UC Merced
UC Merced Electronic Theses and Dissertations

Title
Transport of individual bacteria in microscale structures

Permalink
https://escholarship.org/uc/item/5hd193vj

Author
Chopra, Pooja

Publication Date
2022

Copyright Information
This work is made available under the terms of a Creative Commons Attribution License, availalbe at https://creativecommons.org/licenses/by/4.0/

Peer reviewed|Thesis/dissertation

eScholarship.org
Powered by the California Digital Library
University of California

UNIVERSITY OF CALIFORNIA, MERCED

Transport of individual bacteria in microscale structures

A dissertation submitted in partial satisfaction of the requirements

for the degree of Doctor of Philosophy in Physics

By

Pooja Chopra

Committee in charge:
Professor, Dustin Kleckner, Chair
Professor, Ajay Gopinathan
Professor, Bin Liu

2022

Chapter 3:
© (2022) Physical Review Fluids
All other chapters:
© (2022) Pooja Chopra
All Rights Reserved

The dissertation of Pooja Chopra, titled Transport of individual bacteria in microscale structures, is approved, and it is acceptable in quality and form for publication.

(Professor Bin Liu) Principal Advisor Date

(Professor Ajay Gopinathan) Committee Member Date

(Professor Dustin Kleckner) Committee Chair Date

University of California, Merced
2022

Dedication

To my parents, my daughters Pihul and Ivana, and my husband Dr. Parveen, for their never-ending love, support, encouragement, and sacrifices. Thank you for always believing in me.

TABLE OF CONTENTS

List of Figures vii
List of Tables xv
List of Abbreviations xvi
Acknowledgements xvii
Curriculum Vitae. xix
Abstract 1
Chapter 1: Motivation and Overview 2
1.1: Introduction…………………………………………………………………………...2
1.2: Bacterial motility……………………………………………………………….….2
1.3: Hydrodynamic interactions between bacteria and surfaces ………………………...3
1.4: Active transport through microscale structures………………………………………6
1.5: Unsolved issues on bacterial transport in structured media………………………..6
Chapter 2: Experimental Techniques and Microchannel Fabrication……………….8
2.1: Photolithography …………...…………………………………………………..….8
2.2: Microstructure fabrication……..………………………………………….. 12
2.3: Realtime imaging and tracking of motile bacteria……………………………………20
2.4: Trajectory analyses…………………………………………………………………..21
2.5: An agent-based model………………………………………………………………23
Chapter 3: Geometric effects induce anomalous size-dependent active transport in structured environments…………………………………...…………………..25
3.1: Motivation.…………………………………………………………………………..25
3.2: Tracking individual bacteria in micropillar arrays…………………………………..26
3.3: Pillar-induced trapping…………………………………………………………....27
3.4: Geometric constraints on smooth-swimming bacteria in micropillar arrays………..30
3.5: Size-dependent trapping and escaping……………………………………………....32
3.6: Anomalous size-dependent transport………………………………………………..36
3.7: Discussions…………………………………………………………………………..37
Chapter 4: Run and tumble in structured media……………………………………..39
4.1: Motivation………...…………………………………………………………………39
4.2: Residence of run-and-tumble bacteria on pillar surfaces……………………………39
4.3: Effects of tumbling on transport in micropillars……………………………………42
4.4: A geometric model accounting for self-reorientations………………………………44
4.5: Transport of tumbling cells in micropillars and free spaces…………………………46
4.6: Discussions…………………………………………………………………………..47
Appendix: ………………………………………………………………………………49
A: Safety Measure……………………………………………………………………..49
B1: PDMS Curing protocol……………………...………………………………………..50
B2: Plasma Cleaner……………………….……………………..…………..…..50
C: Preparation of sample used in experiment……………………………………………50

C1: Tryptic Soy Broth Medium (TB solution)……………………………………………..50
C2: Tryptic Soy Agar Plate………………………………………………………………51
C3: Motility buffer (MB)……………………………………………………………....51
C4: Preparation of *E. coli* Strain (HCB 437)……………………………………………..52
C5: Preparation of *E. coli* Strain (GFP)…………………………………………………..52
D.1: Geometric constraints………………………………………………………………53
D.2: Agent-based kinematics subjected to geometric constraints ………………….………55
D.3: Stochastic escaping model………………………………………………………..58

List of References……………………………………………………………………61

List of Figures

Figure		Page
1.1	(A) Schematics of *E. coli* shows the run (left) and tumble (right) activities. (B) Random walks of *E. coli* subjected to a uniform (left) and anisotropic (right) chemical environment. [Reproduced from [12], courtesy of Howard Berg and by permission from Springer, copyright 2010.]	2
1.2	Hydrodynamic images for a pusher force dipole above a flat no-slip surface (red arrows) leading to attraction by the surface (blue arrow). [Reproduced from [28], courtesy of Berke *et al.* and by permission from American Physical Society, copyright 2008.]	3
1.3	Bacteria interactions with surface with no-slip boundary condition. The inset shows observed trajectories of a smooth swimming mutant of *Escherichia coli* (HCB437). [Reproduced from [26], courtesy of Lauga *et al.* and by permission from Elsevier, copyright 2006.]	4
1.4	Hydrodynamic interactions of self-propelled microorganism with surfaces. (A) Schematics of flow fields of a pusher swimmer. (B and C) Trapping of a self-propelled rod by colloidal particles due to hydrodynamic attraction. [Reproduced from [27], courtesy of Spagnolie *et al*. and by permission from Royal Society of Chemistry, copyright 2015.]	5
1.5	Schematic of bacteria close to a surface. The blue and red arrows correspond to the torques arising from hydrodynamic interactions of the cell body with the bottom surface and the drift on the flagella. [Reproduced from [28], courtesy of Sipos *et al.* and by permission from American Physical Society, copyright 2015.]	5
2.1	Schematic diagram of positive (a) and negative (b) photoresist photolithography	9
2.2	Schematic of after development patterns for (a) negative photoresist (b) positive photoresist showing changes in patterns for proper exposure, under exposure and over exposure.	11
2.3	Schematic of photolithography	12

2.4	Flow chart of multi-step process for the microchannel fabrication	13
2.5	a) Spin Coater b) UV Mask Aligner, Quintel Q-2001 TL	14
2.6	SU8 film thickness as a function spin speed (in a 30-second duration).	15
2.7	An overview of the photomask that was used to create the microchannel. (a) The design had multiple diameters pillars (black blocked area) range from 5-50 µm (right to left) with gap 10 µm. (b) zoom in view of image of 20 µm pillars with gap 10 µm. Scale bar shows 100 µm.	16
2.8	Images of microchannels with gap between pillars 10 µm taken at 10X magnification showing 20 μm, 30 μm, and 50 μm (right to left). Scale bar shows 100 µm.	18
2.9	SEM image of pillar array with 30 µm diameter at 40x magnification.	19
2.10	Digital tracking microscope. (a) The microscope stages of a 3D tracking microscopy were programmed by a customized software to follow individual bacterial movement. (b) A snapshot of the software interface, including a real-time microscope view (lower left).	20
2.11	The 3D movement of a wild-type *E. coli* bacterium visualized under the tracking microscope. Colors show its instantaneous speeds.	21
3.1	Simultaneous large-scale and high-resolution study of bacterial transport in a micropillar array through active tracking and image stitching. (a) The trajectory of a single *E. coli* (tracked up to ∼1 mm in distance and ∼10 minutes in time) was reconstructed to characterize its long-term transport. The trajectory is color coded in time. (b) The high resolution that was preserved in each original frame in Figure. 3.1 (a) provided the detailed cell and pillar geometry. The pillars were R = 15 μm in radius, arranged in a square lattice with a lattice constant of a = 40 μm, and a gap of $d = a-2R$ = 10 μm between adjacent pillars. The tracked bacterium (in a dashed contour) was $l \approx 6$ μm in length.	25

3.2 Cell size-dependent trapping and escaping effects. Multiple trajectories for different individuals (color coded by cell length l) are mapped to the same pillar array. The shorter cells tend to circulate around the pillars while the longer cells tend to navigate between the pillars, indicating the distinct trapped and escaping mechanisms, respectively (highlighted in the inset). 27

3.3 Bi-directional circulation of bacteria around pillar surfaces. (a) As shown by the local curvature κ of the trajectory, the same bacterium can circulate a micropillar in both clockwise (blue) and counterclockwise directions (red), as viewed from the top. (b) The probability density function of the normalized curvature κR (sampled every 0.2 μm along the path) shows such a bistability in circulation directions. The slight asymmetry in the distribution is potentially subjected to a nearby bottom surface, which leads more stable clockwise circulations. 28

3.4 (a) Probability distribution ρ of the shorter cells (l < 5 μm), normalized by a uniform density ρ0, shows an effective enhancement at the pillar surface. (b) A similar plot for longer cells (l > 7 μm) shows the opposite effect. 28

3.5 Potential volume exclusion effect (due to finite cell lengths) in the bacterial distribution near the pillar surface. (a) Two example trajectories of the same *E. coli* cell are obtained by tracking the center of the cell body (blue) and its front (red). Both trajectories are mapped into one unit cell of the pillar lattice (a = 40 μm, R = 15 μm). (b) The probability distribution functions (PDF) from these trajectories are shown as a function of the distance to the pillar center (r). Here the length of the cell body is 5.8 ± 0.2 μm. 29

3.6 Heterogeneous cell concentrations near pillar surfaces. (a) The averaged radial distribution of *E. coli* (Fig. 2b and 2c) shows a higher concentration adjacent to pillar surfaces for shorter cells. The shaded area corresponds to the pillar region (with its radius $R = 0.375a$). (b) Distribution ρ is shown as function of the angular position γ about a pillar at different radii (r_1 and r_2) for the same pillar geometry ($R = 0.375a$). The inset shows the locations of these radii in the corresponding 2D distribution of *E. coli* (with their cell body lengths $2\ \mu m < l < 7\ \mu m$). All distributions here are normalized by their values in the uniform case, ρ_0. 30

3.7 Lattice-constrained bacterial residency on the pillar surface. (a) A “pusher” representation of the bacterium (inset, with a cell body length l and a total pusher length l_p) illustrates the geometric constraints for a bacterium circulating around a pillar (at angular position γ). An elongation of l_p to $l_{p,\max}$ (the greatest possible l_p without intersecting neighboring pillars) shows that the adjacent pillar (yellow) can either provide a positive (blue) or a negative (red) contribution to the circulation, demarcated by the orientation (θ_p) of the pusher relative to surface normal of a neighboring pillar $\mathbf{n}_p$. This leads to periodically attractive ($\theta_p < 0$ or without adjacent neighbors; blue or white) and repulsive ($\theta_p > 0$; red) zones on a pillar. (b) A computation of θ_p (solid lines) and maximum $l_{p,\max}$ (dashed lines) give rise to a residency arc angle $\Delta\gamma_0 = 1.1$ rad (for $a = 40$ μm, $R = 15$ μm). (c) The residency arc angles $\Delta\gamma$ (squares), averaged over individual residency events (filled circles), decrease with increasing l and eventually to values below the size of the attractive zone γ_0 (when $l \gtrsim 10$ μm), confirming suppressed circulation for longer cells. 32

3.8 Validating the neighboring-pillar effects on size-dependent bacterial trapping. (a) The box plots of the residency angles $\Delta\gamma$ of *E. coli* (normalized by a full turn 2π) are shown for both short ($l < 4$ μm) and long cells ($l > 7$ μm) under two sets of pillar geometries (with gaps between adjacent pillars $d = 10$ and 40 μm). With this increased gap, the resident angles for long cells are significantly higher while the difference for short cells is insignificant. An asterisk (‘*’) above the link between two data sets indicates a significant difference (here, with its p-value $< 10^{-3}$) from a two-sample t-test (with a Kolmogorov–Smirnov test showing the same result). (b) The corresponding residency angles for the box plots shown in (a) also illustrates a suppressed trapping for long cells ($l > 7$ μm) when subjected to small pillar gaps ($d = 10$ μm). The sample size of each column of data (from left to right) is 66, 85, 13, and 34, respectively. 34

3.9 Size-dependent escaping and global diffusivity. (a) The non-uniform distribution of angles of escaping (γ_f, illustrated in Fig. 3c, inset) shows more probable escaping of bacteria along the diagonals (i.e., $k\pi/4$ with $k = \pm 1, \pm 3$) of the square lattice, consistent with the locations of the repulsive zones. (b) The escaping probabilities P_{esc} are calculated from bacterial trajectories for different cell lengths l (open squares with error bars representing the standard errors). The solid curve corresponds to a fit with a hyperbolic tangent function. (c) The mean squared-displacement (MSD) as a function of the path length (Δs) exhibits a transition from a ballistic regime (MSD $\propto \Delta s^2$) to a diffusive one (MSD $\propto \Delta s$) for both experiments (circles) and numerical simulations with the corresponding P_{esc} (dashed lines). The size of the ballistic regimes, depicted by a ballistic length Δs_c (arrow), increase with l or P_{esc}, consistent with the geometry-induced escaping for longer cells. All lengths in trajectories are normalized by lattice size a. 35

4.1 Effect of active reorientation on bacterial trajectories in micropillar arrays. (a) The trajectory of a smooth-swimming mutant *E. coli* is composed of many circles due to its circulation about individual pillars. (b) A GFP *E. coli* (wild type) bacterium often encounters abrupt changes in swimming directions, leading to a trajectory with non-circular paths. Here the pillar diameter d=30 μm and lattice size a=40 μm. 39

4.2 Residence of bacteria along the pillar circumferences is reduced with self-reorientation capability. (a) The residence angle of the wild-type *E. coli* strain (GFP, in blue) exhibits a much narrower probability distribution function (PDF) as compared to the smooth-swimming mutant (HCB437, in orange) case. (b) The data in (a) are shown in the box plot, with circles (data beyond the box-plot analysis) showing the full range of residence angles for both the GFP and the HCB437 strains. The total numbers of residence angles of these two cases (GFP and HCB437) here are 297 and 390, respectively. 40

4.3 Probability distributions of bacteria within a unit cell of the pillar lattice are compared between the wild-type and smooth-swimming strain. (a) The probability distribution function ρ (normalized by its mean ρ_0) of the wild-type *E. coli* strain are shown in colors within a unit cell. (b) Similar plot for the smooth-swimming mutant. 41

4.4 Effects of self-reorientation on the long-term bacterial transport in a micropillar array. (a) The MSD of a smooth-swimming mutant (HCB437) is shown against its path length, with each curve corresponding to one individual track. (b) MSD plots for the wild type (GFP) cells of the same range body lengths (2 – 5 μm) show a narrower distribution. All length scales here are normalized by the lattice size a=40 μm. The sample sizes of these two cases (HCB437 and GFP) here are 38 and 17, respectively. 42

4.5 MSD curves averaged over all ensembles of the smooth-swimming mutant (HCB347) and the wild-type *E. coli* (GFP) for similar cell body lengths (2-5 μm) show almost negligible effects from bacterial tumbling. While having similar mean transport behaviors, the long-distance ($\Delta s > a$) power law exponent α are much more scattered in the HCB347 case, as shown in box plots (inset). 43

4.6 Simulations of bacterial trajectories in micropillar arrays with an agent-based model under both the smooth-swimming (a) and the tumbling (b) conditions. Micropillars with diameter d = 30 μm and array lattice size a = 40 μm are represented in circles. Solid lines in different colors correspond to the simulated trajectories of individual agents. For each trajectory, a total path length of 400a is shown. 44

4.7 A comparison of the simulated MSD curves under both the smooth-swimming (blue) and tumbling (red) conditions. The error bar shows the standard deviations among 100 sampled trajectories in each case. 45

4.8 A comparison of the MSD curves with and without pillars shows the direct impact of pillar arrays on transport of wild-type *E. coli* that are capable of self-reorientation. Experimental data are shown in open circles. The predictions from the agent-based model are shown in dashed lines. 46

C.1 A streak plate to isolate single colonies of *E. coli* 52

D.1 Geometric constraints in a pillar lattice. (a) Here, the distance between adjacent pillars is given by the lateral size of a square lattice $a = \left|\overrightarrow{OO'}\right|$. A bacterium is simplified as an infinitely thin rod up to a maximum $\left|\overrightarrow{AA'}\right|$ that circulates around a pillar at the origin O along the counterclockwise direction. The cell orientation deviates from the surface tangential by an incident angle θ_i. An adjacent pillar (centered at O') enhances or interrupts the circulation of the microorganisms by providing a force along its surface normal ($\overrightarrow{O'A'}$) and hence a torque. A clockwise or counterclockwise torque is demarcated by the sign of the angle θ_p, the orientation of the cell relative to the O' pillar. (b) The computed mean maximum length $\langle l_{p,\max} \rangle$ (normalized by the lattice size a) is shown as a function of the lattice geometry, characterized by a dimensionless pillar radius R/a 54

D.2.1 The rotational diffusion of free-swimming bacteria. The angular mean-squared displacement (MSD rot) of the swimming directions of E. coli is shown against the elapsed path length Δs for different cell body lengths (open circles). A rotational diffusion coefficient ($D_{rot} = 12MSD_{rot}/\Delta s$) is obtained by a proportional fit (solid line) of MSD(Δs) for all cell body lengths, yielding a random-walk step in cell orientation to be used in the agent-based simulation. The simulated trajectory of free-swimming cells with the above extracted random-walk step reproduces the same rotational diffusivity (dots). 57

D.2.2 Size and speed variations among individual cells. (a) The histogram of cell body lengths of bacteria observed in the study of a typical pillar lattice (R = 30 μm and a = 40 μm). (b) Swimming speed of *E. coli* in pillar arrays show no significant cell length (l) dependencies. Error bars correspond to standard deviations 58

D.3 Stochastic escaping of bacteria from pillar surfaces. (a) Probability density functions of residency arc angles $\Delta\gamma$ for various escaping probabilities within the repulsive zones $P_r = P_{\text{esc}}$, as predicted by a stochastic process (Eq. 15). Here, the escaping probability within the attractive zones is prescribed to be $P_a = 0$ and the distribution curves are averaged for $\gamma_i \in$ 58

$[0,\pi/2)$. (b) The resulting mean residency arc angles $\langle\Delta\gamma\rangle$ are shown as a function of P_{esc} (dashed line). The experimental data (squares, with all error bars indicating standard errors) are shown for comparison.

List of Tables

1. Table A1: lists the safety precautions from the MSDS for the chemicals and biochemicals utilized in our lab (Dr. Liu lab)……………………….……………49
2. Table D.1: Mean maximum pusher sizes $\langle l_{p,\max} \rangle$ computed for different lattice geometries *R/a*…………………………………………………………………55

List of Abbreviations

AFM	Atomic force microscopy
ABP	Active Brownian particles
CCW	Counterclockwise
CDC	Center for disease control and Prevention
CW	Clockwise
BSA	Bovine serum albumin
DI	Deionized water
E. coli	*Escherichia coli*
ECM	Extracellular matrix
PDF	Probability Density Function
PDMS	Polydimethylsiloxane
PEB	Post exposure bake
MSD	Mean-Squared Displacement
SCIF	Stem Cell Instrumentation Foundry
SEM	Scanning Electron Microscopy

Acknowledgments

Thanks to the people I got to meet, my time at University of California, Merced was an absolutely incredible experience for me. I consider it an honor and a joy to have been given the chance to join the University of California, Merced campus and take part in the amazing scientific journey that is graduate school.

First and foremost, I want to express my sincere gratitude to Dr. Bin Liu, my adviser, without whom I would not have been able to complete graduate school. No words can adequately convey the tremendous impact being a part of his group has had on me or how much I value his mentoring. He is a never-ending source of advice on how to improve as a scientist and a person in general. He is constantly available to me and eager to explore new concepts. There is no instructor I could have asked for better.

Then, I'd want to thank Dr. Ajay Gopinathan, who has served as a second advisor. Numerous conversations with him have always aided me in comprehending concepts. I want to acknowledge the members of my thesis committee, Dr. Ajay Gopinathan, Dr. Dustin Kleckner, and Dr. Bin Liu, for spending their time reviewing this work. I want to thank Dr. David Quint for easily guiding me through the process of learning new terminology. I am appreciative to Drs. Linda Hirst and Jing Xu for inspiring me to put forth a lot of effort. For all of their assistance and support provided by CCBM, I must express my appreciation to Sayantani Ghosh, Kara McCloskey, Ajay Gopinathan, and Victor Munoz. Additionally, I want to express my gratitude to Paul Roberts and Carrie Kouadio for their assistance and direction. I also want to thank professors who have had a significant impact on my life for inspiring me when I was discouraged, professors Saw Wai Hla and Frank Pinski from Ohio University and the University of Cincinnati, respectively.

No matter how brilliant a concept may be, putting it into practice may be difficult, therefore I'm grateful to all lab members for their patience and assistance in making it feasible. I acknowledge my close friends as well as my former and present lab colleagues, Jeremias Gonzalez, Yu Zeng, and Joanna Valenzuela. I gained insight into computational codes from Yu Zeng. We appreciate Jeremias Gonzalez's contributions to the scientific conversation and emotional support. A great thank you to Joanna Valenzuela, who trained me in the beginning as the lab manager and later on as a close friend. A special thanks goes out to Linda Jerome, Mariam Yazdaq, Viangkaeo Lee, Cindy Calderon Correa, Radoslav Iliev, Gehad, and Ladiasha, undergrads from our laboratories. I gained a lot of knowledge from them when I was training them.

The other friends who helped me with this project were Dominique Davenport, Fereshteh Memarian, Farnaz Golnaraghi, Niranjan Sarpangala, Jose Zamora Alvarado, Suraj Sahu, Amanda Tan, Megha Suswaram, and Devika Gireesan. For their emotional support, I also want to thank my pals Shikha, Sanvali, Ali, Nishant, Chinky, Shagun, and Raman. I want to express my gratitude to Manu and Raj Agnihotri for their support and adoption as my family. I also want to thank all of my friends who indirectly supported me.

I owe my parents—my mom and dad—a high proportion. My mother's blessing inspires me to work hard, and my father's assistance makes it possible for me to overcome every obstacle. My work has become a reality thanks to the love, support, and understanding of my family, especially my siblings Sidhant Chopra, Neha Chopra, and Dr. Monika Bhalla. I wish to express my gratitude and support to my brother-in-law Sumeet Manglesh and Dr. Karan Veer. My family's children are important to me because of their love and innocence; they inspire me to think more highly. I also want to express my gratitude to my mother- and father-in-law for their patience and love. I want to express my gratitude to my sister-in-laws and their family for their unwavering love and support. I also want to express my gratitude to my family friend Anuj, and his wife Divya, and other relatives for their unwavering support.

I would especially want to thank my husband, Dr. Parveen Kumar, for all of his love, drive, support, and sacrifices in helping me finish my thesis. I want to thank my husband for our enlightening physics conversations. This thesis was made possible by his love and patience, and of course for the time he spent with Pihul and Ivana, our lovely girls. And a particular thanks to my two adorable girls, Pihul and Ivana, whose patience and smile inspire me to set great goals. Pihul gave me the inspiration for this research, and Ivana helped me finish it.

Curriculum Vitae

Pooja Chopra
University of California Merced CA
Email: pchopra@ucmerced.edu,

EDUCATION

- **PhD Candidate** (Physics) UC Merced, California, CA
- **Master of Science** (Biophysics) Ohio University, Athens, OH
- **Master of Science (Physics)** University of Cincinnati, Cincinnati, OH
- **Master of Science (Physics)** Panjab University Chandigarh, India

PUBLICATION

- Pooja Chopra, David Quint, Ajay Gopinathan, and Bin Liu, "Geometry-induced anomalous size-dependence of bacterial diffusion in a micropillar array" Phys. Rev. Fluids **7**, L071101 (2022).

EXPERIENCE AND RESEARCH SKILLS

University of California, Merced-Merced CA | 2016-Present
Graduate student research assistant| Dr. Bin Liu

- Hands-on experience on Purification of Protein in bacteria.
- Hands-on experience on cleanroom fabrication including UV Photolithography, PDMS soft lithography, Mask layout, Profilometer.
- Hands-on experience on cell culture on fibers and analysis using confocal microscopy.
- 1+ years' experience in cancer cell mechanics analysis using flow cytometry, fluorescent imaging.
- Experience in designing and printing photomask using AUTO CAD software package.

FELLOWSHIPS/AWARDS

- Core Facilities Seed Grant Award Fall 2022
- Graduate Student Research Fellowship Fall 2022, 2021,2018
- Outstanding Graduate TA Award Spring 2022
- The Center for Advancing Diversity in Engineering (CADE) Fellowship Fall 2022
- Graduate Student Research Fellowship Summer 2022, 2021,2019,2018
- Graduate Student Research Fellowship Spring 2022, 2021, 2020,2019
- GSOFT travel award, American Physical Society-Soft matter topical group | 2019
- GSA Travel Award Fall 2021
- Physics graduate student Summer Fellowship, Summer 2020
- CCBM Training Award Summer 2019
- Grad Excel peer Mentor AY 2018-2019

- CCBM Mentor for undergraduate Spring 2018
- CCBM Mentor for High School Student 2018
- Physics graduate student Summer Fellowship, Summer 2018, 2017
- Physics Travel Award, AY 2018-2019
- Physics Travel Award, AY 2017-2018
- NSF – Crest Center for Cellular and Bio-Molecular Machines (CCBM) Travel Award, AY 2018-2019.
- NSF – Crest Center for Cellular and Bio-Molecular Machines (CCBM) Travel Award, AY 2017-2018.
- NSF – Crest Center for Cellular and Bio-Molecular Machines (CCBM) Scholar, 2016-current.

TEACHING EXPERIENCE

- **Evidence-Based Teaching Practices**
  University of California Merced; Certificate awarded
  Seven Workshops with discussion participation
- **Teaching Fellow** (SPARK Innovation)
  University of California, Merced, CA
- **Teaching Assistant** (Physics)
  University of California, Merced, CA
- **Teaching Assistant** (Physics)
  Ohio University, Athens, OH
  (Taught more than 6 college/general physics undergraduate lab and recitation sections)
- **Teaching Assistant** (Physics)
  University of Cincinnati, OH
  (Taught more than 15 college/general physics lab and recitation sections)
- **Instructor High School** (Physics and Mathematics)
  K. Key Public School, Hamirpur (H.P) India
- **Instructor Physics**
  Him Academy, Hamirpur (H.P) India
- **Instructor Physics**
  Adhar Academy, Hamirpur (H.P) India

PROJECTS/CONFERENCES/PRESENTATIONS

- Research project at UC Merced, Bacterial sensing and responding to micro-scale objects.
- Research project at Ohio University, Fabrication of multi-parallel microfluidic devices for investigating mechanical properties of cancer cells.
- Anomalous size-dependence of bacterial diffusion in a micropillar array. Pooja Chopra, David Quint, Ajay Gopinathan, Bin Liu, *Advance Material for better tomorrow Virtual Meeting*, June 6, 2021; ***oral presentation***, Presenter: Pooja Chopra

- Anomalous size-dependence of bacterial diffusion in a micropillar array. Pooja Chopra, David Quint, Ajay Gopinathan, Bin Liu, *DSOFT Virtual Meeting*, March 6, 2020; ***oral presentation***, Presenter: Pooja Chopra
- Soft Solids and complex Fluids, June 2019, UMass Amherst, **Transport of individual bacteria in micropillar arrays.**
- National Labs Day (April 2019), University of California Merced. **Transport of individual bacteria in micropillar arrays.**
- Heterogeneous dispersion of individual bacteria in micropillar arrays. Pooja Chopra, David Quint, Ajay Gopinathan, Bin Liu, APS March Meeting, March 4-8, 2019; Boston, MA; ***oral presentation***, Presenter: Pooja Chopra
- Cell size dependence of bacterial motion in micropillar arrays. Pooja Chopra, David Quint, Ajay Gopinathan, Bin Liu, APS DFD Meeting, November 18-20, 2018; Atlanta, GA; ***oral presentation***, Presenter: Pooja Chopra
- Exploring the response of individual bacteria to Micropillar arrays. Pooja Chopra, Yu Zeng, David Quint, Ajay Gopinathan, Bin Liu, APS March Meeting, March 5-9, 2018; Los Angeles, CA; ***oral presentation***, Presenter: Pooja Chopra
- Run and Tumble of *E. coli* in Micropillar Arrays. Pooja Chopra, Bin Liu, APS Far West Meeting, November 3-4, 2017; Merced, CA; ***oral presentation***, Presenter: Pooja Chopra
- 2nd Annual NSF-CREST Center for Cellular and Biomolecular Machines (CCBM) Open House Poster competition (October 2018), University of California Merced, **Transport of individual bacteria in micropillar arrays.**
- 1st Annual NSF-CREST Center for Cellular and Biomolecular Machines (CCBM) Open House Poster competition (September 2017), University of California Merced, **Run and Tumble of *E. coli* in Micropillar Arrays**.
- Center for Cellular and Biomolecular Machines (CCBM) Open House Poster competition (September 2017), University of California Merced, **Run and Tumble of *E. coli* in Micropillar Arrays**.
- CMSS/NQPI Poster competition (November 2015), Ohio University, **Fabrication of multi-parallel microfluidic devices for investigating mechanical properties of cancer cells**.
- Graduate Research Project: **Bound States of e^- in Lithium** using Mathematica and C programing, University of Cincinnati (2014)
- Graduate School Project on "**Study of application of Operational Amplifier,** Panjab University (2009)
- U.G.C sponsored National Conference on "**NANO: The Next Revolution**" 4-5th December 2008 at Mahilpur, Punjab India

PROFESSIONAL DEVELOPMENT AND EXTRA CURRICULUM ACTIVITIES

- Grad student assistant for department events and recruitment
- Peer mentor – Grad Excel peer Mentor Program – UC Merced | 2018-2020
- CCBM Mentor for undergraduate Spring 2017, 2018
- CCBM Mentor for High School Student 2017, 2018

- Workshop of Scientific Writing, August 2019.
- Workshop or short course on Structures and order in soft Matter Physics (APS GSOFT), March 3, 2019
- Summer School on Soft Solids and complex Fluids, - UMass Amherst | June 2-6, 2019.
- Workshop of Evidence Based Teaching Practices – University of California, Merced | Spring 2021
- Workshop of Park AFM certification Program, Summer-Fall 2021
- CCBM Scientific Computing Module- University of California, Merced | July 2018.
- CCBM Nanobiofabrications Module – University of California, MERCED | July17.
- Workshop of Imaging and spectroscopy, July 2017.
- Workshop of Tech-Savvy, May 2016.
- Science project demonstration in 1st annual NSF-CREST Center for Cellular and Biomolecular Machines (CCBM) open house at University of California Merced, 2016 to current.
- Science project demonstration in Physics annual open house at Ohio University, 2014 to 2015.
- Co-author writing student problems and solutions code, LON-CAPA The Learning Online Network with CAPA, August 2014- current
- Secretary, Physics Graduate Student Association (August 2013-June 2014), University of Cincinnati.
- Summer Training on experimental techniques of microbiology and molecular biology at University of Cincinnati, 2012.
- Secured several prizes in general knowledge competition

SELECTED LEADERSHIP/VOLUNTEERING ACTIVITIES

- Judge, Southwest Ohio District Science & Engineering Expo (SEE), University of Cincinnati (2011 to Current)
- Judge, Science and Engineering Fair of Northern Kentucky (SEFNK), 2012-Current
- Judge, State Science Day, The Ohio Academy of Science, 2014- Current
- Member, Women in Science, September 2012-Current
- Member, Graduate Student Senate, Ohio University, August 2014 to 2016.
- Science project demonstration in 1st annual NSF-CREST Center for Cellular and Biomolecular Machines (CCBM) open house at University of California Merced, 2016 to current.
- Science project demonstration in Physics annual open house at Ohio University, 2014 to 2015.
- Member, Physics Department Women Student Association (September 2012- June 2014), University of Cincinnat.

Abstract of the Dissertation

Transport of individual bacteria in microscale structures
By

Pooja Chopra

Doctor of Philosophy in Physics

University of California, Merced, 2022

Diversity among individual microbial responses to environments is essential for understanding their adaptive nature but challenging for experimental studies. These environments include porous media or structured surfaces that are widespread in ecological systems, public health, and industrial applications. However, a traditional laboratory setting that relies on static microscope observations can only provide a given spatial and temporal resolution, which cannot resolve simultaneously the detailed individual features as well as their responses to environments at much different spatial and temporal scales. My research focuses on enriching experimental studies of mechanical effects of environments on bacterial transport by a multiscale platform and understanding the roles played by diversified characteristics of individual cells. By employing a digital 3D tracking microscope to follow individual microorganisms over exceedingly long durations, my studies enable a multiscale platform for such studies and achieve the long-term cellular behaviors at a single-cell resolution. Combining the above experimental platform with artificial microscale structures achieved through microfabrication, we explore the mutual geometric effects of both the environments and individual cells on bacterial transport in a controlled fashion. My finding illustrates that microstructures may induce non-trivial size-dependent transport for swimming bacteria. For instance, an array of micropillars tends to reduce the long-term transport of shorter cells while it promotes that of longer ones for a smooth-swimming *Escherichia coli* strain, which contradicts the common belief that longer individuals are more easily blocked by obstacles. I also found that such anomalous size-dependence in transport can be attributed to the geometric constraints associated with the pillar arrays, which prevent longer cells from being trapped by a single pillar. By introducing a wild type *E. coli* strain that is capable of self-reorientation, I extended this result to understand the transport of bacteria in a more natural scenario.

Chapter 1: Motivation and overview

1.1: Introduction

Bacteria reside in complex living habitats that involve porous media and microscale structures, such as soil particles and mammalian cells. These living microorganisms are responsible for one of top causes of human deaths on a global scale[1,2]. Many of these deadly diseases result from transmission of bacteria through complex living environments to their host cells, including respiratory tract infections, wound deterioration, and many gastric diseases[3,4,5]. In addition to pathogens in clinical studies, how mechanical properties of the environments affect bacterial transport is also of great interest to biologists and engineers due to its importance to ecological and industrial processes[6–8]. Pioneering studies have revealed that geometries of microstructures have already been utilized in nature as antibacterial and antifouling surfaces[9,10]. Many questions remain open on whether microscale structures in these environments can be accessed as tunable parameters for controlling bacterial behaviors.

1.2: Bacterial motility

Motility of *Escherichia coli* (*E. coli*) is enabled by the left-handed helical organelles called flagella. Figure 1.1 depicts the numerous flagella that surround the cell body of the wild-type *E. coli.* Flagella from *E. coli* typically measure 10 μm in length and 20 nm in thickness[11,12]. Most *E. coli* cells have multiple flagella randomly distributed on the cell's surface, with each attached to a flagellar motor[12,13]. The basal body of the flagellar motor acts as a rotor that turns the flagellar filaments, enabling the run-and-tumble movements of *E. coli*[11,12]. When all motors run in the counterclockwise (CCW) direction (as viewed from their basal ends), these filaments form a bundle to push the cell forward[12] and the bacterium

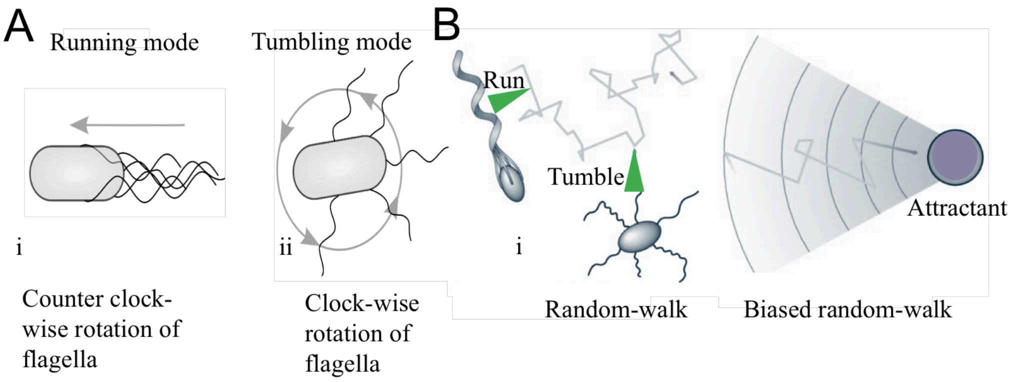

***Figure 1.1**:* (A) Schematics of *E. coli* shows the run (left) and tumble (right) activities. (B) Random walks of *E. coli* subjected to a uniform (left) and anisotropic (right) chemical environment. [Reproduced from [12], courtesy of Howard Berg and by permission from Springer, copyright 2010.]

runs. Intermittent switches of motors to the clockwise direction cause disassembly of the bundle, and the bacterium tumbles (Figure 1.1 (A)). At low loads, a flagella motor can rotate up to several hundred hertz[14].

The dynamic nature of living microorganisms comprises their capabilities to sense and respond to a plethora of environmental conditions, termed taxis. In the presence of chemotactic stimuli (a stimulated condition), the frequency of tumbles is conditionally suppressed, and the bacterial cells employ a biased random walk toward the chemoattractant[15,16] or away from the chemorepellent. This mechanism enables bacteria to approach their favorable chemical environments as shown in Figure 1.1 (B)[12,17,18]. For bacteria swimming by rotating flagellar filaments, a feedback loop is achieved through regulatory proteins that control flagellar motors[11–14]. The underlying mechanisms of the resulting bacterial behavior are studied via the use of advanced experimental techniques, such as optical traps[18], microfluidic devices[19–28], and the use of 3D tracking microscopes [29,30].

1.3: Hydrodynamic interactions between bacteria and surfaces

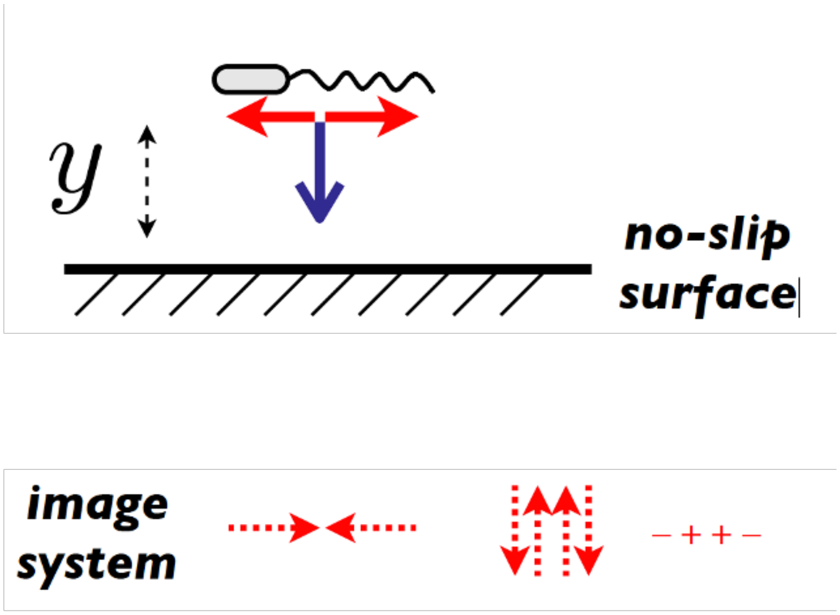

Figure 1.2: Hydrodynamic images for a pusher force dipole above a flat no-slip surface (red arrows) leading to attraction by the surface (blue arrow). [Reproduced from [28], courtesy of Berke *et al.* and by permission from American Physical Society, copyright 2008.]

In their natural habitats, bacteria encounter a variety of solid structures[3,4,12,31]. Porous media[4,24,32], polymer suspensions, and a crowd of cells[7,18,20,22,33] are examples of these structured environments.

A swimming bacterium is conveniently treated as "pusher"-like force dipole for consideration of cell-structure interactions[27,34]. For instance, a cell-wall attraction can be attributed to the interactions between a pusher and its image system associated with a no-slip surface, including a force-dipole, force-quadrupole, and quadrupole source term[34]. Overall, these interactions lead to a torque that reorients the cell to swim toward the surface (Figure. 1.2). The hydrodynamic interaction thus keeps cells close to the surface[20,26,27].

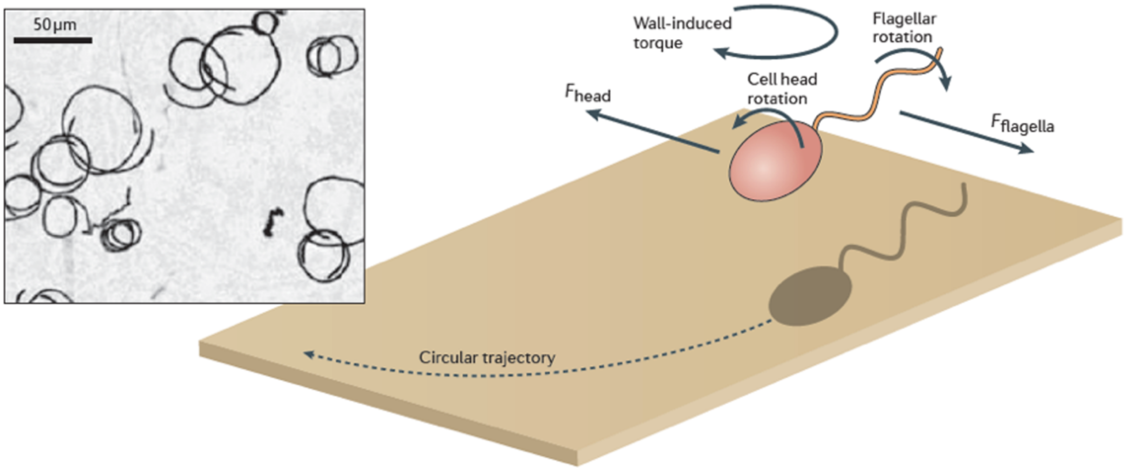

Figure 1.3**:** Bacteria interactions with surface with no-slip boundary condition. The inset shows observed trajectories of a smooth swimming mutant of *Escherichia coli* (HCB437). [Reproduced from [26], courtesy of Lauga *et al.* and by permission from Elsevier, copyright 2006.]

When bacteria swim parallel to a surface (Figure 1.3), the left-handed flagellum rotates counterclockwise (viewed from the flagella-side); the motion of the flagella relative to the nearby surfaces induces additional resistances and leads to a net force (F_{flagella}); the cell body counter-rotates and experiences a force in the opposite direction (F_{head}). The pair of forces thus introduce a net torque perpendicular to the plane of bacterial swimming, resulting in circular trajectories[26,27,34].

The interaction of bacteria with complex geometries has led to intriguing results. For a curved surface, the hydrodynamic interaction between a pusher and a solid wall is sensitive to detailed orientation. For instance, the hydrodynamic interaction is attractive if the bacteria is oriented parallel to the wall but becomes repulsive if it is oriented π/4 away from the surface tangential [26,27,35] (Figure 1.4 (B)).

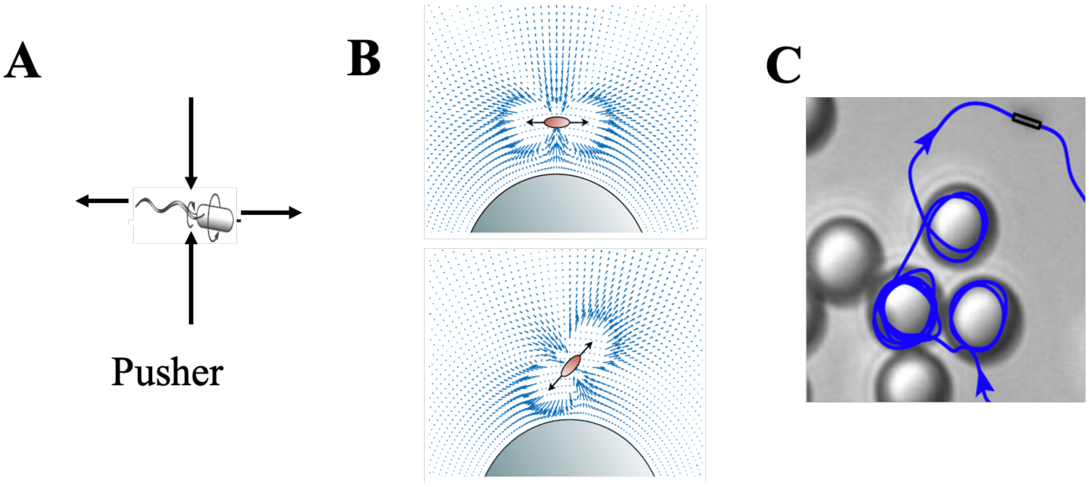

Figure 1.4: Hydrodynamic interactions of self-propelled microorganism with surfaces. (A) Schematics of flow fields of a pusher swimmer. (B and C) Trapping of a self-propelled rod by colloidal particles due to hydrodynamic attraction. [Reproduced from [27], courtesy of Spagnolie *et al*. and by permission from Royal Society of Chemistry, copyright 2015.]

Besides the above cell-wall attraction, a bacterium requires an external torque to follow a curved surface. As shown in Fig. 1.5, such a torque can potentially be achieved by a friction force between the cell body and surface. In order to complete a full circulation, this friction-induced torque needs to exceed the minimal hydrodynamic torque for rotating and dragging the flagella filaments along with the circulation such that a positive angle of the propulsion relative to surface tangential is maintained[28,36,37].

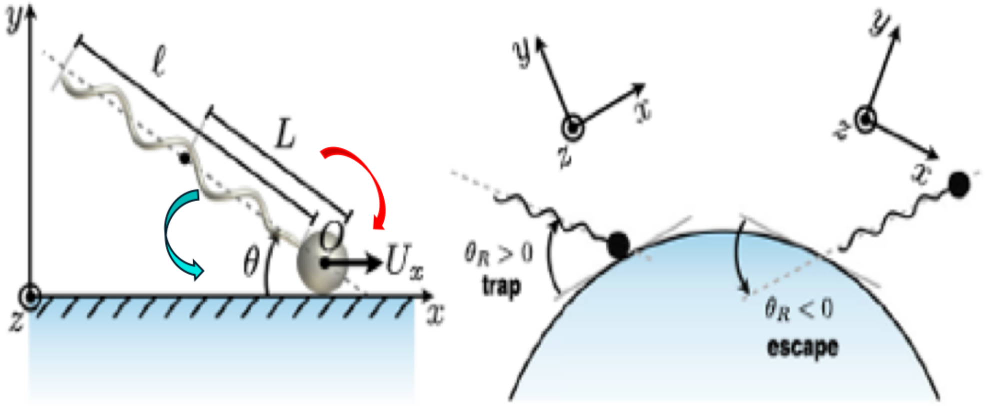

Figure 1.5: Schematic of bacteria close to a surface. The blue and red arrows correspond to the torques arising from hydrodynamic interactions of the cell body with the bottom surface and the drift on the flagella. [Reproduced from [28], courtesy of Sipos *et al.* and by permission from American Physical Society, copyright 2015.]

1.4: Active transport through microscale structures

Besides the understanding of the bacterium-wall interactions, many interests remain on how these solid walls can be structured to influence the transport of bacterial suspension and the surrounding fluid.

Pioneer studies have already revealed complex interplays between bacterial motilities and geometries of environmental structures. Studies in randomly distributed colloidal particles revealed that a relatively low density of obstacles enhanced bacterial transport through more effective forward scattering[38]. Similar structure-induced enhancements in transport were also found in simulations of self-propelled particles in various types of heterogeneous media. As illustrated in a lattice model, randomly distributed mobile obstacles determined an optimal tumbling probability for transport of run-and-tumble particles[19]. By modeling obstacles as attractive potential wells, a noise-sensitive trapping was revealed for self-propelled particles, which was suggested for sorting particles with various reorientation capabilities[22]. A periodic alignment of obstacles was attributed to an enhanced directionality in the transport of active Brownian particles (ABP) at a long-time scale, which was further promoted by increasing the size of obstacles[20]. Despite these structure-induced enhancements in transport, high spatial confinements in porous-media-like structures were observed to restrict both the directional running lengths and the effectiveness of self-reorientation of bacteria, and thus impact their long-term diffusivities by altering the run-and-tumble statistics[25].

In the presence of a gradient of chemoattractant, maze-like microscale structures have been already employed to impact bacterial chemotaxis. Despite such sophisticated topologies in structures, bacteria collectively explore the shortcut by composing a chemotactic wave, leading to effective chemotaxis[21]. Besides maze-escaping, microbial responses to the environmental attractant or repellant were also found tunable through the orientation of periodically aligned microstructures, which are desirable for sorting microbes[23].

In the presence of a background flow, bacterium-structure interactions were found to contribute to a finite residence of motile bacteria on structure surfaces and their upstream movements, leading to distinct dispersion properties from immotile particles[24]. Additionally, hydrodynamic gradients due to periodic microstructures were demonstrated to hinder the transverse dispersion of bacteria and promote both those upstream and downstream ones, accompanied by nonlinear responses of bacteria streaming to flow directions[39].

1.5: Unsolved issues on bacterial transport in structured media

Previous studies have revealed rich bacterial behaviors in structured media, which have been attributed to complex cell-structure interactions. However, a fundamental principle that characterizes such cell-structure interactions is still underexplored, limiting the applications of microstructures for sophisticated biological controls. Additionally, cell morphologies, which inevitably play roles in the effects of microstructures, are challenging to explore experimentally and implement numerically in most of these studies. These challenges are mostly due to limitations in available experimental and computational techniques. Bacteria within the same strain were conveniently treated in a uniform system, without considering detailed *variations in sizes and shapes*. Such diversities, however, are essential to understand the adaptive nature of living bacterial systems.

In my research projects, I aim to close this gap of knowledge by investigating the interplay between individual sizes and microstructure geometries in bacterial transport at a single-cell resolution. In order to address variations in bacterial responses associated with individuals, microscale structures in bacterial environments need to be prepared with a high spatial resolution to resolve all geometric features that potentially contribute to the cell-wall interactions. The detailed method in achieving a well-controlled microstructure is discussed in the next chapter.

Further, to explore the interplay between cellular morphologies and microstructures in diverse bacterial behaviors, we need to resolve both the individual geometries and the associated large-scale transport, which have two length scales different by orders of magnitude. To achieve such a multiscale study, we employ a tracking microscope to follow each individual cell over extended temporal and spatial scales while keeping a high magnification and high-speed recording. These microscope images recorded at high spatial and temporal resolutions were combined for detailed analyses of their transport characteristics and the mechanical effects of the microscale structures. These methods in imaging and data analysis are also discussed in the next chapter.

Chapter 2: Experimental Techniques and Microchannel Fabrication

2.1: Photolithography

Over the past few decades, the area of microfluidics, also known as lab-on-chip, has become a powerful tool in biological research laboratories[40,41]. Different types of fabrication methods have been adopted, including etching, machining, photolithography, soft lithography, and laser ablation[41]. In this research, we have utilized UV photolithography and soft lithography to fabricate the microfluidic devices. In this chapter, we will discuss the fundamentals and protocols of photolithography and soft lithography utilized to create microfluidic devices for our research.

Microfluidic devices are fabricated using UV photolithographic technique [40,42]. A standard photolithography technique utilizes a photosensitive polymer known as photoresist that is selectively exposed to light through a mask, leaving a latent image in the photoresist. In the next step, the exposed photoresist is selectively dissolved in a solvent known as developer to create patterned access to an underlying substrate. The developed patterns are subsequently transferred to a final medium [42]. The medium that is most frequently utilized in the creation of microfluidics devices is polydimethylsiloxane (PDMS) [40].

A photoresist is a polymeric material that is sensitive to light and used in photolithography to pattern the designs. Polymer chains that make up photoresists can be altered by light exposure. Photoresists come in two categories: positive photoresist and negative photoresist. For positive photoresist, the areas exposed to light becomes more soluble in the developer. On the other hand, for negative photoresist, the areas exposed to light becomes less soluble in developer.

A comparison of positive and negative photoresist photolithography is shown in Figure 2.1. Light exposure in a positive photoresist causes the longer polymer chains to break into shorter ones, making the exposed region soluble in the developer. The areas that were not exposed are still resistant to photoresist developer. Contrarily, using negative photoresists, the light exposure forms crosslinks between the lengthy polymer chains, making the exposed area largely developer insoluble. The developer solvent is soluble in the areas that were not exposed. In general, light-sensitive additive molecules and polymer molecules are combined to create negative photoresists [42,43].

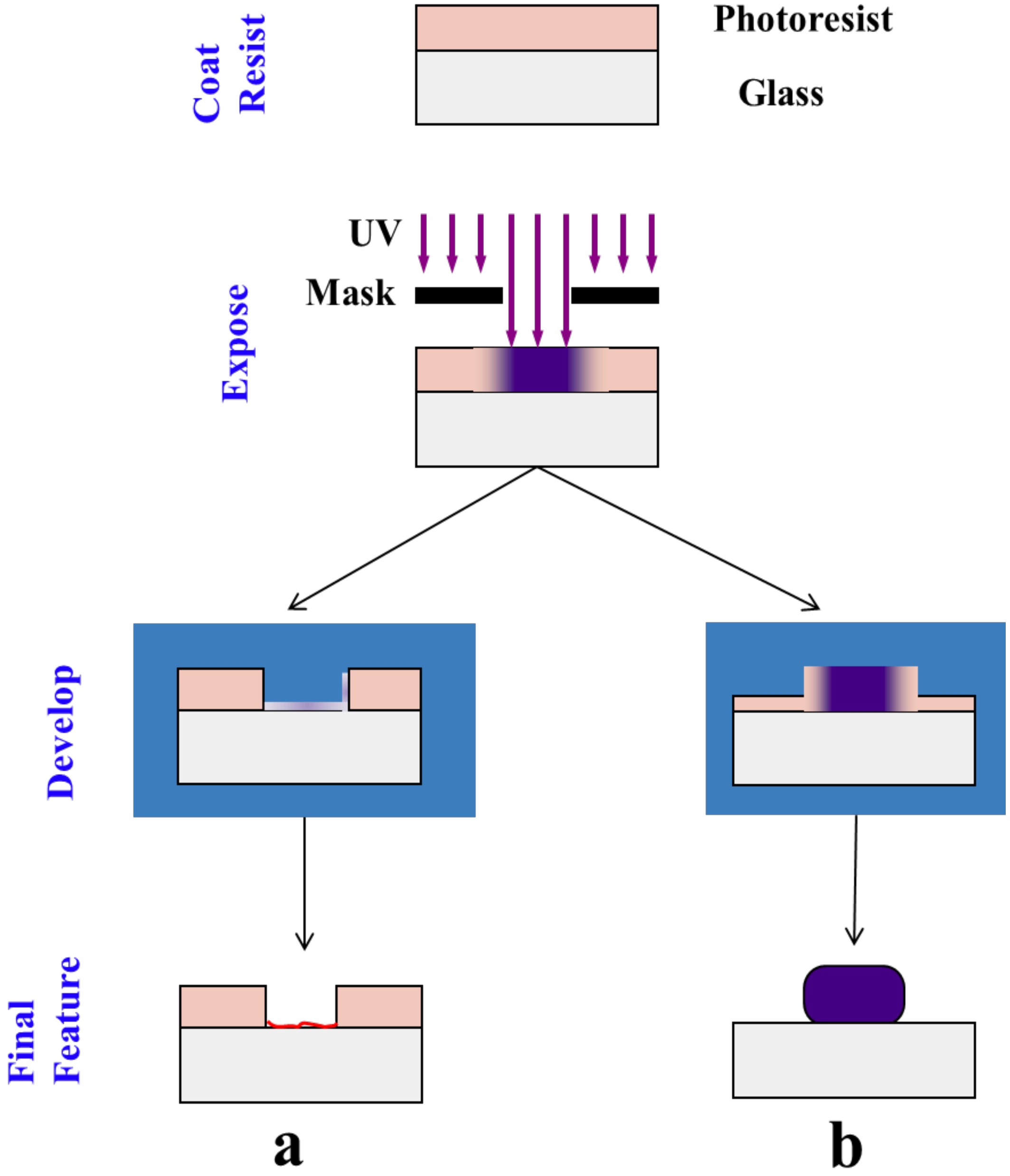
Coat Resist
Photoresist
Glass
UV
Mask
Expose
Develop
Final Feature
a
b

Figure 2.1: Schematic diagram of positive (a) and negative photoresist (b) photolithography.

Each category of photoresist has advantages and disadvantages. Because of the great pattern resolution that results from the comparatively low photosensitivity, positive photoresists are renowned for being able to create incredibly small structures. Positive photoresists' low photosensitivity can be used to manipulate the edge profile of patterned objects. Long chains in positive photoresist must be broken by extended light exposure times due to poor photosensitivity.

When compared to positive photoresists, negative photoresists are far more photosensitive but have lower resolution[42,43]. Negative photoresist has an extremely sensitive nature that requires shorter exposure times, and it only needs one crosslink per molecule to become insoluble in developer. However, developer chemicals are absorbed by the negative photoresist, resulting in a swelling of the photoresist and hence lead to poor resolution in the design.

In photolithography, spin coating is a common method for achieving a precise photoresist thickness. In this procedure, a liquid photoresist is applied to the center of the substrate that will be coated before the substrate is quickly spun up to a predetermined speed (between 2 and 8 krpm). A uniform thin coating of photoresist is produced on the substrate or glass thanks to centrifugal force. The type of photoresist used, and the spinning speed and time determine the final film thickness. The findings of our procedure that we used to calibrate spin speed for a constant spin time are presented in the following.

To optically transfer designs onto resist, a photolithography mask serves as a template. The photomask is a transparent and opaque sheet that allows light to pass through in certain patterns. The best photomasks for extremely high-resolution work are composed of quartz or glass plates and have an opaque chromium layer pattern on them. The photomasks are fabricated using e-beam lithography and can be designed as per experiment requirements.

A small layer of photoresist is exposed to strong light in the 350–400 nm region through a photomask in order to produce the required patterns. Different exposure modes, including as contact, projection, and proximity modes, are available for exposure. Since there is a gap between the mask and the photoresist film in proximity mode, the resolution is low due to light diffraction at the margins of the features [44]. In the contact mode, the mask and photoresist film make contact during the exposure and provides high resolution. We have employed the contact mode during photoresist exposure.

The parameters of exposure duration and exposure energies must be tuned to achieve required resolution. The intended pattern may be seriously hampered that are both overexposed and underexposed. Improper exposure produces overcut and undercut patterns [41,43,45,46]. Figure 2.2 (a) and (b) illustrates a schematic of the appropriately exposed, overexposed, and underexposed exposure of positive and negative photoresist.

Following exposure, a development solution is applied to the sample, which dissolves the photoresist's soluble component and reveals the patterned surface. The energy needed for the full disintegration of photoresist is known as the exposure energy E_T calibrated for exposure step. A post baking step could be followed development to harden the remaining photoresist and improve the adhesion for post development processing.

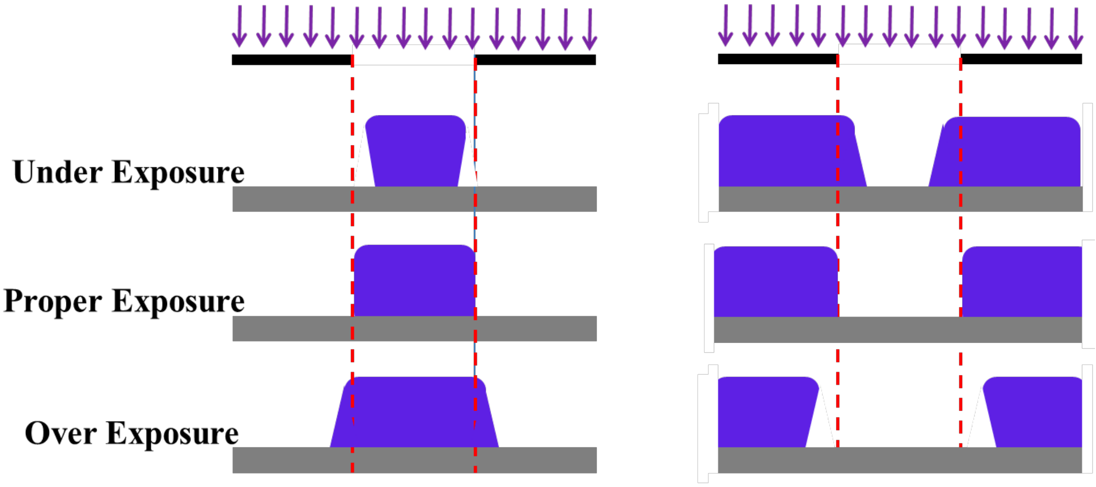

(a) Negative Photoresist **(b) Positive Photoresist**

Figure 2.2: Schematic of after development patterns for (a) negative photoresist (b) positive photoresist showing changes in patterns for proper exposure, under exposure and over exposure.

The photolithography is utilized for creating microchannel molds on a substrate-also referred to as the master mold. During next step, the master mold is used to cast the microchannel using soft lithography, low-cost rapid prototyping technique for transferring micro/nano features on a flexible and soft substrate. Soft lithography can process a wide range of mechanically soft materials, known as elastomeric material. For microfluidic applications, PDMS is a widely utilized, low cost, biocompatible polymer. The low toxicity, chemical inertness, and variable surface chemistry of PDMS, together with its mechanical flexibility and durability, make it a suitable material for casting microfluidic devices. In this step, PDMS is poured into the mold and heated to a high temperature along with a curing agent (which crosslinks the polymer). The hardened PDMS is then removed from the master mold. Figure 2.3 represents the steps used in photolithography to create a master mold and subsequently cast PDMS microfluidic channels from the mold. The next section is devoted to protocols adapted to fabricate a microchannel using UV photolithography and soft lithography.

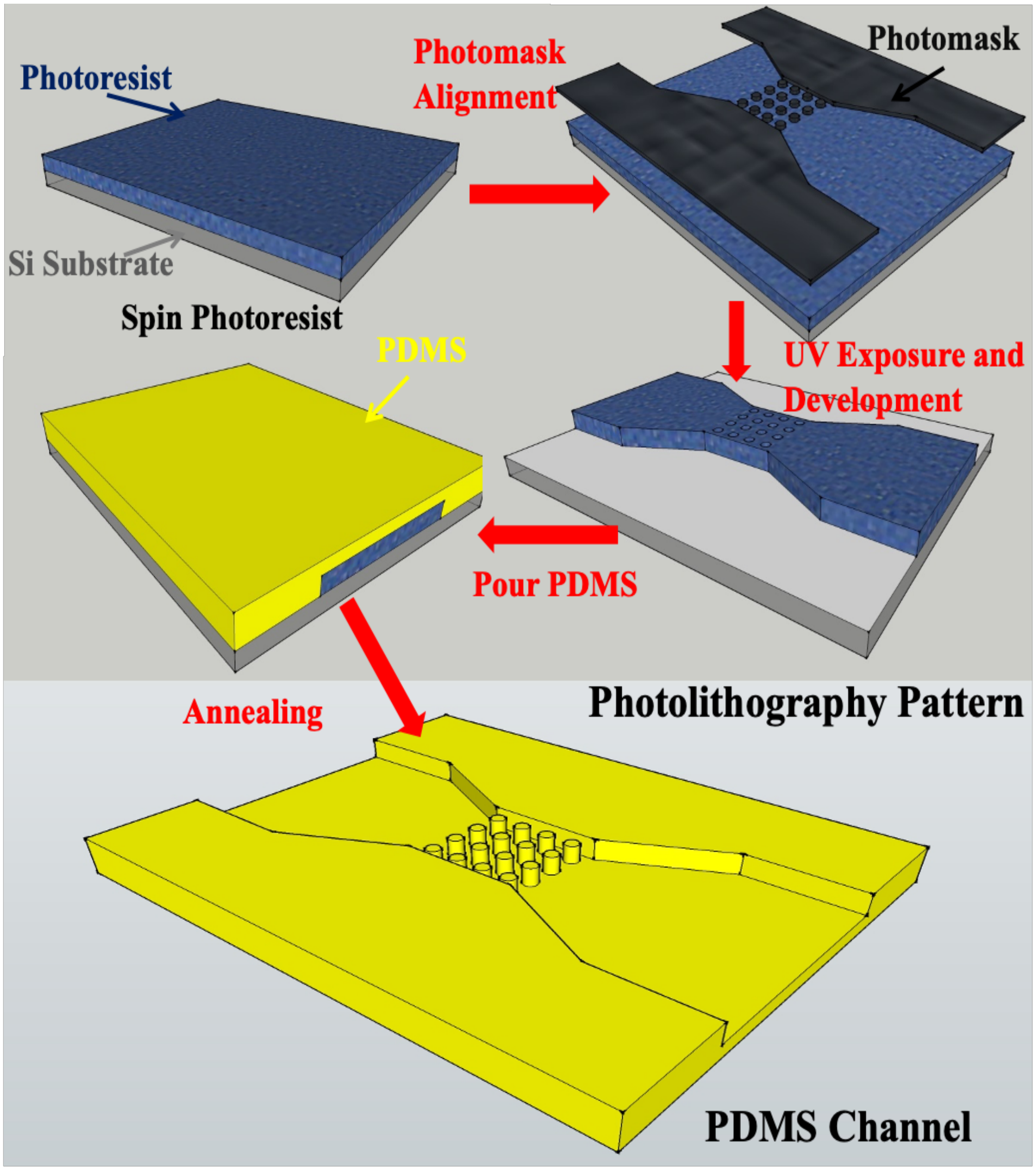
Photoresist
Si Substrate
Spin Photoresist
Photomask Alignment
Photomask
UV Exposure and Development
PDMS
Pour PDMS
Annealing
Photolithography Pattern
PDMS Channel

Figure 2.3: Schematic of photolithography.

2.2: Microstructure fabrication

The principles of microchannel manufacturing employing photolithography to fabricate a master mold and soft lithography to cast a master mold on the PDMS have been covered in previous sections. A clean and functional microchannel device requires the optimization of several processes. Fabricating microchannels is a crucial and extremely challenging stage to examine the interaction of bacteria with microchannels. A lot of efforts have been made to optimize the fabrication parameters to fabricate microchannel of required features with precise resolutions. The protocols presented by photoresist manufacture Microchem have been optimized in order to build single and multiple pillars with a different diameter ranging from 5 microns to 50 microns on a single device. Several pillars on a single device have been fabricated using the modified protocols using SCIF cleanroom. Figure 2.4 represents the microfabrication steps, and the following sections provide a detailed explanation of each step.

Substrate Cleaning

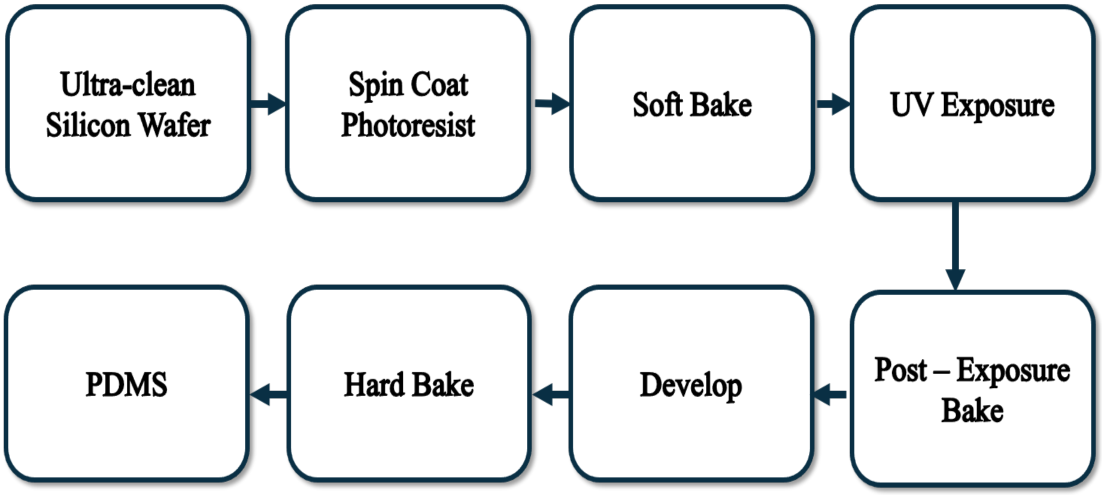

Figure 2.4: Flow chart of multi-step process for the microchannel fabrication

A prepared stock cleaning solution of 1:1 HCl (hydrochloric acid) and deionized (DI) water was used to clean the glass substrate Glass slides were soaked in the prepared stock for 15 minutes, and then the substrate was washed in sequence using acetone (2 minute), methanol (2 minute), DI water and dried using dry N2. Because a dirty substrate can result in flaws in the final design, the glass surfaces were investigated under a microscope to make sure they were clean. The glass slides were pre-baked at 150°C for 5 minutes to evaporate any organic contamination.

Spin Coating

The spin speed and spin time of spin coater were calibrated during the photolithography process in order to get the necessary height of microchannel required for our experiment. The goal of calibrating the spinning speed is to achieve an ideal thickness of photoresist, here, 30 μm.

A variety of negative photoresists including SU8-2015, SU8-2020, SU8-2050 etc. have been investigated. Here, I am reporting the results of only SU8-2015 photoresist. A drop of bubble-free SU8-2015 negative photoresist was carefully applied to the glass slide. The photoresist was spread out using an initial spreading speed of 500 rpm with an initial acceleration of 100 rpm/sec, and then a variable higher spin speed was utilized to regulate the film thickness, which was obtained by an acceleration of 300 rpm/sec. The substrate was continuously spun at a high angular velocity for 30 seconds by the spin coater.

"Film thickness is essentially a compromise between the centrifugal force that pushes the fluid resin towards the edge of the substrate and the drying pace which influences the viscosity of the resin," according to Tyona (2013)[47]. The viscosity of the resin rises as it dries to the point where the radial force of the spin process is unable to transport the resin over the surface [42,43]. At this point, neither the spin time for a fixed spin speed nor the spin speed for a given spin time will cause the film thickness to decrease.

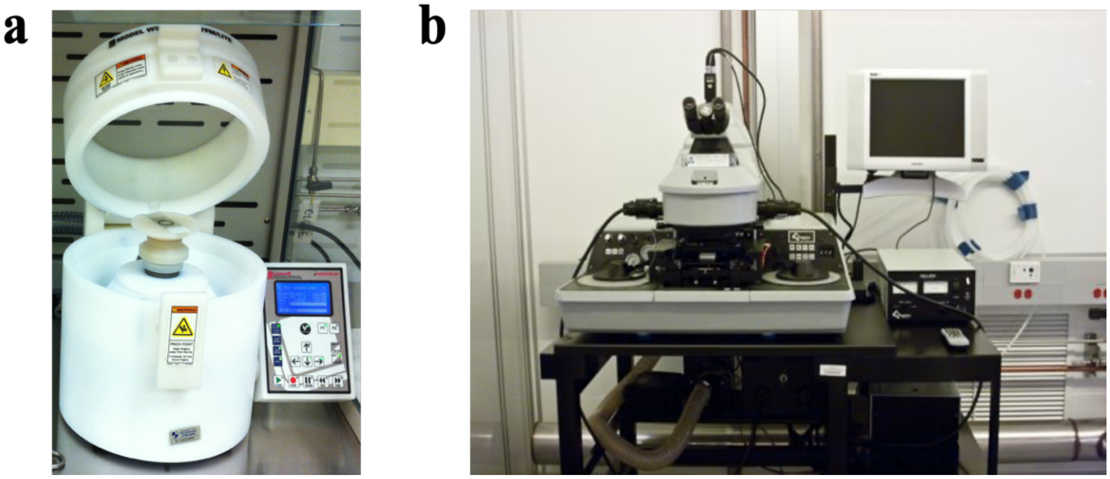

Figure 2.5: (a) Spin Coater (b) UV Mask Aligner, Quintel Q-2001 TL

In order to deposit photoresist on a glass substrate, we employed the Laurell Technologies: Multiuser Process Software Controller WS-650 Modular Spin Processor shown in figure 2.5a. Rapid acceleration was automated during each step. This instrument offer spin capability up to 12,000 rpm with 1 rpm spin precision.

Figure 2.6 represents the thickness data as a function of spin speed at constant spin time demonstrating a significant change at lower spin speeds and settles to a rather consistent value at spin speeds of 3000 rpm and above. All five photoresists in the SU-8 2000 series-SU-8 2005, SU-8 2007, SU-8 2010, and SU-8 2015 exhibit comparable patterns, as illustrated in Figure 2.6.

The primary distinction between these photoresists is their viscosity. Here we use a negative photoresist SU-8 2015. Microchannels were created utilizing the spin speeds of 1000, 1300,1500, 2000, 2500, 3000, and 3500 rpm to verify the manufacturer's specifications.

Specifically, a spread spin at 500 rpm for 15 seconds, followed by a spin at 1300 rpm for 30 seconds, should result in the thickness of 30 μm. Bruker's Dektak XT stylus profilometer was used to measure the height of the microchannel with high precision in nanometer range.

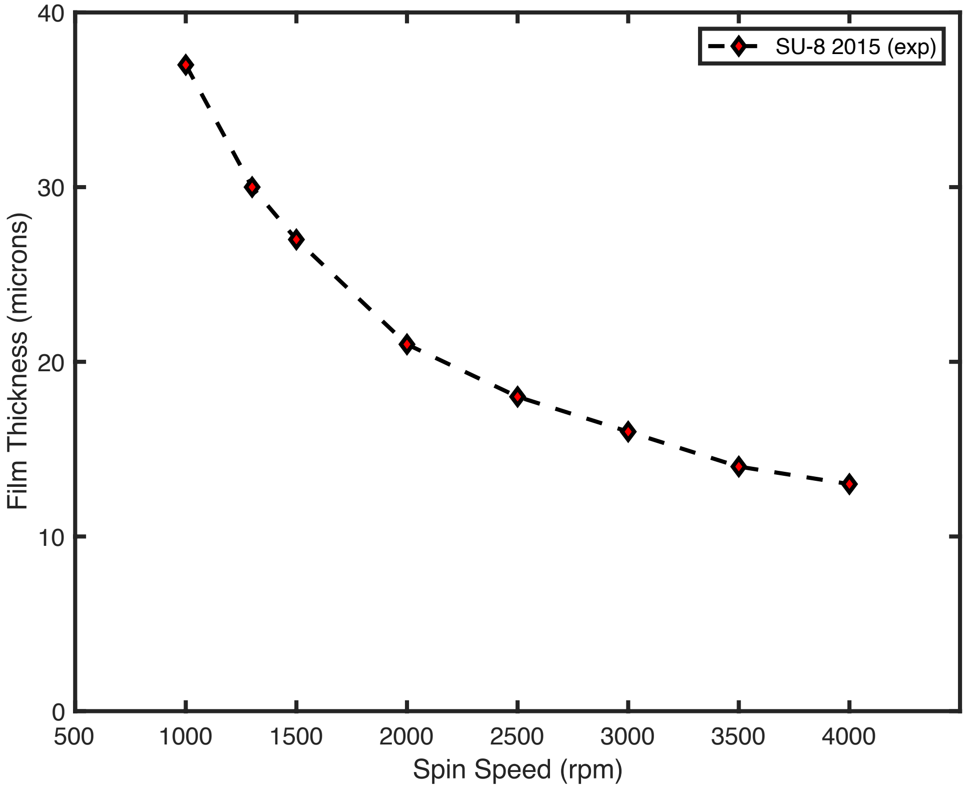

Figure 2.6: SU8 film thickness as a function spin speed (in a 30-second duration).

The Figure 2.6 shows the measured thickness of our microfluidic channels, in agreement with nominal thickness from the manufacturer. Thus, we established that we may utilize the manufacturer's data to change spin speed to get the desired thickness. The microchannels in this study were deposited at a spin speed of 1300 rpm for a continuous spin period of 30 seconds and reports the microchannel thickness of 30 µm.

Soft Bake

The photoresist was baked for 4 minutes at 100°C using a hot plate. A soft bake step is required to initiate the photosensitivity of photoresist. The baking time was determined based on the measured thickness. The soft bake also hardens the photoresist and protect the surface when a contact is made with mask in exposure step. The samples were cooled at room temperature for next step.

Photomask Design and Fabrication

The photomasks used to design the microchannels were made using AutoCAD and Matlab and then printed on a 5” X 5” quartz using chrome as blocking layer at 40,000 dpi by an industrial mask printing facility (Photoronics Inc., Brookfield, CT). An image of designed photomask pillars vary from 5 to 50 μm with gap size of 10 μm is shown in Figure 2.7. The design had a single entry and exit. We created numerous channels with the same spacing size of 10 µm and varied diameters of 20, 30, and 50µm. The purpose of our experiment is to investigate the interaction of a single bacterium with different size pillars, despite the fact that all size pillars were built for different chips. We therefore created a channel to increase experimental throughput. We also designed three separate sets of multi-pillar channels, with pillars that vary from 5 to 50 μm with varied spacing sizes of 10, 20 and 40 μm. In this kind of setup, we can follow and record a single bacterium on the same device due to a multi-pillar design. The use of the same channel for all recordings reduces mechanical noise, making a multi-size pillars system more durable than a single size pillars design.

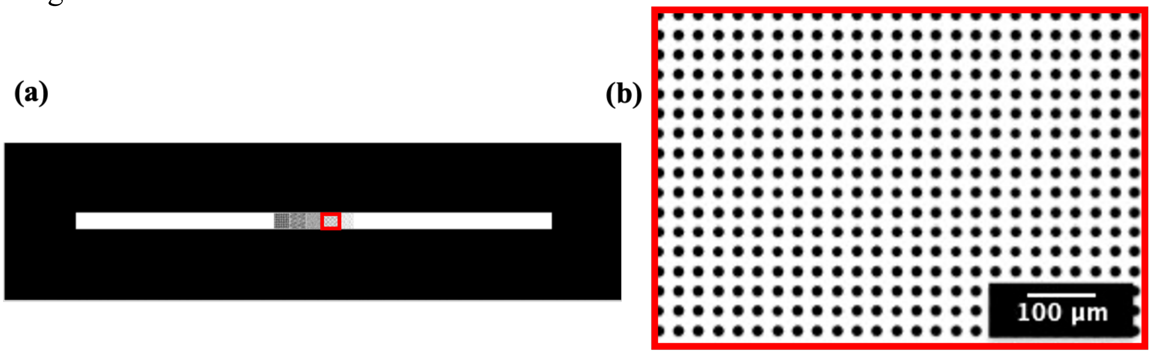

Figure 2.7: An overview of the photomask that was used to create the microchannel. (a) The design had multiple diameters pillars (black blocked area) range from 5-50 µm (right to left) with gap 10 µm. (b) zoom in view of image of 20 µm pillars with gap 10 µm. Scale bar shows 100 µm.

UV Exposure

The Quintel Q-2001 TL UV Mask Aligner shown in Figure 2.5 b is used for UV exposure. The samples were exposed to UV light through the photomasks for 2 to 10 seconds in the steps of 1 second for a constant exposure energy. The samples were investigated after development. A low contrast between the exposed and unexposed region was seen for exposure times less than 4 seconds. Due to the poor contrast, some channels were removed (dissolved) during the development step and resulting in channels that were either unfinished or had irregular heights, and their walls were not straight. On the other hand, wide microchannels were seen for exposure periods greater than 4 seconds. The wider channels were considered as a sign of overexposure because photoreactive polymer had extended chains from the exposed region into unexposed regions. An exposure time of 4 second was optimized to fabricate microchannel for our study.

Post Exposure Bake (PEB)

The crosslinking mechanism started during the exposure stage must be completed by the PEB step. The PEB also lessens mechanical stress created during the soft baking process and improve the resolution. The PEB was applied to the exposed sample for 20 minutes at 100°C.Within 1-3 seconds of placing the sample on the hot plate, I noticed a visible latent picture in the photoresist. According to the manufacturer's specs, the estimated creation time of these visible latent pictures is between 10 and 15 seconds. The PEB time was increased from 1-2 minutes (from manufacturer recommendation) to 20 minutes to protect photoresist from complete wash during development step. The soft bake that happens before an exposure process is not the same as PEB. A series of samples were investigated to optimize the PEB time. More than 10 samples were exposed for 4 seconds and developed for 30 seconds. These samples were investigated for varied exposure time ranging from 1-25 minutes at a constant temperature of 100°C. All samples were investigated under the microscope. Some features were washed away during the development stage at PEB times shorter than 20 minutes

Some of the unexposed photoresist that we wished to remove adhered to the glass substrate for PEB times longer than 20 minutes. To remove unwanted photoresist, we tried extending the development time from 30 seconds to 2 minutes, but it didn't work very well since either the channels were washed away with longer development times, or the unexposed photoresist didn't come out. We have optimized the PEB time for 20 minutes for our microchannel fabrication. All features with varied pillar sizes and spacing of 10 µm were fabricated using exposure time of 4 seconds, PEB for 20 minutes at 100 °C and developing for 30 sec. The image of varied pillar sizes with uniform spacing of 10 µm are shown in Figure 2.8.

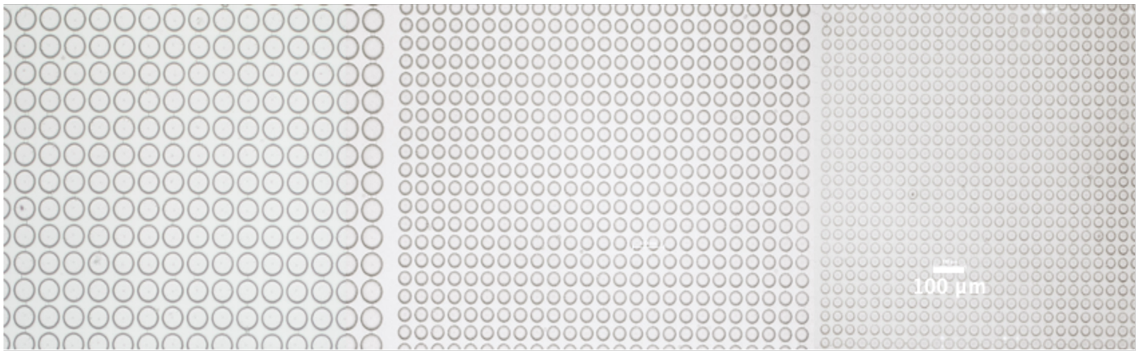

Figure 2.8: Images of microchannels with gap between pillars 10 µm taken at 10X magnification showing 20 μm, 30 μm, and 50 μm (right to left). Scale bar shows 100 µm.

Development

Following the PEB procedure, spin-coated glass slides were dissolved for 30 seconds in SU-8 developer and then quenched using 70% isopropanol. After development, the formed patterns on the glass slides were examined under a microscope. I noticed distinct microchannel patterns after a 30-second development period. I also experimented with development times of 10 to 60 sec with a step of 5 sec. The unexposed photoresist that we wished to remove did not clear for development durations under 30 seconds, and for development times beyond 45 seconds, the microchannels were washed away together with the unwanted photoresist. Although the 35–40 second development durations did not fully wash the channel, the diameters of the microchannels were reduced. The unexposed photoresist was entirely wiped out during the 30-second development time optimization, and the channel widths were as anticipated given our photomask designs. I didn't notice changes in the channel heights with development time, despite the manufacturer's literature on SU-8 states that overdeveloping a sample might cause a drop in microchannel heights. This is justified because our optimized exposure time and PEB times are much lower than anticipated by the manufacturer Microchem.

Hard Bake

The microchannels were hard baked at 200°C for two hours after development step. To solidify and stiffen the produced photoresist patterns for following procedures, rigorous baking is necessary. This procedure improves the photoresist's chemical, physical, and thermal stability. I frequently noticed that after development, the narrowest, most fragile parts of the created designs were somewhat separated from the glass substrate. The microchannel pattern writhes or twists as a result of this. In order to eliminate bending of the microchannel patterns, a fast thermal annealing phase at 100°C and 200°C for 10–20 sec was introduced before the full hard bake. The temperature of the substrate is swiftly raised during fast thermal annealing. According to Cheng et al. (2004), rapid heat annealing is utilized to enhance the surface properties and the binding between produced photoresist and glass substrate [48].

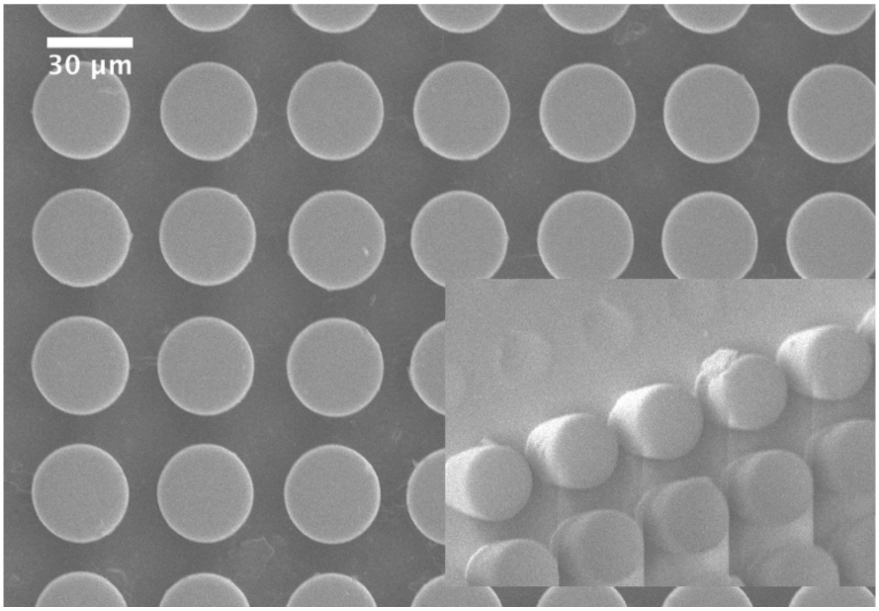

Figure 2.9: SEM image of pillar array with 30 µm diameter at 40x magnification.

We used a profilometer (Bruker Dektak XT) and SEM (Zeiss Gemini SEM 500) after hardbake to investigate the height of the channel and shown in Figure 2.9. Our channel was 30 μm in height. These patterns are then be transferred to a PDMS microchannel device as the discussed in the next step.

PDMS Casting

The master microchannel mold fabricated using photolithography is cast onto a PDMS microfluidic device via PDMS casting. During this step 1 ml of the curing agent is mixed with 10 ml of PDMS solution. The glass slide with master mold and PDMS mixture were then degassed in a vacuum chamber for an hour. The PDMS mixture is then poured into the master mold, placed in a vacuum chamber to remove any remaining air bubbles, and then the channel is heated to 90°C for 10 minutes to complete the curing process. The settled PDMS was carefully removed from the master mold. The PDMS casting was then cleaned with DI water and ethanol. The PDMS casting was sealed with cover slip. The sample were also treated in plasma cleaner before sealing with cover slip to make stronger hydrophilic bond between cover slip and PDMS channel. To create the inlet and outlet, we utilize a hold puncher. All these steps conclude fabrication of a rectangular microfluidic channel which is1 mm wide and 30 μm deep, embedded with square arrays of micropillars, a typical pillar array with pillar radii $R = 15$ μm and lattice size $a = 40$ μm (with the closest gap thus $d = a - 2R = 10$ μm).

2.3: Realtime imaging and tracking of motile bacteria

Individual cells were visualized under an inverted microscope (Nikon Eclipse Ti) at a 60× magnification, recorded at 165 fps by a video camera (Allied Vision Pike F-032B). Here, only the cell bodies are visible under both our phase contrast and fluorescence setting. Our self-programmed software played back the high-speed video in real time and controlled the 3-axis microscope stages (Physik Instrumente PINano Piezo XYZ Stage 70 × 70 × 50 µm and Prior Scientific XY Stage 100 × 75 mm) through a USB DAQ (National Instruments USB-6211) and two stepper motor controllers (Phidgets PhidgetStepper Bipolar HC) at 100 Hz for real-time tracking (Figure 2.10).

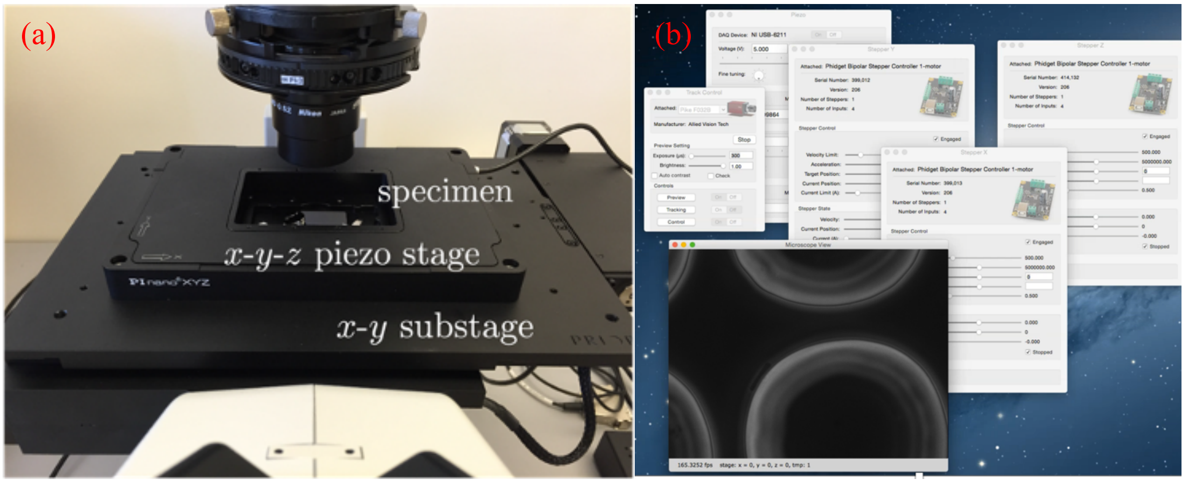

DAQ Device: NI USB-6211
Voltage (V): 5.000
Fine tuning:

Attached: Phidget Bipolar Stepper Controller 1-motor
Serial Number: 399,012
Version: 206
Number of Steppers: 1
Number of Inputs: 4
Stepper Control
☑ Engaged
Velocity Limit:
Acceleration:
Target Position:
Current Position:
Current Limit (A):
Stepper State
Velocity:
Current Position:

Attached: Phidget Bipolar Stepper Controller 1-motor
Serial Number: 414,132
Version: 206
Number of Steppers: 1
Number of Inputs: 4
Stepper Control
☑ Engaged
500.000
5000000.000
0
0.500
0.000
0
-0.000
☑ Stopped

Attached: Pike F032B
Manufacturer: Allied Vision Tech
Preview Setting
Exposure (µs): 300
Brightness: 1.00
☐ Auto contrast ☐ Check
Controls

Attached: Phidget Bipolar Stepper Controller 1-motor
Serial Number: 399,013
Version: 206
Number of Steppers: 1
Number of Inputs: 4
Stepper Control
☑ Engaged
500.000
5000000.000
0
0.500
0.000
0
-0.000
☑ Stopped

165.3252 fps stage: x = 0, y = 0, z = 0, tmp: 1

Figure 2.10: Digital tracking microscope. (a) The microscope stages of a 3D tracking microscopy were programmed by a customized software to follow individual bacterial movement. (b) A snapshot of the software interface, including a real-time microscope view (lower left).

In the free-space case, individual bacteria were tracked automatically by the tracking microscope. The lateral position of the targeted cell within the view is determined by the centroid of the binarized image, which was analyzed by our customized software in real-time. Its axial position relative to the focal plane was obtained by the intensity of the image near the centroid[29]. The microscope stages were controlled by the software [Figure. 2.10(b)] and moved against the direction of bacterial movements to accommodate its movement relative to the center of view. All raw microscope images recorded at a high frame rate (up to 210 fps) were stored simultaneously on the local drive for more detailed morphology and kinematics analyses. Figure 2.11 shows an example 3D motion of bacteria can be achieved by this automated tracking system.

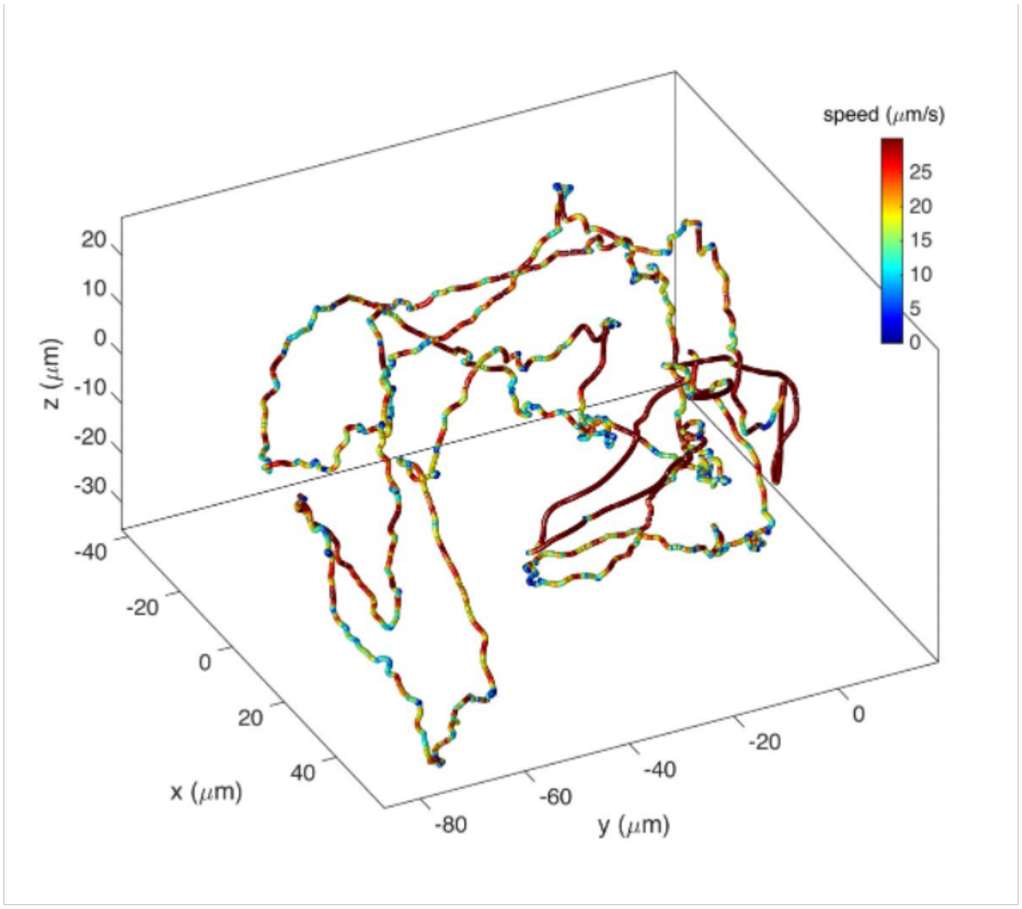

Figure 2.11: The 3D movement of a wild-type *E. coli* bacterium visualized under the tracking microscope. Colors show its instantaneous speeds.

In the presence of micropillars, the image pattern of a bacterium was expected to be shaded by the nearby pillar image, which leads to challenges in fully auto tracking. A manual control of the microscope stages using keyboards (also available with our customized software) was then applied when necessary to assist the image-based tracking algorithm for better outcomes. For *E. coli* strains that swim at about 20 μm/s, it requires at least several seconds for the targeted cell to swim out of the view (≈ 50 μm in the lateral size), and the response time in manual tracking (≈ 1 s) is sufficiently fast. In this hybrid way, we can also track individual *E. coli* in pillar arrays over a long duration (up to 10 minutes).

2.4: Trajectory analyses

From the recorded images of bacteria and micropillars, we obtained the trajectories of bacteria and their relative positions to the surrounding pillars.

To get the entire trajectory of a tracked bacterium in the x-y plane, we first capture the center of the cell body within each frame. In the free-space case, these centers can be obtained by finding the centroid of the binarized images. In the pillar case, due to the complexities in distinguishing cells from the pillar background in image analyses, we located these cell-body centers manually, using the DLTdv digitizing tool [49]. These 2D positions of bacteria in the reference frame of the camera were stored in the data array as $\mathbf{r}_{b,c}(t)$ (at given time t).

Meanwhile, the positions of the microscope stages were recorded by our tracking software, which gave the positions of stages relative to the camera view as $\mathbf{r}_{s,c}(t)$. Combining these two types of positions led to the relative position of bacteria to the microscope stage (or the surrounding media) as

$$\mathbf{r}_b(t) = \mathbf{r}_{b,c}(t) - \mathbf{r}_{s,c}(t) \tag{2.1}$$

The position of the microscope stages at each frame was also used to generate a full view of pillars navigated by individual cell. All those frames that contain the same set of pillars were offset by their corresponding positions (in the lab frame of reference) and merge into an extended map that explored by individual bacteria. The location of every pillar $\mathbf{r}_p$ in this extended map was obtained by tracking the center of circular objects, which was used to find the relative position of bacteria to nearby pillars.

To characterize the transport behaviors of each individual bacterium, we computed the mean squared displacement (MSD) from its constructed trajectories $\mathbf{r}_b(t)$. For any elapsed time Δt, we find the corresponding displacement along the trajectories with all possible starting positions, i.e., $\Delta\mathbf{r}_i(\Delta t) = \mathbf{r}_b(t_i + \Delta t) - \mathbf{r}_b(t_i)$, where indices i correspond to all possible starting positions. The MSD at given Δt is thus

$$\mathrm{MSD}(\Delta t) = \langle \Delta\mathbf{r}_i(\Delta t)^2 \rangle_i. \tag{2.2}$$

Here, symbol $\langle . \rangle_i$ means an average over all indices i. This MSD analysis can be performed the same way using path length s instead of time t, leading to an MSD as a function of elapsed path length, i.e., MSD(Δs). To minimize the end effect, we showed the MSD values only for those elapsed lengths shorter than half of the entire trajectories. As an advantage of computing MSD against path lengths, this MSD(Δs) eliminates the noisy dependence on time due to variation in cell speeds, illustrating more fundamental roles played by geometries.

Once we obtained these MSD curves, the corresponding transport characteristics can be further categorized by their power-law exponents α, by fitting them with a power-law dependence, i.e., Δs^{α}. The exponent $\alpha = 1$ corresponds to a purely diffusive movement, with $\alpha < 1$ and $\alpha > 1$ corresponding to the subdiffusive and the superdiffusive cases, respectively. To obtain such exponents, we first took the logarithms of both the MSD and the elapsed length Δs. The slope of a linear fit of these logarithms gave the value of α, which typically falls in the range between 0 and 2.

With the periodicity of the pillar lattice, we can view the responses of bacteria to every pillar within one unit cell. Every trajectory point in the pillar array can be mapped to such a unit cell by first locating the closest pillar. The corresponding position in that unit cell is thus

$$\mathbf{r}_b'(t) = \mathbf{r}_b(t) - [\mathbf{r}_p], \tag{2.3}$$

where $[\mathbf{r}_p]$ corresponds to the location of the pillar that gives the shortest distance to $\mathbf{r}_b(t)$, ie., shortest $|\mathbf{r}_b(t) - \mathbf{r}_p|$.

These unit cell trajectories $\mathbf{r}_b'(t) = (x_b'(t), y_b'(t))$ can also be binned within a two-dimensional grid for obtaining the distribution of bacteria around a pillar within one unit cell. To compute this distribution, we first convert these continuous position data $(x_b'(t), y_b'(t))$ into integers (m, n) as

$$m = \text{Floor}\ \{[x_b' - \text{Min}(x_b')] / [\text{Max}(x_b') - \text{Min}(x_b')] \times M\}, \tag{2.4}$$
$$n = \text{Floor}\ \{[y_b' - \text{Min}(y_b')] / [\text{Max}(y_b') - \text{Min}(y_b')] \times N\}, \tag{2.5}$$

where $M \times N$ is the size of the 2D grid for binning the data. These integer pairs lead to a count of each possible set Count (m, n), which is then normalized by the total number of trajectory points to get the distribution.

2.5: An agent-based model

To understand the fundamental roles played by micropillar arrays on bacterial transport, we introduced a 2D agent-based model (in collaboration with Dr. Ajay Gopinathan), which regard a bacterium as a self-propelled point-like particles[50]. For simplicity, we consider fixed speed of each agent. Its interactions with the surrounding media and the corresponding responses are implemented through geometric rules in its kinematics. The equation of motion satisfied by such an agent is

$$\text{d}\mathbf{r}/\text{dt} = \mathbf{v}, \tag{2.6}$$

which is to be solved iteratively. At the ith step, this equation can be discretized as

$$\mathbf{r}(t_i + \Delta t) = \mathbf{r}(t_i) + \mathbf{v}\,\Delta t \tag{2.7}$$

For uniform swimming speed, time no longer matters, and the above equation can be further simplified as

$$\mathbf{r}(s_i + \Delta s) = \mathbf{r}(s_i) + \mathbf{n}\,(s_i)\ \Delta s, \tag{2.8}$$

where **n** is a unit vector along the direction of swimming. The direction of this unit vector is given by an orientation angle θ that satisfies

$$\theta(s_i + \Delta s) = \theta(s_i) + \Delta\theta(\mathbf{r}, \mathrm{t}) + \mathrm{d}\theta, \tag{2.9}$$

where $\Delta\theta(\mathbf{r}, \mathrm{t})$ is the change of orientation due to the geometric rules and $\mathrm{d}\theta$ is a random noise term (due to rotational diffusivity) can be determined from experiments (Appendix D.2). In the case of swimming without self-reorientation capability, the geometric rule $\Delta\theta(\mathbf{r}, \mathrm{t})$ is determined purely by the geometries of surrounding media (Appendix D.2).

Chapter 3: Geometric effects induce anomalous size-dependent active transport in structured environments

3.1: Motivation

Structural features of environments have been recently shown to have a significant impact on the motility phases of active matter systems[19–23,51–55]. However, much less is known about how the interplay between variations in individual particle geometry and environmental structure affects macroscopic transport. For motile bacterial systems, in particular, such effects [24,25,31,38,39]can have implications for tunable transport in structured habitats. These implications arise because bacteria come in a variety of shapes and sizes across species[56–58] and even within a single strain[59–61]. It has been suggested that such widely distributed shapes and sizes are a consequence of adaptation to a diversity of features in their environments ranging from mechanical properties to nutrient availability[56]. In particular, the optimization of transport or dispersal is known to provide a strong selective pressure for bacterial morphology evolution[29,56,62,63]. For bacteria that live in structured or porous environments such as soil or tissue [64,65], proximity to a surface involves a whole host of physical interactions. These include hydrodynamic[26–28], electrostatic[66], and steric[35] forces as well as flow induced effects[24,39], which could affect transport in a geometry dependent manner[38,67,68]. Here we study the possibility that the interplay between minor, intrinsic variations in the geometry of swimmers and structural features of the environment could lead to significant transport effects at the macroscopic scale.

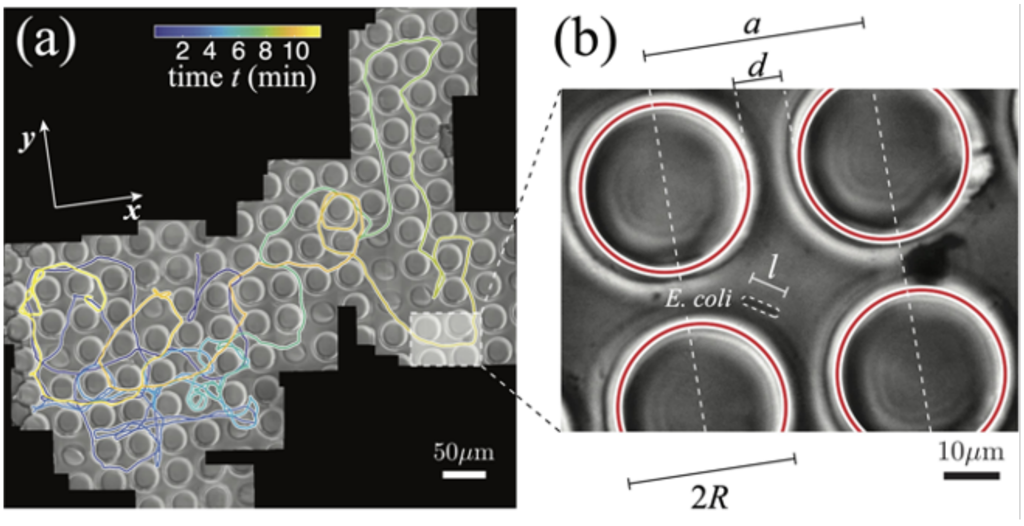

Figure 3.1: Simultaneous large-scale and high-resolution study of bacterial transport in a micropillar array through active tracking and image stitching. (a) The trajectory of a single *E. coli* (tracked up to ∼1 mm in distance and ∼10 minutes in time) was reconstructed to

characterize its long-term transport. The trajectory is color coded in time. (b) The high resolution that was preserved in each original frame in Figure. 3.1 (a) provided the detailed cell and pillar geometry. The pillars were $R = 15\ \mu$m in radius, arranged in a square lattice with a lattice constant of $a = 40\ \mu$m, and a gap of $d = a - 2R = 10\ \mu$m between adjacent pillars. The tracked bacterium (in a dashed contour) was $l \approx 6\ \mu$m in length.

One of the main challenges for such a study is that, in a standard microscope setting, a freely moving individual cell can only be observed, with adequate resolution of individual geometry, over a length scale similar to that of the cell size ($\sim 10\ \mu$m). Meaningful statistics for its long-range transport over the millimeter scale is therefore hard to obtain. Here, we resolved this issue by following individual bacteria via a tracking microscope, where the microscope stage is adjusted in real-time to recenter the cell of interest in the field of view as discussed in chapter 2[29]. To provide a structured environment, we fabricated a rectangular microfluidic channel discussed in chapter 2.

To focus on purely geometrical effects on transport that are applicable to generic active matter systems, we used a smooth swimming *Escherichia coli* strain, HCB437, which avoids any potential active response by the bacteria switching between run and tumble phases[12]. Additionally, this strain shows a natural length variation from $2 - 10\mu$m between individuals allowing us to examine the effects of microscopic geometry on macroscopic transport. We visualized the transport of these bacteria through the pillar array at a high (60× or 100×) magnification over millimeters by reconstructing trajectories. This was done by stitching together single image frames during the course of tracking as shown in Figure. 3.1(b). Even though the tracked bacterium navigates the pillar array over a long distance, its detailed movement and orientation can still be resolved by visiting every single frame with a submicron resolution (Figure. 3.1(b)).

3.2: Tracking individual bacteria in micropillar arrays

We first examined in detail the trajectories of several bacteria with different sizes. Independent of size, bacteria are constrained to move within the open spaces between pillars and the presence of noise leads to an overall diffusive trajectory at long times. However, we noticed two qualitatively different modes of motility depending on size. Short cells ($2 - 5\ \mu$m), on the one hand, frequent the pillar surfaces and move mostly in circular patterns, due to effective hydrodynamic trapping [27,28,67] by the pillar array (Figure. 3.2). Distinct from a plane-wall-induced circulation [26], this circulation around the pillar is bidirectional, regardless of the chirality embedded in the flagellar filaments (Figure. 3.3). Longer cells, on the other hand, appear to escape from such traps, resulting in more persistent movement along the directions of two orthogonal lattice vectors (here, x- and y-axes) (Figure 3.2(a). Thus, longer cells, despite feeling an increased confinement, showed an anomalous increase in their net transport.

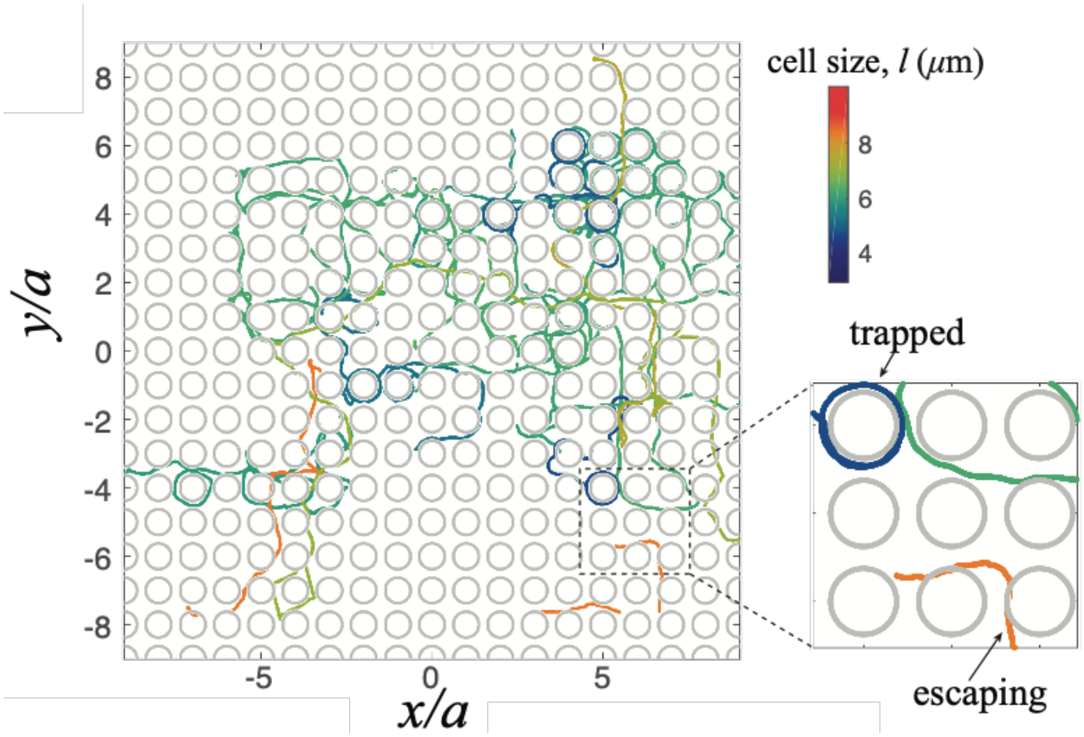

Figure. 3.2: Cell size-dependent trapping and escaping effects. Multiple trajectories for different individuals (color coded by cell length l) are mapped to the same pillar array. The shorter cells tend to circulate around the pillars while the longer cells tend to navigate between the pillars, indicating the distinct trapped and escaping mechanisms, respectively (highlighted in the inset).

3.3: Pillar-induced trapping

The circulation of bacteria that we observed here is also distinguishable from those circular motions of bacteria subjected to a nearby solid surface[26]. In those surface-induced circulations, the direction of circulation is pertinent to the flagellar chirality and is thus unidirectional. For instance, the circulation of *E. coli* near a bottom coverslip is always in the clockwise direction (viewed from the top) due to lefthanded flagella. However, in a micropillar array, a bacterium can circulate around a pillar in either direction, depending on its initial orientation when approaching the pillar surface. Figure 3.3 shows such a bidirectional circulation of bacteria around micro-pillars. In addition to the bistability, the dominating curvatures in a pillar-induced circulation also match the pillar radii, which is distinct from the circulation next to a nearby surface.

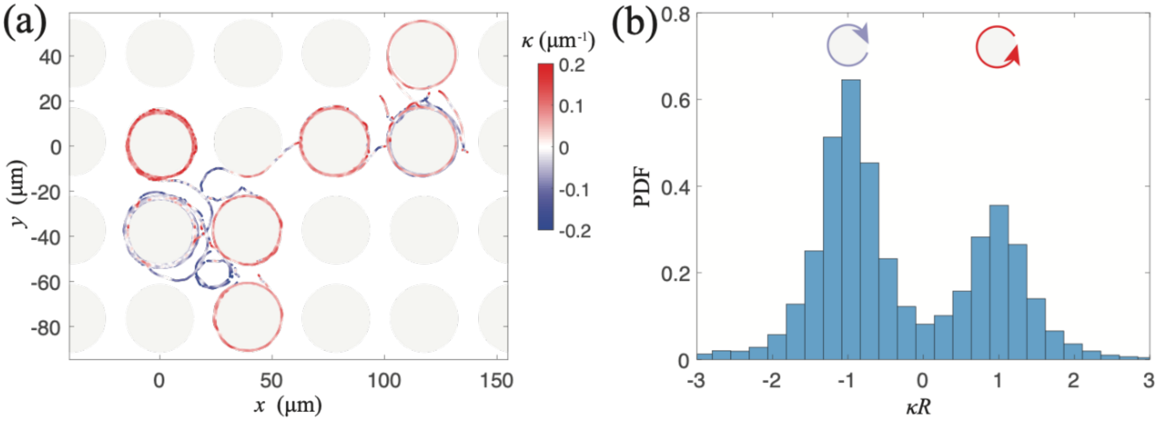

Figure 3.3: Bi-directional circulation of bacteria around pillar surfaces. (a) As shown by the local curvature κ of the trajectory, the same bacterium can circulate a micropillar in both clockwise (blue) and counterclockwise directions (red), as viewed from the top. (b) The probability density function of the normalized curvature κR (sampled every 0.2 μm along the path) shows such a bistability in circulation directions. The slight asymmetry in the distribution is potentially subjected to a nearby bottom surface, which leads more stable clockwise circulations.

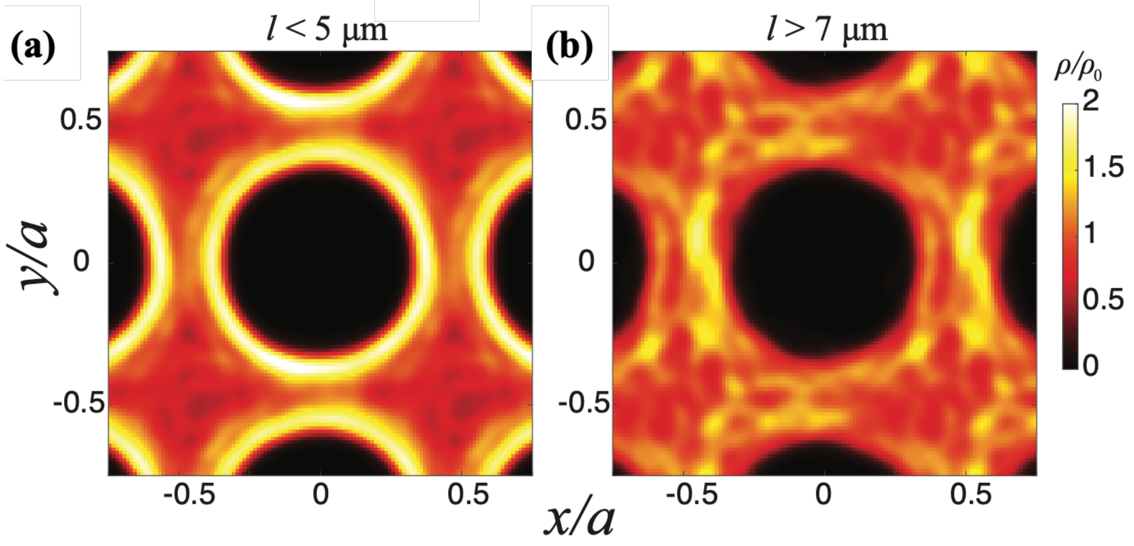

Figure 3.4: (a) Probability distribution ρ of the shorter cells (l < 5 μm), normalized by a uniform density ρ0, shows an effective enhancement at the pillar surface. (b) A similar plot for longer cells (l > 7 μm) shows the opposite effect.

To further quantify these distinct effects of the pillar array on bacteria with different sizes, we computed the probability distribution of the centers of bacteria in space within a single unit cell. As shown in Figure. 3.4 (a) and (b), shorter bacteria are concentrated near the pillar surface (consistent with a hydrodynamic attraction[24]), while longer cells spend more time in the channels, confirming a size-dependent trapping effect.

A volume exclusion due to the finite cell body size can potentially cause a size-dependent distribution of bacteria near pillar surfaces similar to what we observed experimentally (Figure 3.5a and 3.5b). If that is the case, the front of cell body will be closer to the pillar center than its center. As shown in Figure 3.5, both the center and the front of the cell body show a similar radial distribution within one unit cell, which rules out the potential contribution of volume exclusion to the size-dependent effect that we observed.

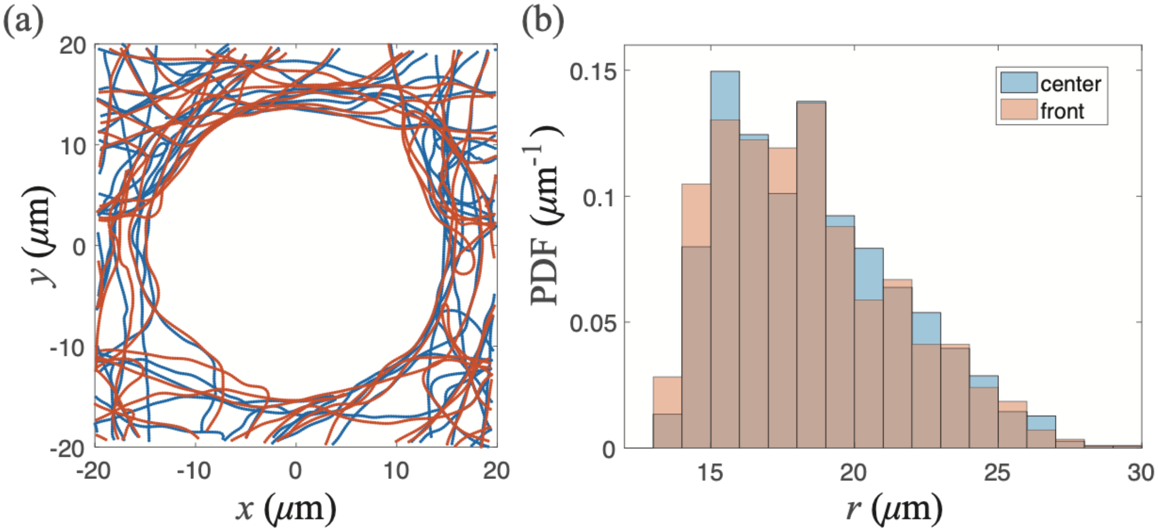

Figure 3.5: Potential volume exclusion effect (due to finite cell lengths) in the bacterial distribution near the pillar surface. (a) Two example trajectories of the same *E. coli* cell are obtained by tracking the center of the cell body (blue) and its front (red). Both trajectories are mapped into one unit cell of the pillar lattice (a = 40 μm, R = 15 μm). (b) The probability distribution functions (PDF) from these trajectories are shown as a function of the distance to the pillar center (r). Here the length of the cell body is 5.8 ± 0.2 μm.

The size-dependent distributions of bacteria near pillar surfaces (shown in Figure 3.4 (a) and 3.4(b) can be further illustrated by averaging the concentrations ρ along angular directions γ and showing the corresponding radial distributions $\langle\rho\rangle_\gamma$. These radial distributions normalized by a uniform density ρ_0 are shown in Figure 3.6(a).

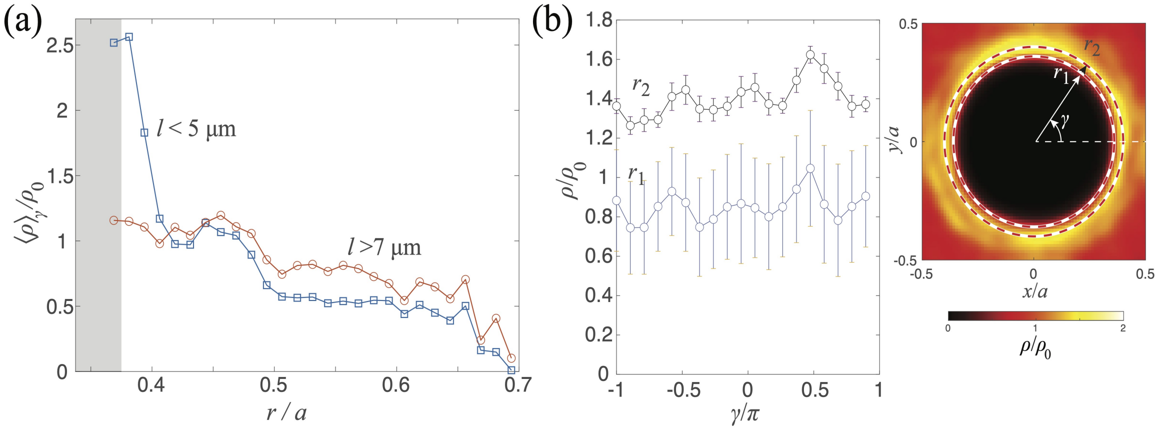

Figure 3.6: Heterogeneous cell concentrations near pillar surfaces. (a) The averaged radial distribution of *E. coli* (Fig. 2b and 2c) shows a higher concentration adjacent to pillar surfaces for shorter cells. The shaded area corresponds to the pillar region (with its radius $R = 0.375a$). (b) Distribution ρ is shown as function of the angular position γ about a pillar at different radii (r_1 and r_2) for the same pillar geometry ($R = 0.375a$). The inset shows the locations of these radii in the corresponding 2D distribution of *E. coli* (with their cell body lengths 2 μm $< l <$ 7 μm). All distributions here are normalized by their values in the uniform case, ρ_0.

Again, the concentration of the shorter cells ($l < 5\ \mu$m) near the pillar surfaces (denoted by the shaded area) are much higher than that of the longer cells ($l > 7\ \mu$m), consistent with the geometry-induced escaping for longer cells. In addition to the heterogeneity along the radial direction, the distribution of bacteria near a pillar is anisotropic. Figure 3.6 (b) shows such a fluctuated cell concentration along a pillar's annulus. The peaks of the fluctuation coincide with location of the attractive zones as predicted by the geometric model discussed in the next section.

3.4: Geometric constraints on smooth-swimming bacteria in micropillar arrays

To understand the mechanism governing the size-dependent distribution, we considered the geometric constraints on a swimming bacterium due to neighboring pillars. For simplicity, the bacterium is regarded as a rod-shaped pusher of length l_p, which is the effective hydrodynamic size set by the flow profile of the entire swimmer including the cell body (of length l) and the flagella (Figure. 3.7a, inset). Such a pusher tends to circulate around a single pillar in its natural state (without any neighboring pillars), due to the known hydrodynamic attraction between a solid surface and a generic pusher swimmer, including both bacteria and synthetic micro swimmers [34,68]. In the presence of the neighboring pillars, the allowable pusher sizes are restricted, with the maximum length $l_{p,\max}$ determined by the geometry (Figure. 3.7 a). In addition to the length constraint, a pusher is also subjected to hydrodynamic interactions from the neighboring pillars. Here, we consider a pusher circulating in the counter-clockwise direction and assume the pusher's orientation is always tangential to the pillar surface that it is circulating around. Depending on the orientation of the pusher relative to the pillar lattice (denoted by angle γ), the pusher may experience a torque from the nearest-neighbor pillar that either promotes or inhibits its circulation around the pillar. Such distinct effects are determined by the orientation angle θ_p of the pusher relative to the surface normal of the nearest-neighbor pillar (Figure. 3.7 a). Here, we consider only the normal component of the hydrodynamic force from the pillar, associated with the anisotropic drag coefficients in the presence of a nearby wall[26,69]. For $\theta_p < 0$, the normal force from the nearest-neighbor pillar provides a torque that tends to tip the pusher toward the center of the pillar it is circulating around, leading to an effective attraction to the pillar surface. For $\theta_p > 0$, the torque due to the nearest-neighbor pillar tends to tip the pusher further away from the center causing the pusher to escape (likely along the tangent to the pillar surface). Considering the tangential components of the forces does not alter the directions of these torques, as long as the drag coefficient normal to the pillar surface dominates. It should be noted that we only treated the above pusher in a resistive-force-type manner to signify the geometric roles played by the nearest-neighbor pillar. More qualitative and quantitative insights of the hydrodynamic interactions require resolving the flow field associated with a full pusher model including no-slip boundaries with pillar geometries[27]. The details of this geometrical model are discussed in appendix D.1).

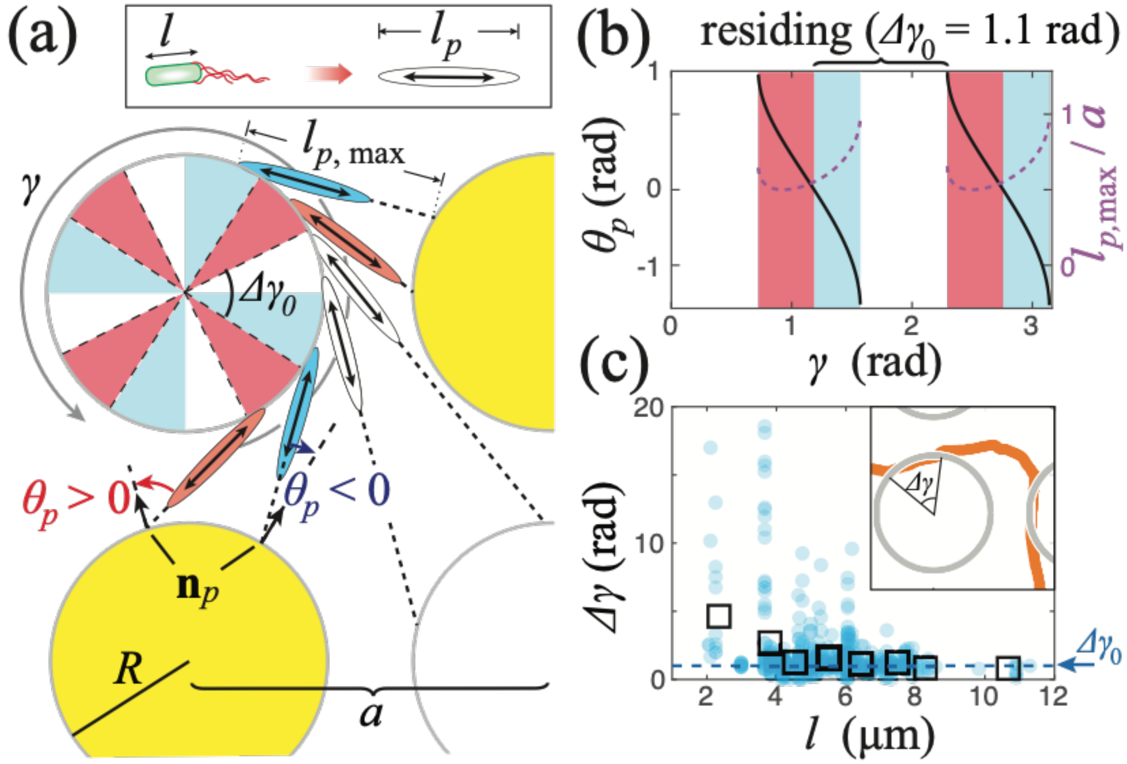
(a)
l
l_p
$l_{p,\max}$
γ
$\Delta\gamma_0$
$\theta_p > 0$
$\theta_p < 0$
$\mathbf{n}_p$
R
a
(b)
residing ($\Delta\gamma_0$ = 1.1 rad)
θ_p (rad)
1
0
-1
0
1
2
3
γ (rad)
1
0
$l_{p,\max} / a$
(c)
20
10
0
$\Delta\gamma$ (rad)
$\Delta\gamma$
$\Delta\gamma_0$
2
4
6
8
10
12
l (μm)

Figure. 3.7:. Lattice-constrained bacterial residency on the pillar surface. (a) A "pusher" representation of the bacterium (inset, with a cell body length l and a total pusher length l_p) illustrates the geometric constraints for a bacterium circulating around a pillar (at angular position γ). An elongation of l_p to $l_{p,\max}$ (the greatest possible l_p without intersecting neighboring pillars) shows that the adjacent pillar (yellow) can either provide a positive (blue) or a negative (red) contribution to the circulation, demarcated by the orientation (θ_p) of the pusher relative to surface normal of a neighboring pillar $\mathbf{n}_p$. This leads to periodically attractive ($\theta_p < 0$ or without adjacent neighbors; blue or white) and repulsive ($\theta_p > 0$; red) zones on a pillar. (b) A computation of θ_p (solid lines) and maximum $l_{p,\max}$ (dashed lines) give rise to a residency arc angle $\Delta\gamma_0 = 1.1$ rad (for $a = 40$ μm, $R = 15$ μm). (c) The residency arc angles $\Delta\gamma$ (squares), averaged over individual residency events (filled circles), decrease with increasing l and eventually to values below the size of the attractive zone γ_0 (when $l \gtrsim 10$ μm), confirming suppressed circulation for longer cells.

3.5: Size-dependent trapping and escaping

This nearest-neighbor effect leads to a series of alternating attractive and repulsive zones along the perimeter of the pillar (with $\gamma \in [0,2\pi)$), determined by the sign of θ_p. Figure (3.7 b) shows the calculated θ_p and $l_{p,\max}$ for a counter-clockwise circulating pusher and a pillar lattice that is consistent with the experimental setting ($R/a = 0.375$). The attractive ($\theta_p < 0$)

and repulsive ($\theta_p > 0$) zones are shaded in red and blue, respectively. Zones that lack any constraints from the nearest-neighbor pillar (in white) are also considered attractive, due to the natural circulating state of pushers (in the absence of the neighboring pillars). This result shows four continuous attractive zones (blue plus white) along the perimeter of the pillar, with each spanning an arc angle $\Delta\gamma_0 = 1.1$ rad, centered near $\gamma = 0$, $\pi/2$, π, and $3\pi/2$, respectively.

To facilitate a more quantitative comparison between the experiment and the theoretical picture, we measured a residency arc angle $\Delta\gamma = \gamma_f - \gamma_i$, which is the difference between the two angles where the bacterium enters (γ_i) and escapes (γ_f) the vicinity of the pillar surface (Figure. 3.7c, inset). The bacteria continuously circulates the pillar over an arc subtending this angle without leaving the surface. The experimental residency arc angles $\Delta\gamma$, plotted against cell lengths l, are shown in Fig. 3.7c. At short cell lengths ($l \lesssim 4$ μm), $\Delta\gamma$ can span over larger angles ($\Delta\gamma > 2\pi$), corresponding to the presence of multi-turn circulations. As l increases, $\Delta\gamma$ becomes restricted only to small angles (e.g., $\Delta\gamma \lesssim \pi$ for $l \gtrsim 7$ μm). Such a restriction in the distribution of $\Delta\gamma$ is responsible for the decrease in its mean with increasing l. For sufficiently long l ($l \gtrsim 10$ μm), the mean $\Delta\gamma$ falls beneath the size of the computed attractive zone ($\Delta\gamma_0 = 1.1$ rad), consistent with a highly constrained pusher that is unable to bypass any repulsive zones (as required for circulations beyond a single attractive zone).

To validate the geometric effects due to neighboring pillars, we examined the residency of *E. coli* on pillar surfaces in an extreme array geometry with its lattice size $a = 70$ μm while retaining the same pillar radii ($R = 15$ μm). The gap between any adjacent pillars becomes $d = a - 2R = 40$ μm, much longer than the longest cell observed in this study. Here, we focus on the residency angles $\Delta\gamma$. Compared to the short gap ($d = 10$ μm) case, the size-dependency in bacterial residency on pillar surfaces vanishes within the range of cell body lengths in this study (Figure 3.8). The relatively longer cells ($l > 7$ μm) that are previously unable to circulate around any pillars ($\Delta\gamma \lesssim \pi$ at $d = 10$ μm) can now circulate over multiple turns with this increased gap size ($d = 40$ μm). However, the variation in residency (due to this new gap size) is insignificant for relatively shorter cells ($l < 4$ μm). These results thus suggest a constraint of neighboring pillars on bacteria circulation that is sensitive to the relative size of bacteria (including cell bodies and flagella) compared to pillar gaps and thus further validate our geometric model.

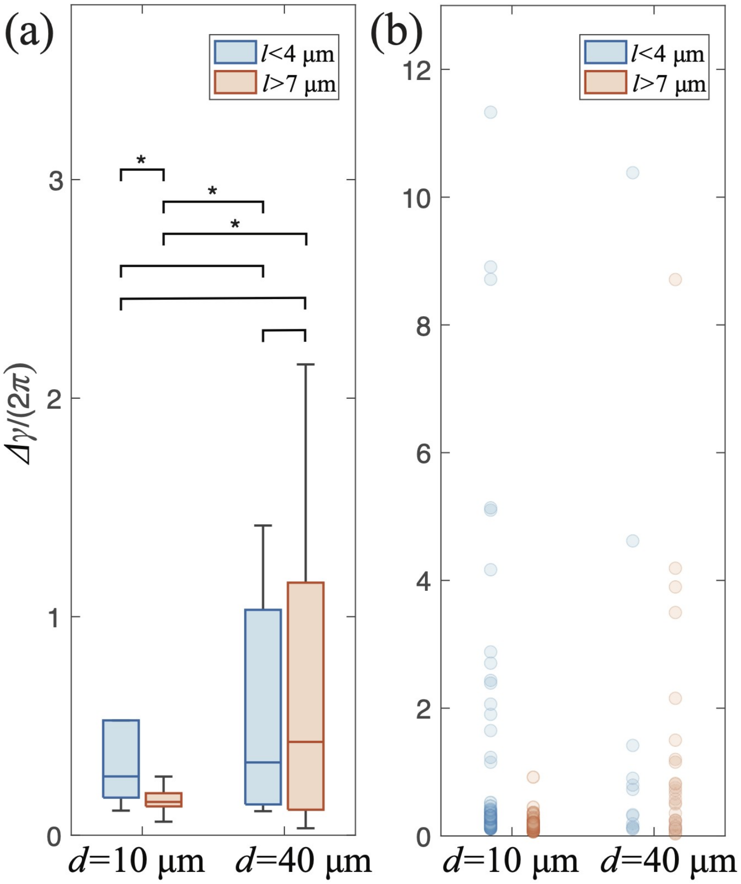

Figure 3.8: Validating the neighboring-pillar effects on size-dependent bacterial trapping. (a) The box plots of the residency angles $\Delta\gamma$ of *E. coli* (normalized by a full turn 2π) are shown for both short ($l < 4$ μm) and long cells ($l > 7$ μm) under two sets of pillar geometries (with gaps between adjacent pillars $d = 10$ and 40 μm). With this increased gap, the resident angles for long cells are significantly higher while the difference for short cells is insignificant. An asterisk (‘*’) above the link between two data sets indicates a significant difference (here, with its p-value $< 10^{-3}$) from a two-sample t-test (with a Kolmogorov–Smirnov test showing the same result). (b) The corresponding residency angles for the box plots shown in (a) also illustrates a suppressed trapping for long cells ($l > 7$ μm) when subjected to small pillar gaps ($d = 10$ μm). The sample size of each column of data (from left to right) is 66, 85, 13, and 34, respectively.

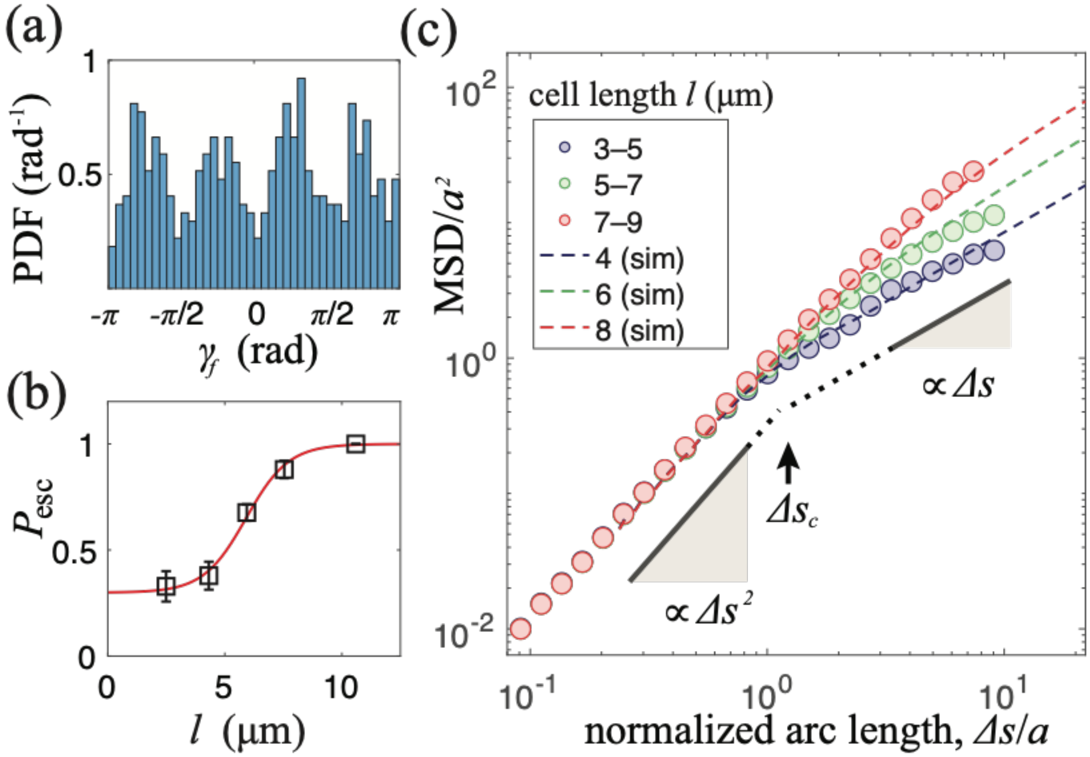

Figure. 3.9: Size-dependent escaping and global diffusivity. (a) The non-uniform distribution of angles of escaping (γ_f, illustrated in Fig. 3c, inset) shows more probable escaping of bacteria along the diagonals (i.e., $k\pi/4$ with $k = \pm 1, \pm 3$) of the square lattice, consistent with the locations of the repulsive zones. (b) The escaping probabilities P_{esc} are calculated from bacterial trajectories for different cell lengths l (open squares with error bars representing the standard errors). The solid curve corresponds to a fit with a hyperbolic tangent function. (c) The mean squared displacement (MSD) as a function of the path length (Δs) exhibits a transition from a ballistic regime (MSD $\propto \Delta s^2$) to a diffusive one (MSD $\propto \Delta s$) for both experiments (circles) and numerical simulations with the corresponding P_{esc} (dashed lines). The size of the ballistic regimes, depicted by a ballistic length Δs_c (arrow), increase with l or P_{esc}, consistent with the geometry-induced escaping for longer cells. All lengths in trajectories are normalized by lattice size a.

To further validate our model, we investigated the statistics of the angles, γ_f, at which bacteria escaped the pillar surface. The probability density function (PDF) of γ_f shows peaks near the diagonal directions of the pillar lattice (Figure. 3.9a), consistent with the predicted locations of the repulsive zones (Figure. 3.7b). This highly anisotropic distribution of γ_f also justifies the use of a single escaping probability P_{esc} (within all repulsive zones only) for characterizing the size-dependent geometric effects. Such an escaping probability is consistent with the stochastic nature of the competition between both the hydrodynamic attraction from the orbited pillar and the “repulsive” contribution from the nearest-neighboring one, associated with the fluctuating orientation and location of a micro swimmer. If we consider that bacteria only escape within repulsive zones, P_{esc} can be obtained as

$$P_{esc} = \frac{N_e}{N_z}, \tag{3.1}$$

where N_e and N_z correspond respectively to the number of escaping events and the number of repulsive zones that bacteria cross during their travel along the pillars’ perimeters. Noting that the angular separation between the centers of two adjacent repulsive zones is $\pi/2$ and neglecting the detailed escaping locations, the number N_z is given by

$$N_z = \sum_{i=1}^{N_e}\left(\left[\frac{2\Delta\gamma_i}{\pi}\right]+1\right), \tag{3.2}$$

where i corresponds to the index of an escaping event and $[\cdot]$ denotes the integer part of a number. The escaping probability is thus the inverse of an ensemble average (denoted by $\langle\cdot\rangle$), i.e.,

$$P_{esc} = \langle[\frac{2\Delta\gamma}{\pi}+1]\rangle^{-1} \tag{3.3}$$

We computed this probability P_{esc} from experiments for different groups of cell body lengths l. As shown in Figure. 3.9b, there is a transition from a low escaping probability ($P_{\mathrm{exc}} \approx 0.3$) for relatively shorter cells ($l \lesssim 5\ \mu$m) to a high escaping probability ($P_{\mathrm{exc}} \approx 1$) for relatively longer ones ($l \gtrsim 7\ \mu$m). A hyperbolic-tangent fit of the experimental data yields a function (solid curve in Figure. 3.9b)

$$P_{esc}(l) = P_0 + (1-P_0)\tanh\,(l - \frac{l_c}{\Delta l}) \tag{3.4}$$

with the critical cell body length $l_c = 6.0\ \mu$m demarcating the distinct escaping behaviors.

3.6: Anomalous size-dependent transport

To show how this geometric effect manifests itself in the long-time transport of bacteria, we (in collaboration with Dr. Ajay Gopinathan) simulated bacterial trajectories by a kinematic model (using the above $P_{\mathrm{esc}}(l)$): a bacterium that reaches a pillar surface stays on the surface and continues circulating the pillar if it is within an attractive zone or it escapes with a probability P_{esc} if it enters a repulsive zone (in red in Figure. 3.7 b). Here, we assumed that a bacterium moves at a constant speed u, which is a fairly good approximation for the non-tumbling mutant (Appendix: Figure. D.2.2).

We then computed the corresponding mean squared displacement (MSD) for comparison with the experimental data (Figure 3.9c). To secure optimal convergence, the MSD values were binned by path lengths Δs and sampled over all trajectories within the same size l group. For all experimental MSD (dots in Figure. 3.9c), cell body lengths l (3 - 9 μm) were grouped every 2 μm to secure a sufficient number ($\gtrsim 20$) of long trajectories ($\gtrsim 200$ μm) within each size category. All data points with less than 10 sampled trajectories were excluded. Each simulated MSD of the corresponding l (dashed line in Figure. 3.9c) was computed over 100 model swimmers with each of them traveling $400\times a$ in total path length s from a random starting position. As shown in Figure. 3.9c, the simulated MSD reproduces well the characteristics of bacterial transport. In both experimental and simulated results, each MSD-Δs curve contains a ballistic regime for small Δs and a diffusive regime for large Δs. The size of the ballistic regime can be characterized by a ballistic length Δs_c (Figure. 3.9c), set by the crossover point between two distinct scaling regimes for transport (with MSD exponents $a = 1$ and $a = 2$). Interestingly, the ballistic length $\Delta s_c/a \approx 1$ for relatively shorter cells, reminiscent of the effective reorientation time scale $\tau = a/u$ for point-like particles diffusing in obstacle networks[70,71]. While converging at short Δs, the long-time MSD-Δs curves are noticeably higher for longer cells, corresponding to longer ballistic lengths Δs_c at longer cell lengths l and thus suggesting a finite-length effect. Again, longer cells, despite feeling an increased confinement, display an anomalous increase in their MSD due to the geometric effects of the neighboring pillars. These quantitative agreements between the experiment and theory further confirm the dominant role played by geometry.

3.7 Discussions:

Our study illustrates the role of individual morphology in the transport of active particles in general and bacteria, in particular, through periodic structured media. In living systems, this surprising enhancement of transport for longer cells, combined with a maximal cell size set by interstitial spaces of the lattice, suggests an optimal cell size potentially determined by the geometry of a porous environment[56,62,72]. Similar geometry-sensitive effects in transport of wild-type strains may already be present, but not explicitly identified, in other studies of bacterial transport[25]. Generalizing our geometric effects to such 3D environments will enable targeted design of environmental geometry for desired size-dependent transport and collective motion[10,31,73]. For a non-periodic lattice, it is expected that the above geometric effect still applies in general, since any geometric constraints due to nearest-neighbor pillars always tend to influence the longer cells first before they can influence shorter cells. However, the location and size of the repulsive zones, as well as the critical cell-body length now vary for each pillar, leading to more complex escaping zones and thus more complex global cell kinematics. Also, in the extreme case that multiple pillars are within the vicinity, a long cell will be more easily jammed as it requires more room for reorientation, contributing to another type of geometric constraint. These potential effects due to disorder in the crystalline structure of the environment will be investigated in our future work.

Our findings also indicate that the transition between localized and dispersive modes is sharp and occurs at a critical value of bacterial size, controlled by the porous environment. Bacteria with typical sizes near this critical value may be able to access both modes of transport by adaptive change in their size based on the local nutrient conditions or other desired transport needs. This suggests, for example, an unexplored benefit of filamentation under starvation conditions in *E. coli*, in addition to others that have been proposed in the literature[74–76]. Our results also have implications for the spatial structure of naturally occurring bacterial colonies in structured environments where spatial location within the colony could be correlated with age dependent cell-size, due to differential transport.

In nature, patterned structures with periodic lattices are widely found on antibiofouling surfaces, such as cicada wings [77] and shark skins [9]. The geometric effects we have identified thus provide a new perspective for revisiting these microscale structures in relation to their antibiofouling effects. Conversely, our work also suggests ways to engineer surfaces so as to either increase or decrease the residency of different bacterial strains with slightly different sizes or even differentiating age structured populations, which may also be of interest in biofouling applications. Such ideas could also be applied to designing environments for the desired sorting or guiding of synthetic micro swimmers as well as the geometric design of individual swimmers.

Chapter 4: Run and tumble in structured media

4.1: Motivation

Self-reorientation is an essential feature of motile microorganisms, which enables their translocation to optimal living environments. In the case of a flagellated bacterium, such as *E. coli*, self-reorientation can be realized through a short "tumbling" duration between two adjacent "running" sections, with the cell body oriented in almost random directions. Our previous study shows that microstructure geometries can be used as a tunable knob to manipulate the transport of a smooth-swimming bacteria mutant, which lack the capability of self-reorientation. How this self-reorientation capability of bacteria in their natural state, e.g., the tumbling of wild-type *E. coli* bacterium, affects their transport in structured media remains to be illustrated.

4.2: Residence of run-and-tumble bacteria on pillar surfaces

Here, we introduced a wild-type *E. coli* strain (ATCC 25922GFP) that runs and tumbles to an array of micropillars, sitting on a square lattice (with pillar diameter *d* = 30 μm and lattice size a = 40 μm). By following individual bacteria using the digital tracking microscope (DTM) and stitching together their microscope images, we reconstructed their

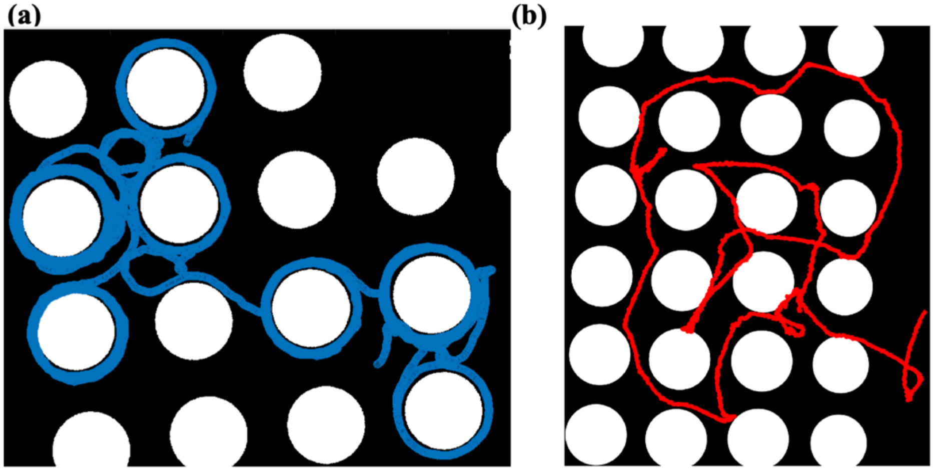

Figure 4.1: Effect of active reorientation on bacterial trajectories in micropillar arrays. (a) The trajectory of a smooth-swimming mutant *E. coli* is composed of many circles due to its circulation about individual pillars. (b) A GFP *E. coli* (wild type) bacterium often encounters abrupt changes in swimming directions, leading to a random walk like trajectory without any circular paths. Here the pillar diameter *d*=30 μm and lattice size *a*=40 μm.

long-term trajectories and compared the result with that of the smooth-swimming mutant cells. While the smooth-swimming mutant cells (at about 5μm in cell body length) are often found circulating about individual pillars [Figure. 4.1 (a)], the wild-type cells at similar body lengths stay near the pillar circumferences over much shorter durations, accompanied by frequent escaping from pillar surfaces [Figure. 4.1 (b)]. For the smooth swimming mutants, smooth curves in bacterial trajectories are intercepted by their contact with nearby pillar surfaces, followed by circular motions along the pillar circumferences. However, in the wild-type case, smooth trajectory segments are joined together by abrupt cell reorientations that occur near and away from the pillar surfaces due to occasional tumbling events. Among these self-reorientations, those near the pillar surfaces lead to additional escaping events compared to the non-tumbling mutant case. Moreover, not all escaping events from the pillar surface are accompanied by self-reorientations. These tumble free instances are reminiscent of the "forward scattering" responses of wild-type *E. coli* to obstacles[38].

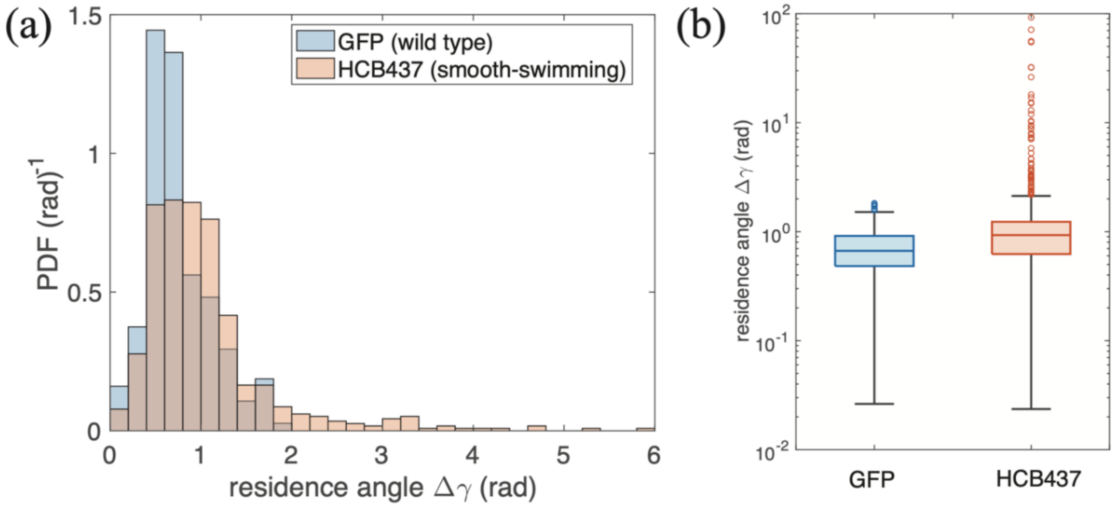

Figure 4.2: The residence of bacteria along the pillar circumferences is reduced self-reorientation capability. (a) The residence angle of the wild-type *E. coli* strain (GFP, in blue) exhibits a narrower probability distribution function (PDF) as compared to the smooth-swimming mutant (HCB437, in orange) case. (b) The data in (a) are shown in the box plot, with circles (data beyond the box-plot analysis) showing the full range of residence angles for both the GFP and the HCB437 strains. The total numbers of residence angles of these two cases (GFP and HCB437) here are 297 and 390, respectively.

From the trajectories of individual cells near the pillar surfaces, we measured a residence angle Δγ, an angular displacement relative to the center of the regarded pillars with bacteria continuously moving along pillar circumferences. A histogram of such residence angles is shown in Figure. 4.2(a). Consistent with the more frequent escaping events, the residence angles are much reduced for the wild-type strain, compared to the mutant case at similar cell-body lengths (2 - 6 μm). The full ranges of the residence angles for both cases are shown along with their box plots [Figure. 4.2(b)]. The residence angles of wild-type strains are strictly within a small angle $\Delta\gamma \lesssim 3$ rad, without any observations of full-circulation instances (i.e., $\Delta\gamma = 2\pi$). On the contrary, the residence angles for the smooth-swimming mutant span over a much wider range, associated with the long-term circulations.

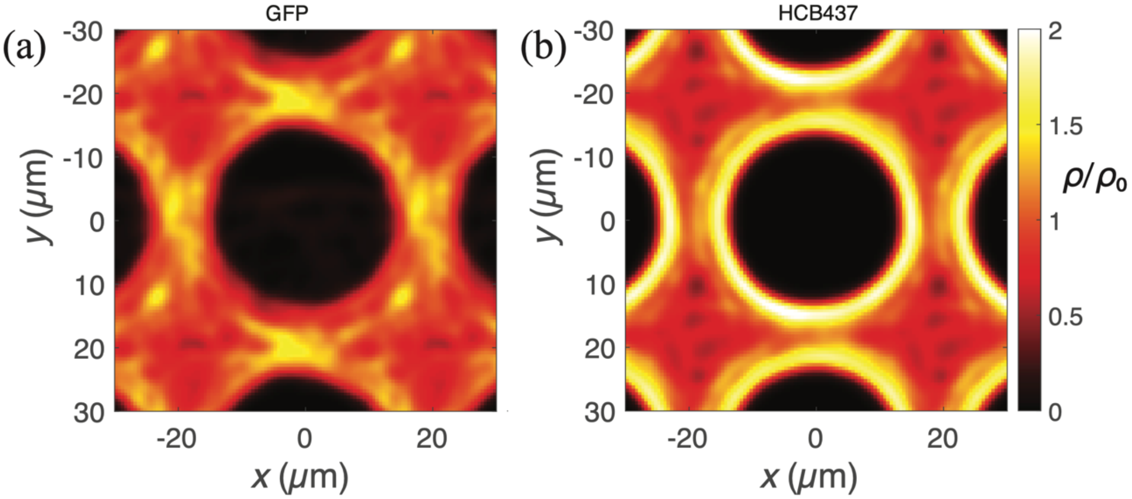

Figure 4.3: Probability distributions of bacteria within a unit cell of the pillar lattice are compared between the wild-type and smooth-swimming strain. (a) The probability distribution function ρ (normalized by its mean ρ_0) of the wild-type *E. coli* strain are shown in colors within a unit cell. (b) Similar plot for the smooth-swimming mutant.

This reduced residence on pillar surfaces for the wild-type strain also accounts for its dissipated distribution within the vacant area among pillars. Figure 4.3 (a) shows the distribution ρ of wild-type *E. coli*, normalized by its uniform distribution ρ_0 and mapped into one unit cell of the pillar lattice. The spots in bright colors between adjacent pillars show the locations at peak concentration where bacteria are most likely to be found. However, the smooth swimming mutant cells (of similar cell body lengths) are highly concentrated near the pillar surfaces, forming a ring-like pattern around each pillar in the concentration plot [Figure 4.3 (b)], consistent with its long residence on pillar surfaces in the absence of tumbling.

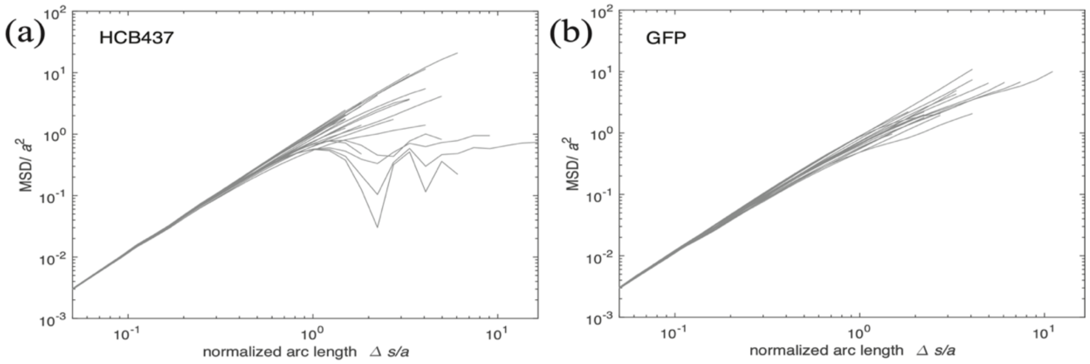

Figure 4.4: Effects of self-reorientation on the long-term bacterial transport in a micropillar array. (a) The MSD of a smooth-swimming mutant (HCB437) is shown against its path length, with each curve corresponding to one individual track. (b) MSD plots for the wild-type (GFP) cells of the same range of body lengths (2 – 5 μm) show a narrower distribution. All length scales here are normalized by the lattice size a=40 μm. The sample sizes of these two cases (HCB437 and GFP) here are 38 and 17, respectively.

4.3: Effects of tumbling on transport in micropillars

To examine how these additional escaping activities affect the overall bacterial transport in structured media, we computed the mean-squared displacement (MSD) from trajectories. These MSD data are plotted against path lengths Δs to minimize the noise associated with variations of individual swimming speeds and focus on the geometric effects of structured media [78]. As shown in Figure. 4.4, all MSD data collapses at a path length shorter than the lattice size a (i.e., $\Delta s < a$), with a power-law exponent $\alpha \approx 2$, showing the dominating ballistic transport within that length scale. For increased path lengths ($\Delta s > a$), the power-law exponent α decreases, associated with the increasing diffusive component in long-term transport. However, these MSDs are highly diverse in the smooth-swimming mutant case [Figure. 4.4 (a)], associated with a mixture of superdiffusive ($\alpha >1$) and subdiffusive processes ($\alpha < 1$). In the extreme case with bacteria trapped to pillars, their MSD values fluctuate due to circulating motion around pillars, leading to even negative power-law exponent. We attribute these varying effects of microstructures to the variation of individual cellular features, e.g., cell body lengths, here, $2 < l < 5$ μm, as we discussed in the previous chapter [78]. However, introducing the self-reorientation capability by replacing the above mutant with the wild-type strain appears to restrict the distribution of MSD curves at long path lengths ($\Delta s > a$), giving rise to a narrower distribution of the power-law exponent α around the pure diffusive case ($\alpha \approx 1$).

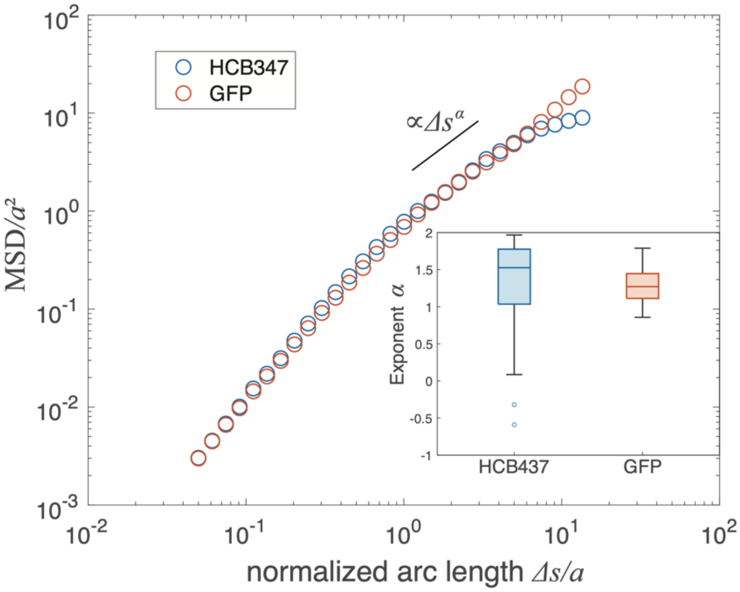

Figure 4.5: MSD curves averaged over all ensembles of the smooth-swimming mutant (HCB347) and the wild-type *E. coli* (GFP) for similar cell body lengths (2-5 μm) show almost negligible effects from bacterial tumbling. However, with a similar mean transport behavior, the long-distance ($\Delta s > a$) power law exponents α are more scattered in the HCB347 case, as shown in box plots (inset).

A more thorough comparison of the mean MSD curves between the mutant and wild type shows almost negligible effects from including self-reorientation (in the wild-type case). As show in Figure. 4.5, both cases exhibit a crossover region between the short-range ballistic ($\alpha \approx 2$) and the long-range diffusive ($\alpha \approx 1$) behaviors at a length scale close to the lattice size, i.e., $\Delta s \approx a$. While sharing similar mean behaviors, the transport characteristics due to individuals is more diverse in the smooth-swimming mutants (HCB347), accompanied by a much wider distribution of the power-law exponents α by fitting the crossover behavior at $a < \Delta s < 3a$ (inset of Figure. 4.5). Rather than simply promoting escaping from circulations about pillars through self-reorientations, the wild-type strains have an even slightly lower mean value of the exponent α as compared with the smooth-swimming mutants (especially at short $\Delta s < a$), which can be attributed to those extra random reorientations via tumbles before bacteria encounter pillar surfaces. However, these extra reorientations of the wild-type cells effectively prevent them from being trapped to any single pillar and eventually diminish those extremely low α instances (e.g., $\alpha \approx 0$) as found in the smooth-swimming mutant case. Both these effects of additional reorientations on bacterial movements near and far from pillars thus potentially cancel each other in the overall transport behaviors. The additional noises in a self-reorienting bacterial system, here, from tumbling activities, surprisingly contributes to more regulated long-term transport characteristics, e.g., with more deterministic exponents α in the MSD curves.

4.4: A geometric model accounting for self-reorientations

To examine whether the above cell-reorientation effects are sufficient to determine the subtle difference in the long-term transport between the smooth-swimming and tumbling strains, we visited a purely geometric model and simulated each bacterium as a self-propelling agent. A non-tumbling version of this model has been applied successfully to the smooth-swimming mutant in pillar arrays, which shows decent agreement with experiments on bacterial transport [78]. In such models, an agent is moving at constant speed and following geometry-based rules associated with its relative location to the nearby pillars. To account for the tumbling capability of the wild-type strain, we introduced additional random reorientations along the trajectory of each agent, representing the tumbling events. These reorientation events were prescribed by a Poisson process, with mean path lengths between adjacent reorientations agreeing with experimental observations, here approximately 20 μm, equivalent to a tumbling rate on the order of 1 Hz, based on the average swimming speed of *E. coli* (≈ 20 μm/s). The moving direction after each reorientation is randomly generated among all possible angles, i.e., $[-\pi/2, \pi/2]$ relative to the norm of the pillar circumference when the agent is circulating about the pillar or $[0, 2\pi)$ when the agent is away from any pillars.

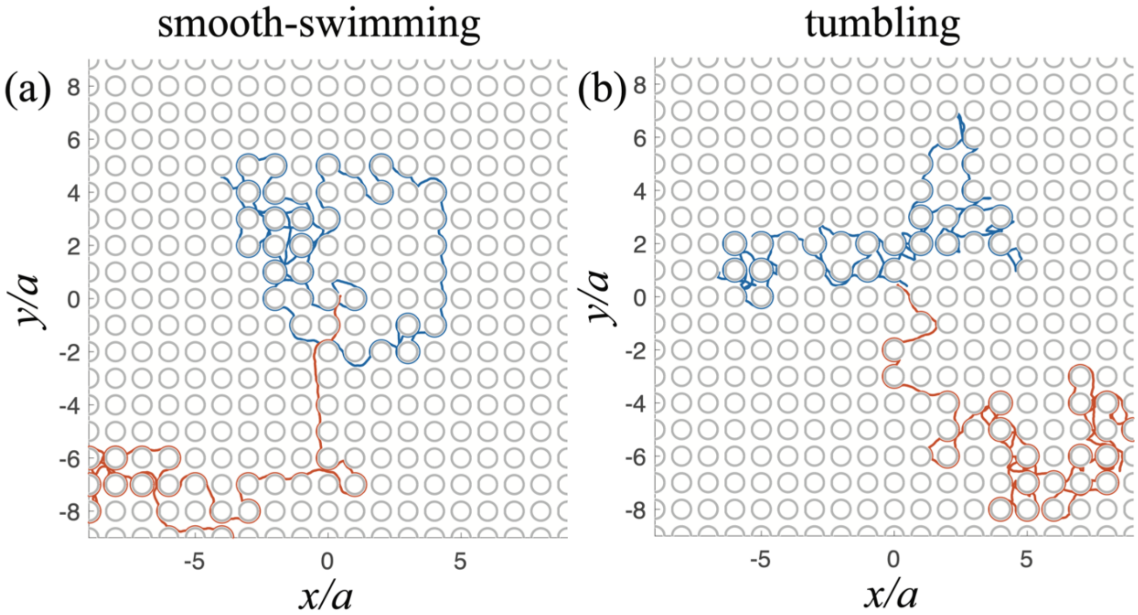

Figure 4.6: Simulating bacterial trajectories in micropillar arrays with an agent-based model under smooth-swimming (a) and tumbling (b) conditions. Micropillars with diameter d = 30 μm and array lattice size a = 40 μm are represented in circles. Solid lines in different colors correspond to the simulated trajectories of individual agents. For each trajectory, a total path length of $400a$ is shown.

Examples of simulated trajectories for smooth-swimming and the tumbling agents are shown in Figure. 4.6. While both cases can be represented by a diffusive trend at the long-range scale (with path lengths much greater than a), the tumbling ones [Figure. 4.6 (b)] are accompanied by sharp reorientations absent under the smooth-swimming condition [Figure. 4.6 (a)], reminiscent of actual trajectories of *E. coli* observed in our experiments (Figure. 4.1). It is worth noting that our simulations still revealed occasional circulations of the tumbling agents about pillars, which were much less likely to occur in the corresponding bacterial systems. This discrepancy suggests that a spatially and temporally uniform tumbling may not fully capture the difference between the smooth-swimming and the wild-type strain.

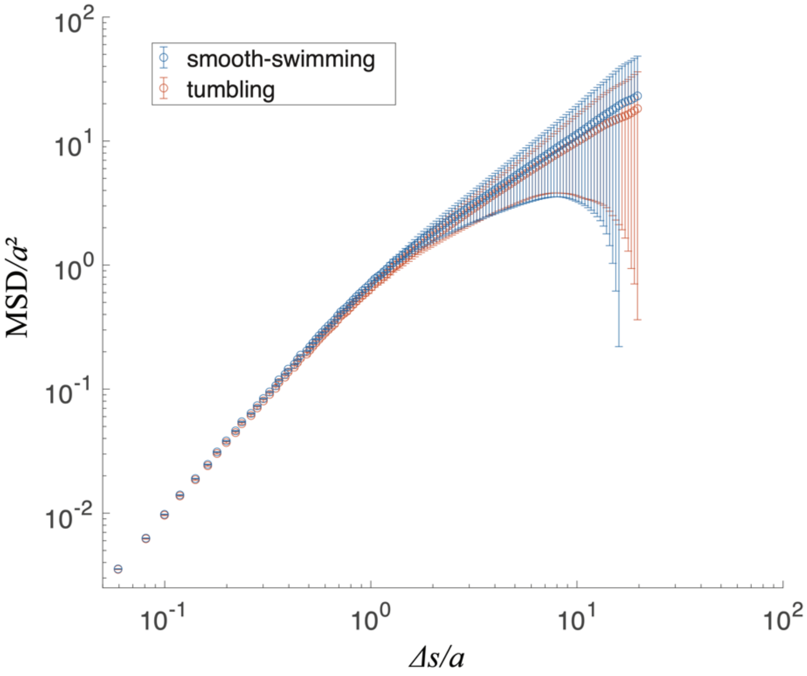

Figure 4.7: A comparison of the simulated MSD curves under both the smooth-swimming (blue) and tumbling (red) conditions. The error bars correspond to standard deviations among 100 sampled trajectories in each case.

Similar to the previous analyses of the experimental data (Figure. 4.5), we computed the MSD values from the simulated trajectories for both the smooth-swimming and the tumbling agents and plotted them against the path lengths. As revealed by the simulated MSD curves (Figure. 4.7), introducing additional reorientations (through tumbling) does not necessarily promote the overall transport of these agents. Given the geometric parameters associated with the relatively short cell body lengths (2 – 5 μm) here, the tumbling agents indeed possess a slightly lower MSD at large scales ($\Delta s > a$), consistent with our experimental observations. Furthermore, as indicated by the standard deviations in the MSD curves (Figure. 4.7), such a slight reduction in transport is accompanied by a suppression of both those extremely low and high power-law exponent cases, which again agrees with our experimental results.

4.5: Transport of tumbling cells in micropillars and free spaces

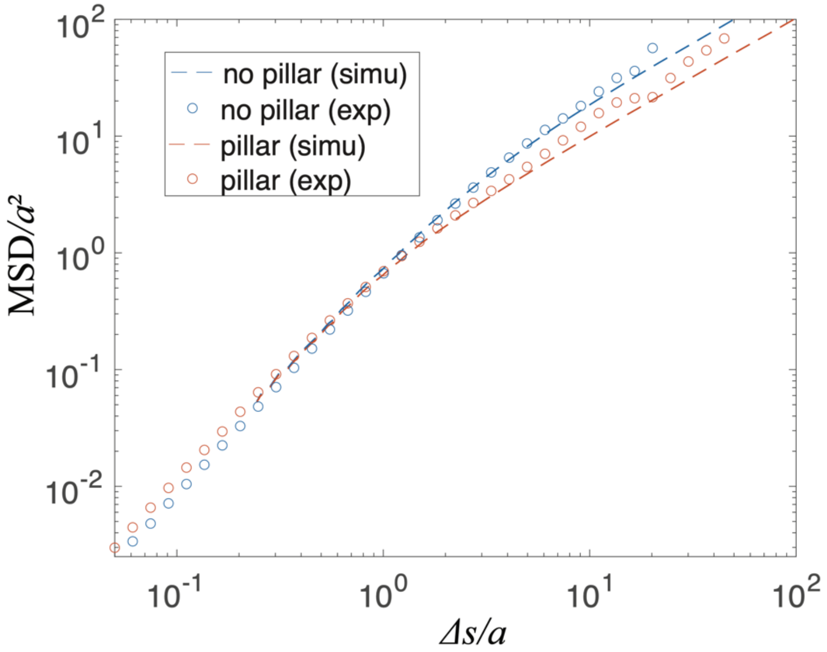

Figure 4.8: Comparing the MSD curves with and without pillars shows the direct impact of pillar arrays on the transport of wild-type *E. coli*. Experimental data are shown in open circles. The predictions from the agent-based model are shown in dashed lines.

To obtain quantitatively the effect of micropillars on the transport of wild-type *E. coli* that are capable of self-orientation, we compared the MSD of these bacteria in micropillar arrays with that in free spaces. In experiments, these free-space environments were achieved using an empty microfluidic channel that incorporates the same geometry as those filled with micropillars. The long-term trajectories in free space were obtained by automatically following individual cells in 3D using the DTM[29]. We note that all trajectories within a small gap (< 5 µm) from the top or bottom substrate were considered subjected to boundary effect [26] and were thus excluded from the MSD analyses. By plotting MSD curves side-by-side for both the pillar and free-space cases, we found that removing these constraints from pillars gave rise to increased transport over a length scale beyond the lattice sizes *a* (Figure. 4.8). Simulations with the above numerical model not only revealed a similar trend for the tumbling agents but also agreed with the experimental data quantitatively well, without any needs for fitting parameters (Figure. 4.8). This surprisingly decent agreement suggests the importance of geometries since our model does not requires any knowledge of the detailed cell-structure interactions but utilizes only the geometric constraints from environments on individual agents.

4.6: Discussions

Here, we supplement our understanding of active transport in microscale structures by including the self-reorientation capabilities (e.g., through tumbling) to the otherwise smooth-swimming bacteria that are likely to be trapped by these structures. To our surprise, these additional reorientations played a nontrivial role in bacterial transport through an array of micropillars, which altered both the effectiveness of trapping near the pillars and the persistence length of trajectories away from them. Overall, these two effects lead to an averaged transport activity of a wild-type *E. coli* strain similar to that of a smooth-swimming mutant, with the latter lacking self-reorientation capabilities. While sharing similar mean behaviors, the transport characteristics of individual cells, e.g., the power-law exponents of the MSD curves, are more regulated in the wild-type case, contrary to the additional noises introduced by their tumbling activities.

Despite these complexities, we revealed that those subtle differences in transport due to tumbling could be recovered by a geometry-based model, regardless of the detailed cell-structure interactions. Besides providing qualitative predictions, this geometry-based model was also employed to obtain quantitatively the transport characteristics of wild-type *E. coli* in micropillar arrays and free spaces, which agreed decently with the experimental observations. These qualitative and quantitative agreements between experiments and simulations suggest the universal effects of geometries in bacterial transport through microscale structures.

Here, we have only considered bacteria with relatively short body lengths (2 – 5 μm) compared to the lattice size. As we demonstrated earlier, a longer bacterium can simultaneously interact with multiple pillars, which leads to size-sensitive transport for the smooth-swimming mutants. It is expected that this size dependence will also affect the transport of bacteria with self-reorientation capabilities, which we will investigate in the future.

So far, we have assumed the self-reorientation activities of wild-type bacteria to obey a Poisson process and occur uniformly in space among pillars. This simplification may result in the discrepancy between the experimental findings and simulating results, especially regarding the residence angle along pillar surfaces for the wild-type *E. coli.* We conjecture that bacteria tumble more frequently near the pillar surface compared to the free-space case, which can be implemented in our agent-based simulations. It is expected that these extra reorientations near the pillar surfaces account for more disruptions of circulating motions of wild-type *E. coli*, leading to overall smaller residence angles as we found in experiments. An experimental investigation of the spatial and temporal distribution of tumbling events will confirm whether this is the case. More specially, I will obtain the orientations of the cell body from the microscope images of each individual tumbling bacterium. The fluctuation of such orientations and its swimming speed serve together a criterium of tumbling activities[79] . These tumbling segments of trajectories will be used to show a spatial distribution of tumbling probabilities. We will use such distributions to characterize the dependence of tumbling on the distance between bacteria and pillar surfaces. These quantitative results will also be used to implement our agent-based model for the self-reorientating bacteria in the presence of microstructures.

Meanwhile, our MSD analyses do not capture any anisotropy in bacterial transport, which can be crucial to natural biological processes, especially for extending our pillar array to more sophisticated lattice geometries. Our future analyses of transport characteristics will include an angular dependence to address any directional response of bacteria transport due to anisotropies in microstructures.

Appendix:

A: Safety Measure

This study complied with all policies and precautions set out by the Environmental Health and Safety Department at the University of California, Merced. The experiment was carried out in the lab under careful adherence to the chemical hygiene regulations. A training program for chemical safety and hygiene was available at the lab. During this session, examples of the value of lab coats, eyewear, gloves, and other items were provided. As a result, safety precautions were always observed within the lab.

All biological samples used in the research were handled in biosafety cabinets. Waste that was biologically polluted was disposed of in biohazard-designated receptacles. Chemical wastes were disposed of in waste acid containers that were clearly identified. Every member of the staff was aware of the Material Safety Data Sheets (MSDS) that were stored in Dr. Liu's lab safety handbook. The lab facility contained separate fume hoods and storage areas for combustible, organic, and inorganic compounds. The types of chemicals and biochemicals utilized in the study or on hand in the lab are listed in Table A1 along with the MSDS instructions. All safety measures were implemented while this study was being conducted.

Table A1: lists the safety precautions from the MSDS for the chemicals and biochemicals utilized in our lab (Dr. Liu lab)

Name of chemical/bio-chemical	MSDS Hazards Instructions
Acetone	Highly Flammable
Ethanol	Highly Flammable
Isopropanol	Highly Flammable
Buffer Solution	May be harmful if you swallowed
Potassium phosphate monobasic	Harmful in contact with Skin
Ampicillin sodium salt	Breathing difficulties if inhaled
Sodium chloride	No Specific
Potassium phosphate dibasic	Harmful in contact with Skin

B1: PDMS Curing protocol

This protocol is written by me as a part of this thesis and is part of Dr. Liu's lab protocols.

1. Tare weigh boat
2. Mix together 1gram Sylgard 184 Elastomer curing agent/10g Sylgard 184 Elastomer base using a wooden spatula until many tiny bubbles form.
3. After about an hour, the mixture is put in a desiccator to degas until all bubbles are gone.
4. Make sure your SU-8 2015 mold is cleaned if not gently clean with ethanol and dry it before use.
5. The tape should be longer and broader than the glass slide. Put the glass slide in the tape's middle. Fold the tape's short edges around the glass after folding the tape's long edges around the glass slide. The glass slide will be surrounded by them as walls.
6. The PDMS mixture is poured into the glass-slide mold, placed in a desiccator to remove any remaining air bubbles, and then the channel is heated to 90°C for 10 minutes to complete the curing process.
7. Carefully remove the glass slide from the cured PDMS when it has had time to cure.
8. Take a 0.5mm diameter hole puncher and punch a hole into the PDMS block to make inlet and outlet
9. With the help of ethanol and DI water, the PDMS channel is cleaned.

B2: Plasma Cleaner

This protocol is written by me as a part of this thesis and is part of Dr. Liu's lab protocols.

1. Insert your dry, cleaned channel into the chamber of Plasma cleaner (Harrick Plasma).
2. Pull the knob shut.
3. To produce a vacuum, turn on the pump and run it for a minute.
4. Switch on the power and observe color within the chamber. Within a few seconds, it will become green.
5. Rotate the knob to the right.
6. Execute plasma for one minute.
7. Switch off the power and stop the pump.
8. To lower the pressure, slowly turn the knob to the left.

C: Preparation of sample used in experiment

C1: Tryptic Soy Broth Medium (TB solution)

This protocol is written by me as a part of this thesis and is part of Dr. Liu's lab protocols.

Tryptic soy Broth, TB (BD cat 236950): Dissolve 12g/400ml

1. Tare flask
2. Add 12gram of TB powder to 380 ml of DI water.
3. Autoclave for 30 minutes on liquid setting
4. Allow solution to cool down at 40 °C to 50 °C.
5. Add 20 ml 0.04 grams/20ml Ampicillin to the 380ml TB solution.
6. Solution should be kept at 4°C.
7. Do not keep for more than 7–10 days.
8. Provide your name's initials together with the sample name, date, and time of preparation.

C2: Tryptic Soy Agar Plate

This protocol is written by me as a part of this thesis and is part of Dr. Liu’s lab protocols.

Tryptic soy agar (BD cat 236950): Dissolve 8g/200ml

Making ~6 plates

1. Add 8gram of tryptic soy agar powder to 190 ml of DI water.
2. Autoclave for 30 minutes on liquid setting
3. Allow solution to cool down at 40 °C to 50 °C but not too long or it will solidify.
4. Add 10 ml 0.02 grams/10ml Ampicillin to the 190ml TB solution.
5. Pour 10 ml TB agar solution into petri dishes and let sit.
6. Parafilm the dishes side and store upside down in fridge.
7. Provide your name's initials together with the sample name, date, and time of preparation.

C3: Motility buffer (MB)

This protocol is written by me as a part of this thesis and is part of Dr. Liu’s lab protocols.

Make 40 ml of motility buffer

0.46 g Potassium Phosphate Dibasic (K_2HPO_4)
0.18 g Potassium Phosphate Monobasic (KH_2PO_4)
0.00116 g Ethylene Diamine Tetraacetic Acid Disodium Salt Dihydrate (EDTA)
0.156 g Sodium Chloride (NaCl)
40 ml of DI water (dH_2O)

1. Mix all above to make 40 ml MB.
2. Measure the pH value, it should be ~7
3. Label the container then store in 4 °C. Label should include solution name, date, pH and your initials.

C4: Preparation of *E. coli* Strain (HCB 437)

This protocol is written by me as a part of this thesis and is part of Dr. Liu's lab protocols.

The *E. coli* strain (HCB437) was grown on a plate (4% tryptic soy agar) at 30◦C after inoculation. One motile colony from the plate was transferred to a flask with 10 mL tryptic soy broth (4% tryptic soy broth), incubated on an orbital shaker (running at 200 RPM) for 16 hr at 30◦C. The sample was then diluted 500 times with tryptic soy broth and incubated for another 3.5 hr at 30◦C in the shaker incubator (at 200 RPM). After incubation, the sample was diluted 50 times, followed by a washing process: the sample was centrifuged (at 2000 RPM for 4 min) and re-suspended in a motility buffer (0.064 M K2HPO4, 0.035 M KH2PO4, 0.078 mM EDTA, 0.067 M NaCl, pH =7) for 3 times before being prepared as a specimen.

C5: Preparation of *E. coli* Strain (GFP)

This protocol is written by me as a part of this thesis and is part of Dr. Liu's lab protocols.

We used *E. Coli* (strain ATCC No. 25922GFP) as a model bacterium. The bacterium was growing on a Tryptic Soy Agar plate (4% Tryptic Soy Agar (BD cat 236950), 0.01% Ampicillin) at 30°C. One colony from the plate inoculated in 10mL of Tryptic Soy Broth (4% Tryptic Soy Broth (BD cat 211825), 0.01% Ampicillin) and incubated for 16h at 30°C and 200rpm. A 20 µL sample was diluted in 10mL Tryptic Soy Broth and incubated for 3.5 at 30℃ and 200 rpm. A 20 µL sample diluted in 980 µL Tryptic Soy Broth. The sample was centrifuged for 4 minutes at 2000 rpm. Then pellet re-suspended in motility buffer (0.064M K_2HPO_4, 0.035M KH_2PO_4, 0.078mM EDTA, 0.067M NaCl). The sample was centrifuged and re-suspend for a total of 3 washes in motility buffer before taking a sample for the experiment.

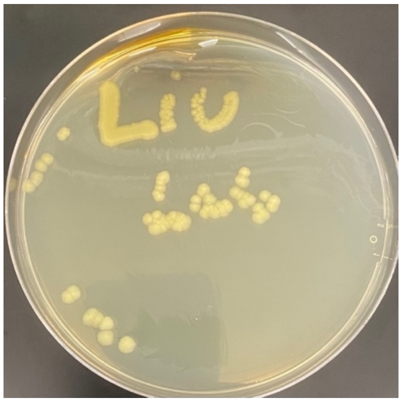

Figure C.1: A streak plate to isolate single colonies of *E. coli*

D.1: Geometric constraints

The effective attraction and repulsion of a circular pillar on a circulating bacterium are determined by the orientation of the cell relative to the nearest-neighbor pillar θ_p (Figure. 3.7). Given the lattice geometry, such an orientation can be shown as a function of the cell's position, here the angular position γ with respect to the center of the orbited pillar. We show in the following that such a function can be solved analytically.

In this analytical model, we consider the whole body of the bacterium (including the flagellar bundle) an infinitely thin rod (thick line) that is only allowed to move in the x-y plane (Figure 3.11). For a cell that orbits a pillar (centered at O and sitting on a square lattice with lateral size ($a = |\overrightarrow{OO'}|$), the leading edge of the rod contacts the pillar's circumference at the point A with an angle γ, i.e., $OA = (R\cos\gamma, R\sin\gamma)$. Here, we allow the cell orientation to deviate from the surface tangent by an incident angle θ_i [27,28]. An elongation of the rod along the trailing edge intersects the nearest-neighbor pillar (centered at O') at the point A' with an angle γ' with respect to that pillar, i.e., $\overrightarrow{OA'}$ = (a+ R $\cos\gamma'$, R $\sin\gamma'$), , subject to its geometric constraints.

The rotation of the vector AA' from the surface normal of the pillar O' is denoted as θ_p. Since $\overrightarrow{AA'} = -\overrightarrow{A'A}$, we have an identity from the above geometries:

$$\gamma' + \theta_p - \pi = \gamma - \pi/2 + \theta_i. \tag{1}$$

Considering the maximum length of the rod (without intersecting any pillar circumferences) as $l_{p,\max}$, we can represent the vector $\overrightarrow{AA'}$ by both ($l_{p,\max}, \gamma - \pi/2 + \theta_i$) in polar coordinates (with respect to A) and $\overrightarrow{OA'} - \overrightarrow{OA}$ in Cartesian coordinates, followed by the identities:

$$l_{p,max}\cos\left(\gamma - \frac{\pi}{2} + \ Q_i\right) = \mathrm{R}(a/\mathrm{R} + \cos\gamma' - cos\gamma) \tag{2}$$

$$l_{p,max}\sin\left(\gamma - \frac{\pi}{2} + \ Q_i\right) = \mathrm{R}(\sin\gamma' - sin\gamma) \tag{3}$$

Eliminating $l_{p,\max}$ from the above two equations gives

$$\tan(\gamma + \theta_i) = -\left[\frac{a}{R} + \sin(\theta_p - \gamma - \theta_i) - \cos\gamma\right] / \left[\cos(\theta_p - \gamma - \theta_i) - \sin\gamma\right] \tag{4}$$

Letting $x \equiv \sin(\gamma') - \cos(\theta_p - \gamma - \theta_i)$ and $b \equiv \cos\gamma - \frac{a}{R} + \tan(\gamma + \theta_i)\sin\gamma$,

we rewrite the above equation as a quadratic equation for x:

$$[b - \tan(\gamma + \theta_i)x]^2 = 1 - x^2. \tag{5}$$

Solving this quadratic equation gives

$$x\left(\gamma,\theta_i,\frac{R}{a}\right)=\frac{b\tan(\gamma+\theta_i)\pm\sqrt{b^2\tan^2(\gamma+\theta_i)-(b^2-1)[1+\tan^2(\gamma+\theta_i)]}}{1+\tan^2(\gamma+\theta_i)}\ . \tag{6}$$

Consequently, the cell orientation with respect to the neighboring pillar becomes

$$\theta_p=\cos^{-1}x\left(\gamma,\theta_i,\frac{R}{a}\right)+\gamma+\theta_i \tag{7}$$

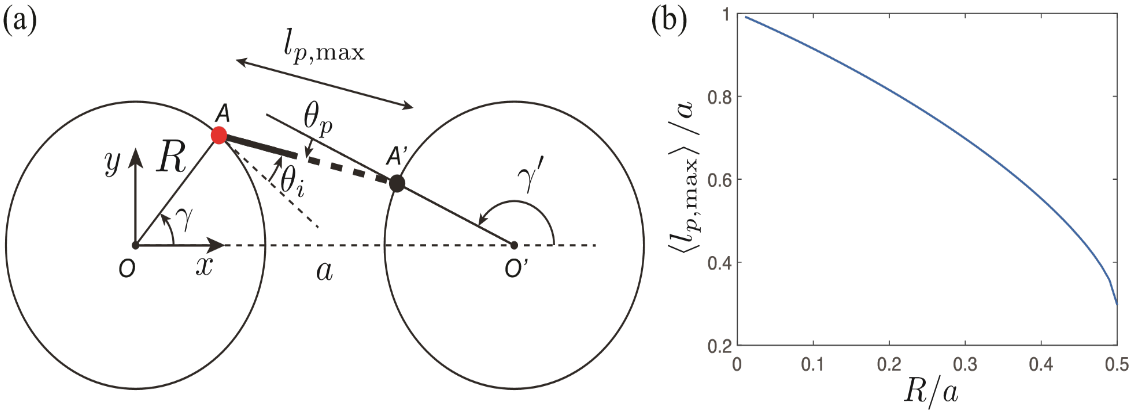

Figure D.1: Geometric constraints in a pillar lattice. (a) Here, the distance between adjacent pillars is given by the lateral size of a square lattice $a=\left|\overrightarrow{OO'}\right|$. A bacterium is simplified as an infinitely thin rod up to a maximum $\left|\overrightarrow{AA'}\right|$ that circulates around a pillar at the origin *O* along the counterclockwise direction. The cell orientation deviates from the surface tangential by an incident angle θ_i. An adjacent pillar (centered at O') enhances or interrupts the circulation of the microorganisms by providing a force along its surface normal ($\overrightarrow{O'A'}$) and hence a torque. A clockwise or counterclockwise torque is demarcated by the sign of the angle θ_p, the orientation of the cell relative to the O' pillar. (b) The computed mean maximum length $\langle l_{p,\max}\rangle$ (normalized by the lattice size *a*) is shown as a function of the lattice geometry, characterized by a dimensionless pillar radius *R/a*

and the maximum length

$$l_{p,\max}=R\frac{\sin\gamma-x(\gamma,\theta_i,R/a)}{\cos\,(\gamma+\theta_i)} \tag{8}$$

One of these two roots (Eq. 6) is associated with the intersection between $\overrightarrow{AA'}$ and the far side of the pillar, which can be ruled out easily by keeping the shorter $l_{p,\max}$.

Given that the incident angle is small, i.e., $\theta_i = 0$, we compute the mean of the above maximum length $l_{p,\max}$ over the angle γ as

$$\langle l_{p,\max} \rangle = \frac{a}{\gamma_{\max} - \gamma_{\min}} \int_{\gamma_{\min}}^{\gamma_{\max}} \left(\frac{R}{a}\right) \frac{\sin\gamma - x(\gamma, 0, R/a)}{\cos\gamma} \mathrm{d}\gamma, \tag{9}$$

where $\gamma_{\min}$ and $\gamma_{\max}$ are the lower and upper bounds for real integrand within one quadrant, which are evaluated numerically in MatLab. The dependency of $\langle l_{p,max} \rangle$ on lattice geometries (*R/a*) are shown in Fig. D1b. Example values for selected geometries, especially those of the interest in this study, are enumerated in Table D.1.

Table D.1: Mean maximum pusher sizes computed for different lattice geometries *R/a*.

R/a	⟨*lp*,max⟩/*a*
0.100	0.915
0.333	0.654
0.375	0.595
0.417	0.525
0.500	0.297

D.2: Agent-based kinematics subjected to geometric constraints

To apply these geometry-based pillar effects to cell kinematics, we neglect the slight dependency of the locations of the attractive and repulsive zones on the circulation directions (Figure. 3.7) and focus on a deterministic residency within each attractive zone and a probabilistic residency within each repulsive zone. Here, we employ an agent-based model, with the length-dependent constraint from neighboring pillars implied by a size-dependent geometric rule. For fully attractive pillars, $\Delta\theta(\mathbf{r}, t)$ in Eq. (2.9) satisfies

$$\Delta\theta(\mathbf{r}, \mathrm{t}) = \begin{cases} 0, & \text{if } |\mathbf{r} - \mathbf{r}_{\mathrm{p}}| > R, \\ -\dfrac{\Delta s}{R}\widehat{\mathbf{R}} & \text{if } |\mathbf{r} - \mathbf{r}_{\mathrm{p}}| = R, \end{cases}$$

which prescribes the agent to circulate about the pillar when within its vicinity. Here, unit vector $\widehat{\mathbf{R}}$ is along the surface norm of the pillar.

Considering the existence of the repulsive zone (especially for relatively longer cells), we let the agent either reside on the pillar surface throughout the entire repulsive zone or leave immediately upon entering that zone, determined by comparing a numerically generated random number (uniformly distributed between 0 and 1) with the given escaping probability P_{esc}. Once the cell escapes, we prescribe its swimming direction along the tangential direction of its previously orbited pillar. A white noise of small amplitude is applied to swimming directions afterwards to account for a rotational diffusion in the free-swimming direction of the non-tumbling mutant, which is extracted from the experimental trajectories (Figure D.2.1).

To characterize such rotational diffusivities in experiments, we computed the angular mean-squared displacement ($\mathrm{MSD_{rot}} = \langle(\theta - \langle\theta\rangle)^2\rangle$) from the swimming directions θ and showed it as a function of the elapsed path length Δs. Results for different cell lengths are similar (Figure D.2.1). A proportional fit of the data for all cell sizes gives a rotational diffusion coefficient $D_{\mathrm{rot}} = \mathrm{MSD_{rot}}/(2\Delta s) \approx 0.0061 \mathrm{rad}^2/\mu\mathrm{m}$. Given the typical step size in path lengths used in our simulation's $\mathrm{d}s = 0.02\times a$ (or $\mathrm{d}s = 0.8$ μm for lattice size $a = 40$ μm), we have a random-walk step in the white noise as $\mathrm{d}\theta = \pm\sqrt{D_{\mathrm{rot}}\mathrm{d}s/2} \approx \pm 0.05$ rad. Not surprisingly, applying this white noise to the simulation of free-swimming bacteria (without pillars) restores the same rotational diffusivities (Figure D.2.1).

We prescribe the attractive zones ($\theta_p > 0$ or without nearest-pillar constraints) from the calculation in the previous section. For simplicity, we consider $\theta_i = 0$ and use the averaged attractive zones from both the clockwise and the counterclockwise cases. These averaged attractive zones are thus centered at $\gamma = 0$, $\pi/2$, π, and $3\pi/2$ with respect to the center of the orbited pillar. Each agent starts at a randomly generated position and moves at a constant speed. Within the vicinity of the pillar surface (determined by the criterion that the distance to pillar center O is shorter than the O pillar radius), the agent either keeps staying on the pillar surface through circulation or leaves the surface along the tangential direction. Such binary activities are determined by whether the agent is within the repulsive ($\theta_p < 0$) or the attractive (otherwise) zones: the agent leaves the pillar with a probability P_{esc} within the repulsive zone or moves along the circumference of the pillar until it reaches the next repulsive zone.

After escaping along the direction tangential to the pillar's circumference, the bacterium moves at constant speed until it reaches an attractive or repulsive zone of the next pillar along its trajectory. A white noise in swimming direction was extracted from experimental trajectories (Figure. D.2.1) and introduced to the model swimmer when it is away from the pillar surface.

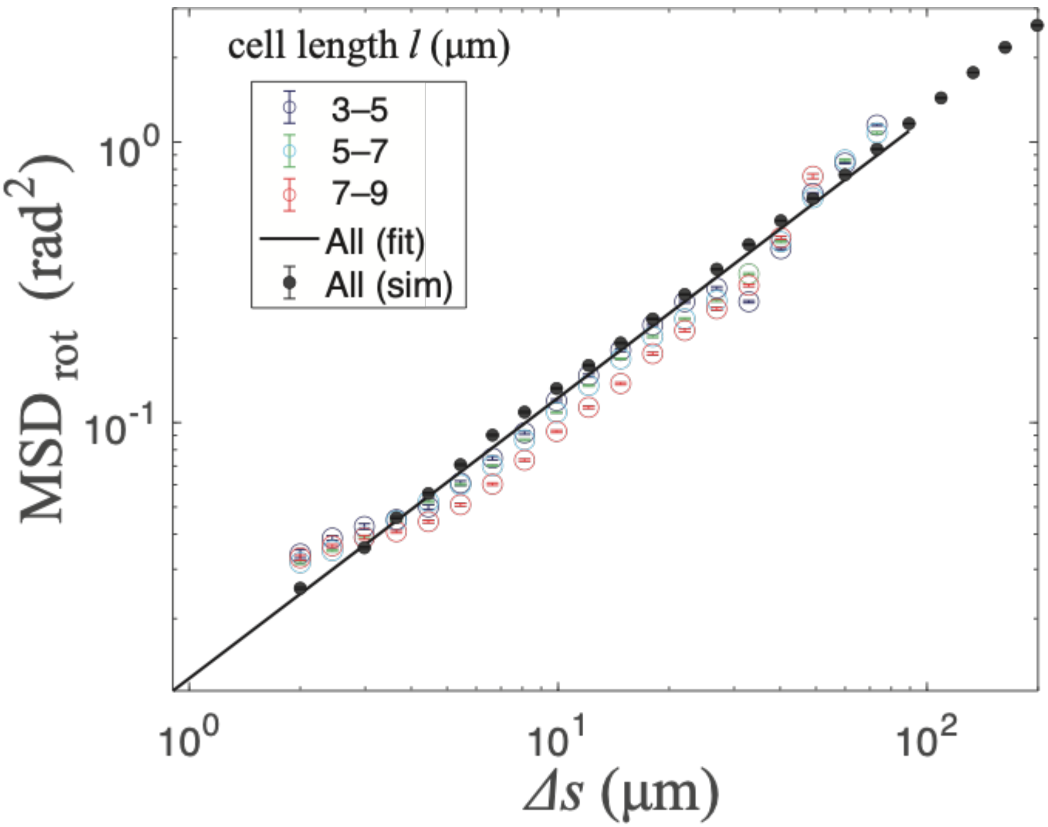

Figure D.2.1: The rotational diffusion of free-swimming bacteria. The angular mean-squared displacement ($\mathrm{MSD}_{\mathrm{rot}}$) of the swimming directions of *E. coli* is shown against the elapsed path length Δs for different cell body lengths (open circles). A rotational diffusion coefficient ($D_{\mathrm{rot}} = 12\ \mathrm{MSD}_{\mathrm{rot}}/\Delta s$) is obtained by a proportional fit (solid line) of $\mathrm{MSD}(\Delta s)$ for all cell body lengths, yielding a random-walk step in cell orientation to be used in the agent-based simulation. The simulated trajectory of free-swimming cells with the above extracted random-walk step reproduces the same rotational diffusivity (dots).

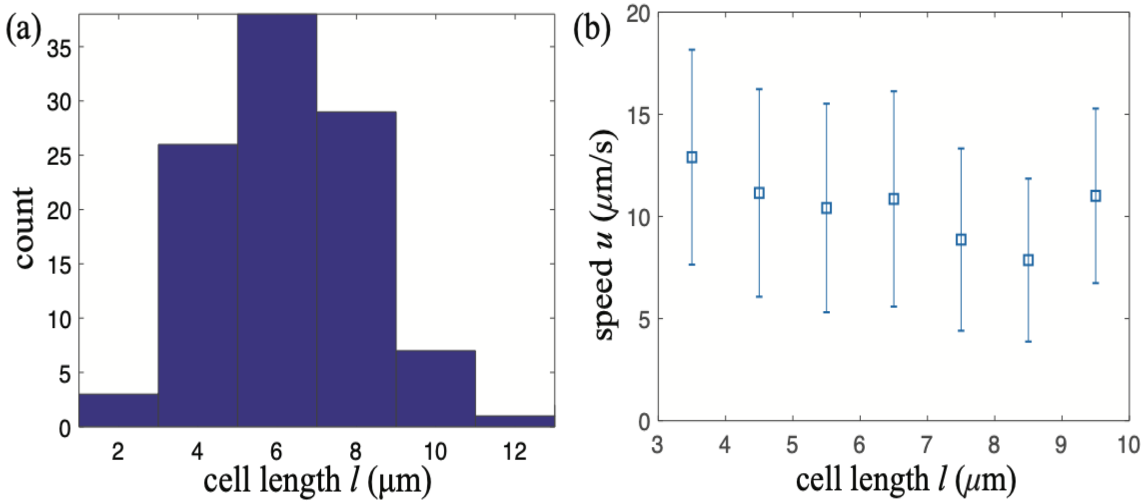

Figure D.2.2: Size and speed variations among individual cells. (a) The histogram of cell body lengths of bacteria observed in the study of a typical pillar lattice (R = 30 μm and a = 40 μm). (b) Swimming speed of *E. coli* in pillar arrays show no significant cell length (l) dependencies. Error bars correspond to standard deviations

D.3: Stochastic escaping model

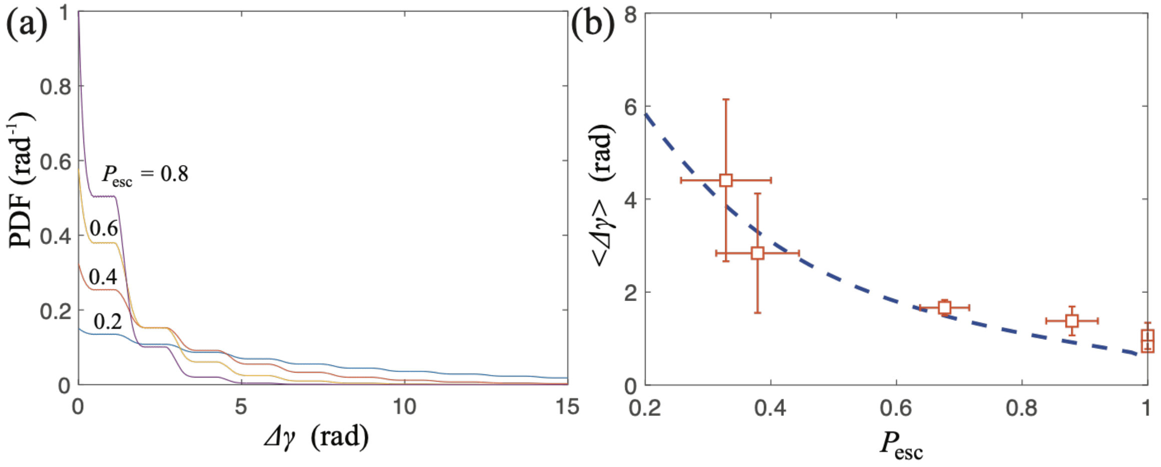

Figure D.3: Stochastic escaping of bacteria from pillar surfaces. (a) Probability density functions of residency arc angles $\Delta\gamma$ for various escaping probabilities within the repulsive zones $P_r = P_{esc}$, as predicted by a stochastic process (Eq. 15). Here, the escaping probability within the attractive zones is prescribed to be $P_a = 0$ and the distribution curves are averaged for $\gamma_i \in [0,\pi/2)$. (b) The resulting mean residency arc angles $\langle\Delta\gamma\rangle$ are shown as a function of P_{esc} (dashed line). The experimental data (squares, with all error bars indicating standard errors) are shown for comparison.

We consider a random process with the bacterium leaving its previously orbited pillar only within any repulsive zones at a uniform probability P_{esc}. The probability of finding a residency arc angle $\Delta\gamma$ can thus be represented by a Bernoulli process as

$$p(\Delta\gamma) = (1 - P_{\mathrm{esc}})^{n_r} P_{\mathrm{esc}}, \tag{10}$$

where n_r is the number of repulsive zones that the bacterium passes without exiting its circulation, i.e.,

$$n_r = \begin{cases} \left[\left| |\gamma_f - \gamma_i| - \Delta\gamma_0 \right| / (\pi/2) \right], & \text{if } \gamma_i \in \text{any repulsive zones} \\ \left[|\gamma_f - \gamma_i| / (\pi/2) \right], & \text{if otherwise.} \end{cases} \tag{11}$$

Here, γ_i and γ_f are respectively the initial and final angular position of a circulation, $\Delta\gamma_0$ is the size of an attractive zone (Figure. 3.7), and the symbol $[\cdot]$ corresponds to the integer part of a number. It is worth noting that the model so far ignores the detailed position where a bacterium enters (γ_i) or leaves (γ_f) the pillar surfaces and the potential finite escaping probability within the attractive zones. Given the binary escaping probabilities within attractive and repulsive zones (P_a and P_r respectively), we show in the following that the above result can be further generalized to a more realistic escaping model. For simplification in the derivation, we represent the probability that a bacterium moves along the pillar surface for a small angular displacement $\delta\gamma$ by $p_{a,r} = e^{-\nu_{a,r}\delta\gamma}$, with index a or r denoting the type of zones (attractive or repulsive, respectively). Matching the probability that a bacterium escapes within a single attractive P_a or repulsive zone P_r, we have

$$P_{a,r} = \sum_{j=1}^{N_{a,r}} e^{-j\nu_{a,r}\delta\gamma} \left(1 - e^{-\nu_{a,r}\delta\gamma}\right), \tag{12}$$

where $N_{a,r}$ is the number of discretized angle elements $\delta\gamma$ within an attractive (N_a) or a repulsive (N_r) zone. We thus have in the continuum limit

$$P_{a,r} \xrightarrow{\delta\gamma \to 0} 1 - e^{-\nu_{a,r}\Delta\gamma_{a,r}} \tag{13}$$

or

$$\nu_{a,r} = -\ln(1 - P_{a,r})/\Delta\gamma_{a,r}, \tag{14}$$

where $\Delta\gamma_{a,r}$ is the size of a single attractive or repulsive zone, i.e., $\Delta\gamma_a = \Delta\gamma_0$ and $\Delta\gamma_a = \pi/2 - \Delta\gamma_0$. The probability density function $p(\Delta\gamma)$ of a bacterium to circulate about the pillar for an arbitrary $\Delta\gamma$ is given by

$$p(\Delta\gamma)\mathrm{d}\Delta\gamma = (1 - P_a)^{n_a}(1 - P_r)^{n_r}\ \nu_{a,r}\mathrm{d}\Delta\gamma, \tag{15}$$

where $n_{a,r}$ are multiples (as real numbers) of attractive or repulsive zones covered in the circulation, and the index (a or r) of ν is determined by the type of zones where the bacterium escapes. This probability distribution thus depends not only on the residency arc angle $\Delta\gamma$ but also on the detailed location of γ_i and γ_f within the attractive and repulsive zones. Not surprisingly, for isotropic escaping ($P_a = P_r$ and $\nu_a = \nu_r$), our result becomes $p(\Delta\gamma) = \nu_r e^{-\nu_r \Delta\gamma}$, recovering a classic Poisson process.

Examples of such distribution functions (averaged for all possible γ_i) are computed and shown in Figure D.3.1(a). We also computed the corresponding mean residency arc angles $\langle\Delta\gamma\rangle$, which show a decent agreement with the experimental observations (Figure. D.3 (b)).

References

1. Vos, T. *et al.* Global burden of 369 diseases and injuries in 204 countries and territories, 1990–2019: a systematic analysis for the Global Burden of Disease Study 2019. *The Lancet* **396**, 1204–1222 (2020).
2. Murray, C. J. *et al.* Global burden of bacterial antimicrobial resistance in 2019: a systematic analysis. *The Lancet* **399**, 629–655 (2022).
3. Forman, D. & Burley, V. J. Gastric cancer: global pattern of the disease and an overview of environmental risk factors. *Best Pract. Res. Clin. Gastroenterol.* **20**, 633–649 (2006).
4. *Cancer Epidemiology: Modifiable Factors*. vol. 472 (Humana Press, 2009).
5. Hall-Stoodley, L., Costerton, J. W. & Stoodley, P. Bacterial biofilms: from the Natural environment to infectious diseases. *Nat. Rev. Microbiol.* **2**, 95–108 (2004).
6. Belas, R. Biofilms, flagella, and mechanosensing of surfaces by bacteria. *Trends Microbiol.* **22**, 517–527 (2014).
7. Ge, X. *et al.* Bacterial responses to periodic micropillar array: Bacterial Responses to Periodic Micropillar Array. *J. Biomed. Mater. Res. A* **103**, 384–396 (2015).
8. Swiecicki, J.-M., Sliusarenko, O. & Weibel, D. B. From swimming to swarming: Escherichia coli cell motility in two-dimensions. *Integr. Biol.* **5**, 1490 (2013).
9. Schumacher, J. F. *et al.* Engineered antifouling microtopographies – effect of feature size, geometry, and roughness on settlement of zoospores of the green alga *Ulva*. *Biofouling* **23**, 55–62 (2007).

10. Nishiguchi, D., Aranson, I. S., Snezhko, A. & Sokolov, A. Engineering bacterial vortex lattice via direct laser lithography. *Nat. Commun.* **9**, 4486 (2018).
11. Sowa, Y. & Berry, R. M. Bacterial flagellar motor. *Q. Rev. Biophys.* **41**, 103–132 (2008).
12. Berg, H. C. *E. coli in motion*. (Springer, 2004).
13. Xing, J., Bai, F., Berry, R. & Oster, G. Torque–speed relationship of the bacterial flagellar motor. *Proc. Natl. Acad. Sci.* **103**, 1260–1265 (2006).
14. Lowe, G., Meister, M. & Berg, H. C. Rapid rotation of flagellar bundles in swimming bacteria. *Nature* **325**, 637–640 (1987).
15. Sourjik, V. & Wingreen, N. S. Responding to chemical gradients: bacterial chemotaxis. *Curr. Opin. Cell Biol.* **24**, 262–268 (2012).
16. Clausznitzer, D., Oleksiuk, O., Løvdok, L., Sourjik, V. & Endres, R. G. Chemotactic Response and Adaptation Dynamics in Escherichia coli. *PLoS Comput. Biol.* **6**, e1000784 (2010).
17. Cai, Q., Li, Z., Ouyang, Q., Luo, C. & Gordon, V. D. Singly Flagellated *Pseudomonas aeruginosa* Chemotaxes Efficiently by Unbiased Motor Regulation. *mBio* **7**, e00013-16, /mbio/7/2/e00013-16.atom (2016).
18. Altindal, T., Chattopadhyay, S. & Wu, X.-L. Bacterial Chemotaxis in an Optical Trap. *PLoS ONE* **6**, e18231 (2011).

19. Bertrand, T., Zhao, Y., Bénichou, O., Tailleur, J. & Voituriez, R. Optimized Diffusion of Run-and-Tumble Particles in Crowded Environments. *Phys. Rev. Lett.* **120**, 198103 (2018).
20. Pattanayak, S., Das, R., Kumar, M. & Mishra, S. Enhanced dynamics of active Brownian particles in periodic obstacle arrays and corrugated channels. *Eur. Phys. J. E* **42**, 62 (2019).
21. Phan, T. V. *et al.* Bacterial Route Finding and Collective Escape in Mazes and Fractals. *Phys. Rev. X* **10**, 031017 (2020).
22. Ribeiro, H. E., Ferreira, W. P. & Potiguar, F. Q. Trapping and sorting of active matter in a periodic background potential. *Phys. Rev. E* **101**, 032126 (2020).
23. Brun-Cosme-Bruny, M. *et al.* Deflection of phototactic microswimmers through obstacle arrays. *Phys. Rev. Fluids* **5**, 093302 (2020).
24. Creppy, A., Clément, E., Douarche, C., D'Angelo, M. V. & Auradou, H. Effect of motility on the transport of bacteria populations through a porous medium. *Phys. Rev. Fluids* **4**, 013102 (2019).
25. Bhattacharjee, T. & Datta, S. S. Bacterial hopping and trapping in porous media. *Nat. Commun.* **10**, 2075 (2019).
26. Lauga, E., DiLuzio, W. R., Whitesides, G. M. & Stone, H. A. Swimming in Circles: Motion of Bacteria near Solid Boundaries. *Biophys. J.* **90**, 400–412 (2006).

27. Spagnolie, S. E., Moreno-Flores, G. R., Bartolo, D. & Lauga, E. Geometric capture and escape of a microswimmer colliding with an obstacle. *Soft Matter* **11**, 3396–3411 (2015).
28. Sipos, O., Nagy, K., Di Leonardo, R. & Galajda, P. Hydrodynamic Trapping of Swimming Bacteria by Convex Walls. *Phys. Rev. Lett.* **114**, 258104 (2015).
29. Liu, B. *et al.* Helical motion of the cell body enhances Caulobacter crescentus motility. *Proc. Natl. Acad. Sci.* **111**, 11252–11256 (2014).
30. Taute, K. M., Gude, S., Tans, S. J. & Shimizu, T. S. High-throughput 3D tracking of bacteria on a standard phase contrast microscope. *Nat. Commun.* **6**, (2015).
31. Wioland, H., Woodhouse, F. G., Dunkel, J. & Goldstein, R. E. Ferromagnetic and antiferromagnetic order in bacterial vortex lattices. *Nat. Phys.* **12**, 341–345 (2016).
32. Celli, J. P. *et al. Helicobacter pylori* moves through mucus by reducing mucin viscoelasticity. *Proc. Natl. Acad. Sci.* **106**, 14321–14326 (2009).
33. Sándor, Cs., Libál, A., Reichhardt, C. & Olson Reichhardt, C. J. Dynamic phases of active matter systems with quenched disorder. *Phys. Rev. E* **95**, 032606 (2017).
34. Berke, A. P., Turner, L., Berg, H. C. & Lauga, E. Hydrodynamic Attraction of Swimming Microorganisms by Surfaces. *Phys. Rev. Lett.* **101**, (2008).
35. Drescher, K., Dunkel, J., Cisneros, L. H., Ganguly, S. & Goldstein, R. E. Fluid dynamics and noise in bacterial cell-cell and cell-surface scattering. *Proc. Natl. Acad. Sci.* **108**, 10940–10945 (2011).

36. Bianchi, S., Saglimbeni, F. & Di Leonardo, R. Holographic Imaging Reveals the Mechanism of Wall Entrapment in Swimming Bacteria. *Phys. Rev. X* **7**, 011010 (2017).
37. Galajda, P., Keymer, J., Chaikin, P. & Austin, R. A Wall of Funnels Concentrates Swimming Bacteria. *J. Bacteriol.* **189**, 8704–8707 (2007).
38. Makarchuk, S., Braz, V. C., Araújo, N. A. M., Ciric, L. & Volpe, G. Enhanced propagation of motile bacteria on surfaces due to forward scattering. *Nat. Commun.* **10**, 4110 (2019).
39. Dehkharghani, A., Waisbord, N., Dunkel, J. & Guasto, J. S. Bacterial scattering in microfluidic crystal flows reveals giant active Taylor–Aris dispersion. *Proc. Natl. Acad. Sci.* **116**, 11119–11124 (2019).
40. *Optofluidics: fundamentals, devices, and applications*. (McGraw-Hill, 2010).
41. Ng, J. M. K., Gitlin, I., Stroock, A. D. & Whitesides, G. M. Components for integrated poly(dimethylsiloxane) microfluidic systems. *Electrophoresis* **23**, 3461–3473 (2002).
42. Mack, C. A. *Fundamental principles of optical lithography: the science of microfabrication*. (Wiley, 2007).
43. Madou, M. J. *Fundamentals of Microfabrication*. (CRC Press, 2018). doi:10.1201/9781482274004.
44. *Handbook of Photomask Manufacturing Technology*. (CRC Press, 2018). doi:10.1201/9781420028782.

45. Levenson, M. D., Viswanathan, N. S. & Simpson, R. A. Improving resolution in photolithography with a phase-shifting mask. *IEEE Trans. Electron Devices* **29**, 1828–1836 (1982).

46. *Fine line lithography*. vol. 1 (Elsevier North-Holland Publishing Co., 1980).

47. Tyona, M. D. A theoritical study on spin coating technique. *Adv. Mater. Res.* **2**, 195–208 (2013).

48. Cheng, J.-Y., Wei, C.-W., Hsu, K.-H. & Young, T.-H. Direct-write laser micromachining and universal surface modification of PMMA for device development. *Sens. Actuators B Chem.* **99**, 186–196 (2004).

49. Hedrick, T. L. Software techniques for two- and three-dimensional kinematic measurements of biological and biomimetic systems. *Bioinspir. Biomim.* **3**, 034001 (2008).

50. Romanczuk, P., Bär, M., Ebeling, W., Lindner, B. & Schimansky-Geier, L. Active Brownian Particles. From Individual to Collective Stochastic Dynamics. *Eur. Phys. J. Spec. Top.* **202**, 1–162 (2012).

51. Bechinger, C. *et al.* Active Particles in Complex and Crowded Environments. *Rev. Mod. Phys.* **88**, 045006 (2016).

52. Morin, A., Desreumaux, N., Caussin, J.-B. & Bartolo, D. Distortion and destruction of colloidal flocks in disordered environments. *Nat. Phys.* **13**, 63–67 (2017).

53. Quint, D. A. & Gopinathan, A. Topologically induced swarming phase transition on a 2D percolated lattice. *Phys. Biol.* **12**, 046008 (2015).

54. Yazdi, S., Aragones, J. L., Coulter, J. & Alexander-Katz, A. Metamaterials for Active Colloid Transport. (2020).
55. Reichhardt, C. & Reichhardt, C. J. O. Directional locking effects for active matter particles coupled to a periodic substrate. *Phys. Rev. E* **102**, 042616 (2020).
56. Young, K. D. The Selective Value of Bacterial Shape. *Microbiol. Mol. Biol. Rev.* **70**, 660–703 (2006).
57. Rappé, M. S., Connon, S. A., Vergin, K. L. & Giovannoni, S. J. Cultivation of the ubiquitous SAR11 marine bacterioplankton clade. *Nature* **418**, 630–633 (2002).
58. Angert, E. R., Clements, K. D. & Pace, N. R. The largest bacterium. *Nature* **362**, 239–241 (1993).
59. Hahn, M. W., Moore, E. R. B. & Höfle, M. G. Bacterial Filament Formation, a Defense Mechanism against Flagellate Grazing, Is Growth Rate Controlled in Bacteria of Different Phyla. *Appl. Environ. Microbiol.* **65**, 25–35 (1999).
60. Typas, A., Banzhaf, M., Gross, C. A. & Vollmer, W. From the regulation of peptidoglycan synthesis to bacterial growth and morphology. *Nat. Rev. Microbiol.* **10**, 123–136 (2012).
61. Shen, J.-P. & Chou, C.-F. Morphological plasticity of bacteria—Open questions. *Biomicrofluidics* **10**, 031501 (2016).
62. Schuech, R., Hoehfurtner, T., Smith, D. J. & Humphries, S. Motile curved bacteria are Pareto-optimal. *Proc. Natl. Acad. Sci.* **116**, 14440–14447 (2019).

63. Persat, A., Stone, H. A. & Gitai, Z. The curved shape of Caulobacter crescentus enhances surface colonization in flow. *Nat. Commun.* **5**, 3824 (2014).
64. Turnbull, G. A., Morgan, J. A. W., Whipps, J. M. & Saunders, J. R. The role of bacterial motility in the survival and spread of Pseudomonas fluorescens in soil and in the attachment and colonisation of wheat roots. *FEMS Microbiol. Ecol.* **36**, 21–31 (2001).
65. Balzan, S., de Almeida Quadros, C., de Cleva, R., Zilberstein, B. & Cecconello, I. Bacterial translocation: Overview of mechanisms and clinical impact. *J. Gastroenterol. Hepatol.* **22**, 464–471 (2007).
66. Hermansson, M. The DLVO theory in microbial adhesion. *Colloids Surf. B Biointerfaces* **14**, 105–119 (1999).
67. Tong, J. & Shelley, M. J. Directed Migration of Microscale Swimmers by an Array of Shaped Obstacles: Modeling and Shape Optimization. *SIAM J. Appl. Math.* **78**, 2370–2392 (2018).
68. Davies Wykes, M. S. *et al.* Guiding microscale swimmers using teardrop-shaped posts. *Soft Matter* **13**, 4681–4688 (2017).
69. Cox, R. G. & Brenner, H. The slow motion of a sphere through a viscous fluid towards a plane surface—II Small gap widths, including inertial effects. *Chem. Eng. Sci.* **22**, 1753–1777 (1967).
70. Jakuszeit, T., Croze, O. A. & Bell, S. Diffusion of active particles in a complex environment: Role of surface scattering. *Phys. Rev. E* **99**, 012610 (2019).

71. Schakenraad, K. *et al.* Topotaxis of active Brownian particles. *Phys. Rev. E* **101**, 032602 (2020).

72. Bakken, L. R. & Olsen, R. A. The relationship between cell size and viability of soil bacteria. *Microb. Ecol.* **13**, 103–114 (1987).

73. Long, Z., Quaife, B., Salman, H. & Oltvai, Z. N. Cell-cell communication enhances bacterial chemotaxis toward external attractants. *Sci. Rep.* **7**, 12855 (2017).

74. Wainwright, M., Canham, L. T., Al-Wajeeh, K. & Reeves, C. L. Morphological changes (including filamentation) in *Escherichia coli* grown under starvation conditions on silicon wafers and other surfaces. *Lett. Appl. Microbiol.* **29**, 224–227 (1999).

75. Miller, C. *et al.* SOS Response Induction by ß-Lactams and Bacterial Defense Against Antibiotic Lethality. *Science* **305**, 1629–1631 (2004).

76. Justice, S. S., Hunstad, D. A., Seed, P. C. & Hultgren, S. J. Filamentation by *Escherichia coli* subverts innate defenses during urinary tract infection. *Proc. Natl. Acad. Sci.* **103**, 19884–19889 (2006).

77. Ivanova, E. P. *et al.* Natural Bactericidal Surfaces: Mechanical Rupture of Pseudomonas aeruginosa Cells by Cicada Wings. *Small* **8**, 2489–2494 (2012).

78. Chopra, P., Quint, D., Gopinathan, A. & Liu, B. Geometric effects induce anomalous size-dependent active transport in structured environments. *Phys. Rev. Fluids* **7**, L071101 (2022).

79. Qu, Z., Temel, F. Z., Henderikx, R. & Breuer, K. S. Changes in the flagellar bundling time account for variations in swimming behavior of flagellated bacteria in viscous media. *Proc. Natl. Acad. Sci.* **115**, 1707–1712 (2018).

80. Feller, W. *An introduction to probability theory and its applications. Vol. 1*. vol. 1 (Wiley, 2009).